AN EXPERIMENT TO STUDY THE FORMATION OF CHARMONIUM STATES IN ANTIPROTON-PROTON ANNIHILATION AT CERN'S INTERSECTING STORAGE RINGS.

Bjarne Stugu.

Thesis presented in partial fulfillment of the requirements to obtain
the degree Dr. Scient. at the University of Oslo, Inst. of Physics.
Oslo, January 1987.

CERN LIBRARIES, GENEVA

CM-P00099086

Errata.

Two of the incertitudes of table 4.2 (page 98) are interchanged. The correct table reads:

Sample:	Assumptions:	Parameter:	Value:
χ_1	none	B_0	$< .83$
		a_2	$-.10^{+.34}_{-.26}$
	$B_0=0$	a_2	$-.13 \pm .19$
χ_2	$a_3=0$	B_0	$< .70$
		a_2	$.46^{+.19}_{-.18}$

Table 4.2: Helicity zero components and magnetic quadrupole components determined from the maximum likelihood fits of the χ_1 and χ_2 samples.

Table 4.3 (page 104) should read:

Sample	Test function	C.L. for J=0	C.L. for J=1	C.L. for J=2
χ_1	R_{01}	7.5%	50.4%	-----
χ_2	R_{02}	0.5%	-----	55.2%
χ_2	R_{12}	----	2.6%	36.0%

Table 4.3: Confidence levels of spin tests.

CERN LIBRARIES, GENEVA

AN EXPERIMENT TO STUDY THE FORMATION OF CHARMONIUM STATES IN ANTIPROTON-PROTON ANNIHILATION AT CERN'S INTERSECTING STORAGE RINGS.

Bjarne Stugu.

Thesis presented in partial fulfillment of the requirements to obtain the degree Dr. Scient. at the University of Oslo, Inst. of Physics.

Oslo, January 1987.

ABSTRACT

We present the experiment R704 at CERN's ISR, which makes use of a hydrogen gas-jet target and antiprotons circulating in the ISR for the study of charmonium states formed directly in antiproton-proton annihilation. A number of charmonium states were tagged by their radiative decays to the J/ψ, which in turn decayed into electron-positron pairs. We present an analysis searching electron positron pairs which are compatible with the decay of a J/ψ. Specifically, the $^1P_1$ charmonium state is searched. 5 events compatible with the formation of this state, subsequently decaying into a J/ψ, are found. When interpreted as a resonance, its mass is compatible with being at the centre of gravity of the ^3P states. However, we cannot reject the hypothesis that the events stem from non-resonant inclusive production of the J/ψ.

Furthermore, we present a study of the angular distributions in the processes $\bar{p}p \to \chi_J \to \gamma\psi \to \gamma e^+ e^-$, $J=1,2$. We find that the data prefer the conventional spin assignments of the χ_1 and χ_2 states although alternative spin hypotheses may not be ruled out from this study alone. The χ_1 radiative transition to the J/ψ is found to be compatible with a pure dipole transition. However, the χ_2 data seem to indicate the presence of a positive quadrupole component. The χ_2 data are found to be compatible with the hypothesis that a single quark radiates the γ in the transition to the J/ψ.

Finally we present measurements of the $\bar{p}p$ elastic cross section at 90^0 CM. The precision of these measurements greatly exeeds the precision of previously existing data. It is found that $d\sigma/dt$ at 90^0 CM decreases faster than s^{-12} in the lab. momentum range from 3.6 to 5.7 Gev/c.

ACKNOWLEDGEMENTS

This thesis is the result of my work within the R704 collaboration at CERN as well as at the University of Oslo. The spirit of this collaboration has proved very inspiring for the pursue of my work, and the devoted work of every member has been a necessary condition for the success of the experiment. I am therefore indebted to all members of the R704 collaboration.

Particularily, I would like to express my sincerest thanks to Dr. Philos. Torleiv Buran for patient and inspiring guidance in every aspect of experimental high energy physics necessary for the completion of this work. Furthermore I am greatly indebted to Cand. Real. Lars Bugge for many useful discussions and comments. Finally, I would like to thank professor Arne Lundby for making my stay at CERN possible.

I am in the very fortunate situation of always being supported in every possible way by my caring parents. This have greatly facilitated my work, and I use this opportunity to express my warmest thanks to my parents for all influence they have had on my personal development.

TABLE OF CONTENTS:

Page

1. INTRODUCTION TO CHARMONIUM PHYSICS
 1.1 Introduction ... 1
 1.2 Experimental Overview ... 3
 1.3 Charmonium and QCD ... 5
 1.4 The Charmonium Model ... 6
  1.4.1 Non Relativistic Potential Models ... 6
  1.4.2 Alternative Approaches ... 9
  1.4.3 Spin Dependent Forces ... 11
  1.4.4 Width of Charmonium ... 14
  1.4.5 Radiative Transitions ... 16
 1.5 Charmonium in Antiproton-proton Collisions ... 17

2. DESCRIPTION OF THE R704 EXPERIMENT
 2.1 Introduction ... 20
 2.2 Antiprotons for R704 ... 21
 2.3 Target System ... 25
 2.4 Detectors ... 28
  2.4.1 The Main Arms ... 30
   2.4.1.1 The Trigger Hodoscopes ... 30
   2.4.1.2 The Cerenkov Counters ... 32
   2.4.1.3 The Multiwire Proportional Chambers ... 33
   2.4.1.4 The Precalorimeter ... 35
   2.4.1.5 The Analog Chambers ... 36
   2.4.1.6 The Lead Glass Wall ... 37
  2.4.2 The Veto Counters ... 38
  2.4.3 Luminosity Counters and Measurements ... 40
 2.5 Calibration of the Calorimeters ... 42
 2.6 Trigger and Data Aquisition ... 44
 2.7 Use of Luminosity in the Experiment R704 ... 46

3. INCLUSIVE ψ ANALYSIS ... 48
 3.1 Data Reduction ... 48
 3.2 Final Analysis ... 52
  3.2.1 The ψ as an Analyser ... 52
  3.2.2 The Final Event Selection ... 53
  3.2.3 Comments on the Event Samples ... 60
  3.2.4 Efficiency of the Analysis ... 61
 3.3 Interpretation of the Events ... 62
  3.3.1 The χ Samples ... 62
  3.3.2 The $^1P_1$ Sample ... 64
  3.3.3 The Resonance Hypothesis ... 69
 3.4 Conclusions ... 75

4. ANGULAR DISTRIBUTIONS 76
4.1 Introduction 76
4.2 Helicity Formalism 77
4.3 Determination of the Angles 82
4.4 Acceptance Calculations 86
4.5 Features Apparent in the Raw Distributions 89
4.6 Analysis of the Angular Distributions 93
4.6.1 Choice of Method 93
4.6.2 Parity Transformations 94
4.6.3 Constructing the Likelihood Function 94
4.7 Results 96
4.7.1 Testing the SQR Hypothesis 97
4.7.2 Determining the Parameters 98
4.7.3 Spin Tests 100
4.8 Multipole Transitions and the Quark Magnetic Moment 104
4.9 Conclusions 106

5. ELASTIC SCATTERING AT 90^0 CM 108
5.1 Introduction 108
5.2 The Trigger 109
5.3 Offline Analysis 111
5.3.1 Production 111
5.3.2 Background Substraction 115
5.3.3 Correction Factors 118
5.4 The Elastic Cross-section 120
5.5 Discussion 121
5.6 Conclusions 126

6. CONCLUSIONS 127

APPENDICES 129
1. R704 Coordinate Systems 129
2. Angular Distributions in the Helicity Formalism 131
3. Monte Carlo Simulation of a Distribution 135
4. Statistical Methods 137

REFERENCES 142

1. *INTRODUCTION TO CHARMONIUM PHYSICS*

1.1 Introduction

When the existence of extremely narrow hadronic states with masses larger than 3 Gev/c^2 was evidenced in 1974 [1,2,3], it did not last long until the physics community felt convinced that these states were made up of a new type of quarks, charm quarks. The narrowness of the states together with the relatively small mass difference between the 1^{--} ground state (the J/ψ)* and its first radial exitation (the ψ') suggested that these particles consisted of a massive quark-antiquark pair.

Many authors were speculating on the existence of a fourth quark long before its discovery. In 1964 [4], ideas requiring quark-lepton symmetry were put forward. This necessitated a fourth quark, given the existence of four leptons.

Several experimental facts would also be better understood if a fourth quark were introduced. The ratio of cross-sections of $e^+e^- \to$ hadrons to $e^+e^- \to \mu^+\mu^-$ is expected to be approximately given by:

$$R = \frac{\sigma(e^+e^- \to \text{hadrons})}{\sigma(e^+e^- \to \mu^+\mu^-)} = 3 \sum_i q_i^2$$

where the sum runs over the number of quark flavours, and q_i is the charge of the i-th quark flavour. QCD introduces three colours, hence the factor 3. The introduction of a fourth quark rises this ratio from 2 to 3.3. This is in better agreement with experiment.

Another problem was the experimental suppression of weak decays such

* The J/ψ will frequently be denoted by just "ψ" in this thesis.

as $K^+ \to \pi^+ e^+ e^-$, which could not be explained within the framework of weak interactions with just three quarks. In particular, concidering the two reactions $K^+ \to \pi^0 e^+ \nu$ and $K^+ \to \pi^+ e^+ e^-$ described by the following diagrams in a model with three quarks;

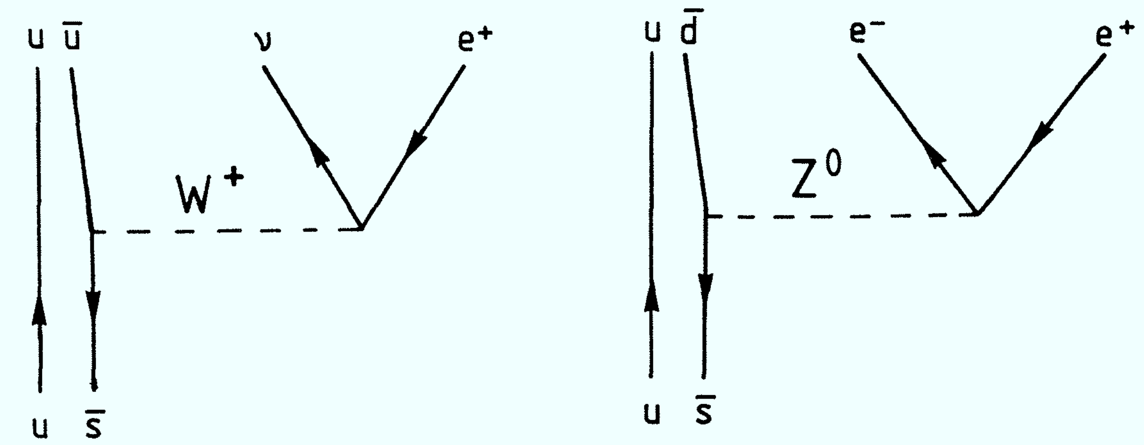

Fig. 1.1: Kaon weak decays in a three quark model.

one should expect that the first process is due to the charged current

$$J^{\mu}_{+} = \bar{u}\gamma^{\mu} \frac{1}{2}(1-\gamma_5)d'$$

where d' is the Cabbibo rotated state, $d' = d\cos(\theta) + s\sin(\theta)$, while the second process is due to the neutral current given by:

$$J^{\mu}_{o} = \bar{d}'\gamma^{\mu} \frac{1}{2}(1-\gamma_5)d' \qquad ;$$

i. e. it should have a probability of the same order of magnitude as the first one. However, experiment shows that the ratio between the two branching fractions is 1.7×10^{5}. The introduction of a fourth quark,[5], may cure this problem if, instead of having just one quark multiplet,(u,d'), a second one is introduced, (c,s'), where $s' = s\cos(\theta) - d\sin(\theta)$. Then the neutral current involving strangeness would contain two pieces:

$$J_0^\mu = \bar{d}'\gamma^\mu \frac{1}{2}(1-\gamma_5)d' + \bar{s}'\gamma^\mu \frac{1}{2}(1-\gamma_5)s' \quad .$$

We see that the part giving the transition $s \to d$ in the first term will be cancelled by a similar part in the second term. This is exactly what is required to explain the small branching ratio of $K^+ \to \pi^+ e^+ e^-$.

1.2 Experimental Overview

Following the discovery of the J/ψ, lots of activity was devoted to the search for new charmonium states. Except for the discovery of the J/ψ in the process $p+Be \to e^+e^- + X$, most data on charmonium, until the experiment R704, come from electron-positron annihilation in storage rings. In electron-positron annihilation, only the states with the quantum numbers of the photon are produced directly, i.e. the $^3S_1$ and the $^3D_1$ states. The remaining states are searched in transitions from higher lying states.

A substantial fraction of the decays of the higher lying states are radiative. A study of the inclusive photon spectrum of the decay of the ψ' led to the discovery of three new states at DESY in 1975 , the χ_0, χ_1 and the χ_2 [6]. These states had masses between the ψ and the ψ' mass, and were naturally interpreted as ^3P-wave charmonium.

In 1978 the Crystal Ball detector was installed at SPEAR [37]. This detector was designed especially to study photon spectra. Some 0.9×10^6 ψ' events were collected, and the inclusive photon spectrum in fig. 1.2 was obtained. From this spectrum, five states were evidenced, the three χ_J states, and two new states, the η_c and the η_c'. Moreover, by studying exclusive reactions, the spin and parity of the χ_J states were obtained. Fairly precise measurements of the masses of the χ_J states were also obtained. However, the precision of these measurements was limited by the detector resolution, and suffered also from a systematic error of about 4 Mev, due to the uncertainty of the detector calibration. Although the performance of the Crystal Ball detector is exceptionally good, these measurements are very unprecise compared to the precision obtained for the masses of the resonances which were produced directly in electron-positron annihilation. Another merit of the C.B. detector was that it ruled out the existence of several candidates for the singlet S states, in particular the X(2830) seen at DESY. This resolved several difficulties with the charmonium model.

Finally, we must mention the measurements of the Mark III collaboration [7] on the η_c, which allowed for the determination of the spin and parity of this state by studying the cascade $\psi \to \gamma\ \eta_c \to \gamma\ \varphi\ \varphi \to \gamma + 4K$. Table 1.1 summarizes the experimental status of the charmonium states below the open charm threshold.

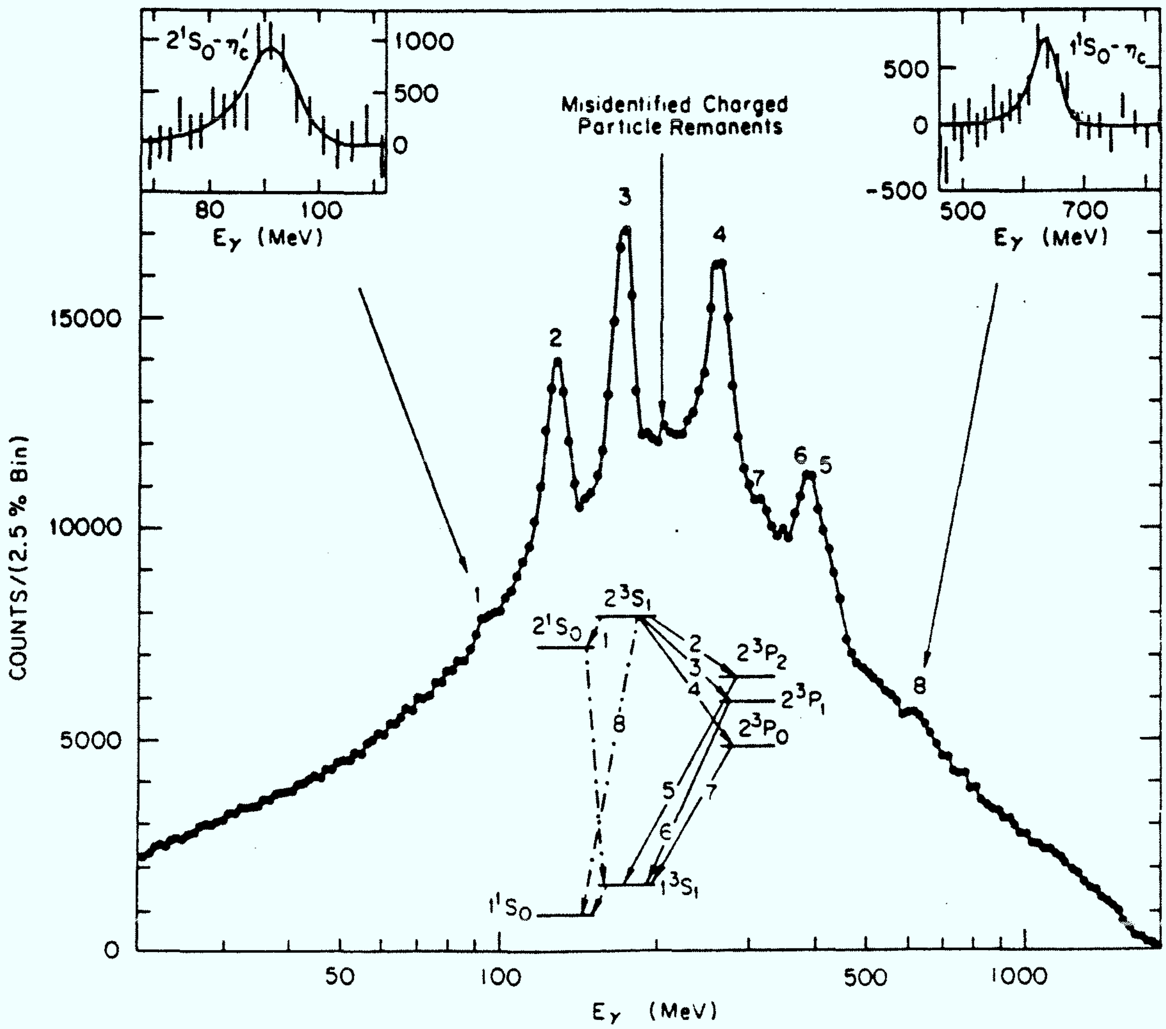

Fig. 1.2: Inclusive photon spectrum from the Crystal Ball detector. Five charmonium states are evidenced. From [37].

State	$(n-1)\,{}^{2J+1}l_J$	Mass (MeV)	Width (MeV)
η_c	1^1S_0	2984 ± 4	12.4 ± 4.1
J/ψ	1^3S_1	3096.9 ± 0.09	.063 ± .009
χ_0	1^3P_0	3415 ± 1	11 ± 2
χ_1	1^3P_1	3509 ± 0.55	< 3.8
χ_2	1^3P_2	3555.8 ± 0.6	.85 - 4.9
η_c'	2^1S_0	3594 ± 5	< 8
ψ'	2^3S_1	3686.0 ± 0.1	.215 ± .04

Table 1.1: Experimentally measured masses and widths of charmonium states (pre R704). The η_c' is seen by just one experiment. An expected state, the "${}^1P_1$", is still not found [8].

1.3 Charmonium and QCD

The properties of the charmonium states are mainly determined by the nature of strong interactions. In particular, the candidate theory of strong interactions, Quantum Chromodynamics (QCD), may be probed. QCD is a gauge field theory with SU(3) as the gauge group. Each quark is postulated to carry a new quantum number called colour, which may have three different values. The QCD Lagrangian should be locally invariant when the quark colour triplets are transformed by elements of the fundamental representation of SU(3). Invariance of the Lagrangian implies the existence of eight gluon fields which, in addition to interacting with the quark fields, also interact with themselves. Moreover it is postulated that only colour singlets exist in nature as free entities. This postulate implies the existence of confining forces, i.e. of forces between the quarks which give rise to a potential energy of the system which tends to infinity as the quark separation increases. The two simplest $SU(3)_C$ singlets are $q\bar{q}$ and qqq states, which are the mesons and the baryons respectively.

Another important property of QCD is that the effective coupling constant tends to zero as the quark separation decreases. This property, called asymptotic freedom, is derived by considering second order effects in perturbation theory. At distances smaller than about .3-.5 fm., the coupling constant is substantially smaller than unity, meaning that interactions due to one-gluon exchanges dominate. Thus, in this region, QCD should behave quite similarily to QED, and perturbation theory should be valid. In the non-relativistic approximation, one gluon exchange corresponds to a situation where the interaction between two particles may be described by a potential of the Coulomb type, i.e. $V(r) \alpha r^{-1}$.

1.4 The Charmonium Model

1.4.1 Non Relativistic Potential Models.

The narrowness of the charmonium states suggests that the c-quark is a rather heavy object. This gave hope to the possibility that the charmonium system could be described within a non-relativistic Scroedinger picture. This may be investigated by estimating the speed of the quarks crudely. Consider a two-particle system in one dimension acting on eachother with a force proportional to their separation. The Hamiltonian is:

$$H = p^2/2\mu + \mu(\omega x)^2/2$$

where μ is the reduced mass of the system. The virial theorem reads:

$$\langle p^2/\mu \rangle = \langle x\frac{dV}{dx} \rangle$$

giving;

$$\langle\beta^2\rangle = \langle x\frac{dV}{dx}\rangle = \frac{\mu\omega^2}{2m} \langle x^2\rangle$$

where β is the speed of the quarks in units of the speed of light,c.

From the well-known wavefunction of the harmonic oscillator, the expectation value $\langle x^2\rangle$ may be calculated in terms of μ and ω.This yields $\langle x^2\rangle = (2\mu\omega)^{-1}$ The energy difference between the ψ' and the J/ψ is equal to ω=.589Gev, so:

$$\langle\beta^2\rangle = \frac{\omega}{4m} = \frac{.589}{4*1.5} \approx .1$$

for a quark mass of 1.5 Gev/c^2. Hence it seems appropriate to attempt to describe the $c\bar{c}$ system within a non-relativistic framework.

A variety of potentials have been put into the Schroedinger equation in order to reproduce the energy spectrum of the $c\bar{c}$ system. In order to fulfill the requirements of QCD, all models have some features in common, namely the properties implied by asymptotic freedom and confinement. For small distances, the potential should therefore be of the Coulomb type, while confinement should be realized at large distances. Many authors expect the potential to rize linearily with the quark separation. The Cornell potential [9] :

$$V(r) = -\frac{4}{3}\frac{\alpha_s}{r} + ar$$

seems to give a reasonably good description of the data. Another approach is to define the two parts of the potential separately for large and small distances [10], i.e.:

$$V(r) = \begin{cases} -k/r & ; r<r_0 \\ -V_0 + ar & ; r>r_0 \end{cases}$$

Imposing the constraint that the potential should be continous and have a continous derivative, gives $r_0 = \sqrt{(k/a)}$ and $V_0 = 2\sqrt{(ak)}$, hence the number of free parameters is the same as in the Cornell potential.

It is interesting to note that the preferred values of k and a yield a value of r_0 close to .3fm. when charmonium and bottomium states are fitted simultaneously. Most models produce a mean radius for the J/ψ of about .45fm, hence it seems like the short range nature of QCD is not very well probed with the charmonium system.

Other potentials which have been used, include the purely phenomenological [11]:

$$V(r) = C \ln(r/r_0)$$

which produces level splittings between orbital exitations which are independent of the quark masses, a feature which seems to be roughly fullfilled since the level splittings in charmonium are nearly equal to those in bottomium. Furthermore, the potential [12]:

$$V(r) = Ar^{v}$$

describes data well, when v =.1. Many general properties may be derived from such a simple potential, so a lot of information may be extracted although the potential is purely phenomenological.

One should also mention a potential which is derived in momentum space from the potential describing one gluon exchange [13]:

$$V(q^2) = 4\alpha_s(q^2)/(3q^2)$$

with

$$\alpha_s(q^2) = (4\pi/9)\ln(\Lambda^2/q^2)$$

where Λ is the QCD scale parameter. A confining term is introduced by noting that the Fourier transform of a linear term, ar, is $V(q^2) \alpha 1/(q^2)^2$. A simple interpolating formula

$$V(q^2) = \frac{4}{3}\frac{4\pi}{9}\frac{1}{q^2\ln(1-q^2/\Lambda^2)}$$

ensure the correct long and short range properties of the potential. Actual calculations are performed by Fourier transforming this potential to position space. The best value for Λ obtained, agrees with what is found in e.g deep inelastic scattering. In fig. 1.3 we show a comparison between a number of potentials. We see that in the region where we find the charmonium states, they are practically coinciding.

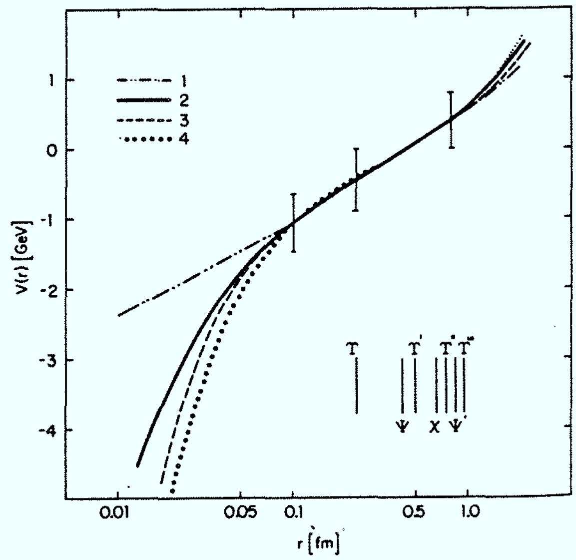

Fig. 1.3: A comparison between various successful potentials. (1) Martin, [38]; (2) Buchmuller, Grunberg and Tye, [39]; (3) Bhanot and Rudaz, [40]; (4) Eichten et al., [41].

1.4.2 Alternative Approaches.

The phenomenological potential models are very attractive due to the fact that they are relatively simple. Data are also described well within this framework. However, the connection to QCD is not always too clear. In this section, we describe very briefly two alternative approaches.

In the "QCD sum rule" approach [15], vacuum polarisation tensors of

QCD are studied. Unitarity and analyticity properties of these tensors are exploited in order to derive masses, widths and transition rates of several charmonium states. So far, only properties of the lowest lying state with a specific set of quantum numbers can be derived.

The greatest succes of the QCD sum rules is the rejection of the X(2830) as a candidate for the η_c[16]. Instead, this state was predicted at (3.00 ± 0.03) GeV/c^2. This prediction was confirmed later on with the Crystal Ball discovery of the η_c at 2.98 GeV/c^2 [17]. The widths of the P-states also seem to be in good shape within this framework.

The quark separation in charmonium is too large for the use of perturbation theory. Unfortunately, there is no known way of performing calculations at large distances in QCD. However, within the framework of lattice gauge theories, large distance properties of QCD may be obtained [18]. In lattice QCD, the colour electric and magnetic fields are defined on discrete points in space-time. Instead of evaluating properties of QCD analytically on the lattice, it is necessary to perform large computer simulations. Progress has been made in determining the long-range static QCD potential through this approach. In fig. 1.4, a compilation of the results for the static potential is shown. Spin effects may also be included in the simulations. This is described in the section below.

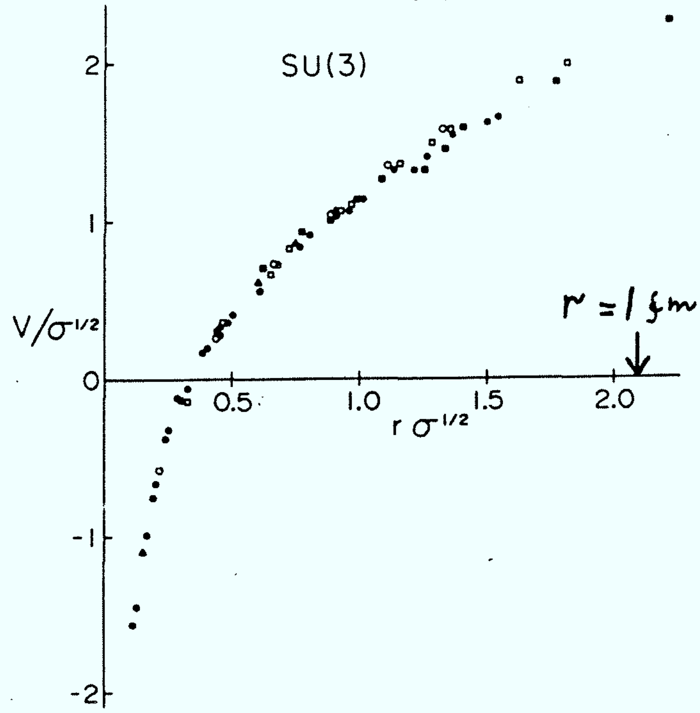

Fig. 1.4: A compilation of estimates of the static potential in lattice QCD. From [18].

1.4.3 Spin Dependent Forces.

In perturbative field theory, interactions are described by the exchange of field quanta and transition elements. The connection between this interaction picture and the potential is given by [19]:

$$V(r) = (2\pi)^{-3} \int M_{fi} e^{i\vec{q}.\vec{r}} dq^3$$

where M_{fi} is the transition element, and $\vec{q}$ is the momentum transfer. To zero order in v/c, the transition element is proportional to $V(q)=1/q^2$. The Fourier transform of this gives the Coulomb potential. However, writing out M_{fi} to order $(v/c)^2$ will yield the Breit Hamiltonian which includes spin-orbit, spin-spin and tensor terms.

A similar procedure has been attempted in QCD in order to incorporate spin-dependent effects. The work of Eichten and Feinberg [20] and Gromes [21,22] has led to a potential of the following form:

$$V = \varepsilon(r) + \frac{1}{2m^2}\left[\frac{1}{r}\frac{d}{dr}(3\varepsilon + 4V_1)\right] \vec{L}.\vec{S} + \frac{1}{12m^2} V_2 \; S_{12} + \frac{1}{3m^2} V_3 \; \vec{s}_1.\vec{s}_2$$

Here, m is the quark mass and $\varepsilon(r)$ is the static (non-relativistic) potential. ε, V_1, V_2 and V_3 are quantities to be determined from QCD. The tensor operator, S_{12}, is given by $S_{12} = 3(\vec{\sigma}_1.\vec{r})(\vec{\sigma}_2.\vec{r})/r^2 - \vec{\sigma}_1.\vec{\sigma}_2$ where $\vec{\sigma} = 2\vec{s}$.

The three spin-dependent potentials depend on the Lorentz structure of the exchange operator. For vector exchange we have [22]:

$$V_1 = 0 \; ; \; V_2 = -\left(\frac{d^2\varepsilon}{dr^2} - \frac{1}{r}\frac{d\varepsilon}{dr}\right) \; ; \; V_3 = 2\nabla^2\varepsilon \; ,$$

while a pure scalar potential gives:

$$V_1 = -\varepsilon; \; V_2 = V_3 = 0.$$

The quantities ε, V_1, V_2 and V_3 are not yet explicitly derived within QCD. However, in ref. [20] formal expressions for these quantities are given within the formalism of lattice gauge theories. Several Monte Carlo simulations have been performed attempting to determine the potentials. Although larger simulations are desireable, the first results seem to indicate that the long range QCD potential is effectively of a scalar type [23,24].

Note that the results above reproduce the Breit Hamiltonian of QED. This justifies the early, purely phenomenological generalizations of the Breit Hamiltonian employed in order to describe the mass splittings of charmonium. In ref. [25], the long range potential, V_{conf}, is divided into a vector and a scalar part. The short range potential, V_c, is assumed to be of the vector type, stemming from one gluon exchange. The potential is therefore the sum of three parts:

$$V = V_c + V_v + V_s$$

where $V_v = \eta V_{conf}$ and $V_s = (1-\eta)V_{conf}$.

The resulting spin dependent potential is [14,25].

$$V(r) = \frac{1}{2m^2}\left(\frac{4c}{r^3} + 4(1+\kappa)\frac{1}{r}\frac{dV_v}{dr} - \frac{1}{r}\frac{dV}{dr} \right) \vec{L}.\vec{S}$$

$$+ \frac{2}{3m^2}\left(4\pi c\,\delta(\vec{r}) + (1+\kappa)^2\, \nabla^2 V_v(r)\right) \vec{s}_1.\vec{s}_2$$

$$+ \frac{1}{12m^2}\left(\frac{3c}{r^3} + (1+\kappa)^2\left(\frac{1}{r}\frac{dV_v}{dr} - \frac{d^2V_v}{dr^2}\right) \right) S_{12}$$

where $c = 4\alpha_s/3$ and κ is the quark anomalous magnetic moment, another adjustable parameter. The last term in the $\vec{L}.\vec{S}$ part may be thought of as due to Thomas precession, and is independent of the parameter η.

The tensor term does not contribute to the ψ-η_c splitting. The first estimates of this splitting assumed that the potential was dominantly of a Coulomb type. This gave a hyperfine splitting which was much too small[26]. However, assuming that the confining forces also played a role gave improved results[27].

For the χ_J splittings, the long range forces dominate. Neglecting the tensor term of the potential, we have the following ratio:

$$\frac{M_{\chi_2} - M_{\chi_1}}{M_{\chi_1} - M_{\chi_0}} = 2$$

Experimentally, this ratio is ≈ 0.5!. Thus, the tensor term must be of importance. Schnitzer [25] notes that for a linear + Coulomb potential, this ratio must be greater than .8 for a pure vector potential, and no anomalous magnetic moment ($\eta=1$, $\kappa=0$). Hence, we must allow for either a large anomalous magnetic moment, or the effective coupling of the confining potential must be of a mainly scalar type. Most models seem to support scalar confinement (e.g. ref. [28]).

An independent test of the nature of the confining potential would be the determination of the $^1P_1$ mass, which, in the limit of vanishing spin-spin forces, is given by:

$$M_{^1P_1} = (5/9)M_{\chi_2} + (3/9)M_{\chi_1} + (1/9)M_{\chi_0}$$

A mass of the $^1P_1$ close to this, would serve as an indication that the long range QCD forces are effectively of a scalar type; noting that only the vector part of the potential contributes to the spin-spin and tensor terms.

1.4.4 Width of Charmonium

The lowest lying charmonium states have masses which are below the threshold for production of a pair of charmed mesons. Thus, hadronic decays of these states are hindered by the Zweig rule which states that decay modes where quark lines are broken, are suppressed. This explains the narrowness of the low lying states, and also the large radiative branching ratios of the first exited states. In many ways, the charmonium system is similar to a system consisting of an electron-positron pair, positronium. Numerous calculations have been performed on this system [29,30]. These calculations may naively be carried over to a charmonium system decaying into gluons, which in turn transform into hadrons with unit probability. Furthermore, leptonic widths and widths of decays into photons are predicted by direct use of the positronium formulae. Table 1.2 gives some expected properties of the hadronic widths of various charmonium states.

A few qualitative arguments may be given in order to explain the relative widths of the different states. Firstly, we must mention that one-gluon intermediate states are forbidden due to conservation of colour. We also note Yang's theorem [33], stating that a spin one object may not decay into two massless spin one particles (such as real gluons and photons) This rule does however not apply to virtual (heavy) gluons where one of the gluons transforms into a $q\bar{q}$ pair. Hence, the decay $^3P_1 \rightarrow gq\bar{q}$ is possible. Moreover, while a two gluon state is c-even, a three gluon state may be both c-even and c-odd since the two singlets which may be formed with three gluons, have opposite charge conjugation (details in [31]). Hence, $^1P_1$ and the $^3S_1$-states must decay via three gluons, the $^1S_0$, $^3P_0$ and the $^3P_2$ states may decay via two gluons, and finally the $^3P_1$ state may decay through three gluons or a $gq\bar{q}$ intermediate state.

State	Dominant hadronic decay mode	Hadronic Width (MeV)	
		0 order QCD	Measured
η_c	2g	5.6 *	12.4 ± 4.1
χ_0	2g	2.4 ± .9 **	11.0 ± 2.0
χ_1	$3g/gq\bar{q}$	≈ 0.2 **	< 1.0
χ_2	2g	0.6 ± 0.3 **	3.0 ± 0.7
$^1P_1$	3g	0.07-.35 *	-
η_c'	2g	2.4 *	-
ψ'	3g	.02 *	.05± 0.01

<u>Table 1.2:</u> Hadronic widths of charmonium. Calculations from [31] (*), and [32] (**). The J/ψ width is input for all calculations. One should bear in mind that quite a few experimental facts have changed since the quantities in [31] were calculated. The measured widths include R704 results. The quoted ψ' width exclude all "radiative" hadronic transitions to the ψ.

The actual widths of the states depend on the properties of the wave functions at the origin. These are in turn to be determined from the model dependent potential. However, some information on the wave functions may be extracted by considering the electromagnetic decays, which are exactly calculated in QED. For example, we deduce from the observed electronic width of the J/ψ and the Van Royen-Weisskopf formula [29]:

$$\Gamma(\psi \rightarrow e^+e^-) = \frac{4e_c^2\alpha^2}{M_\psi^2}|R(0)|^2$$

that $|R(0)|^2 \approx .45\ \mathrm{GeV}^3$.

Furthermore, we may make a crude estimate of α_s, using the ratio between the formula above and the generalized $e^+e^- \to 3\gamma$ formula[30,14].

$$\Gamma(\psi \to \mathrm{hadrons}) = \frac{40}{81\pi}(\pi^2 - 9)\frac{\alpha_s^3}{M_\psi^2}|R(0)|^2$$

The wave function at the origin cancels and we obtain $\alpha_s \approx .18$ by using the experimentally observed widths.

The widths of the χ_J states depend on the derivative of the wavefunction at the origin. Generalizing the positronium formulae and using a value of α_s of the order of .2, the widths come out a lot narrower than actually measured. Second order corrections are thus large but unfortunately very difficult to estimate.

1.4.5 Radiative Transitions.

All exited charmonium states should decay into lower lying states by the emission of a photon. The spontaneos emission of photons is due to the interaction of the quarks with the electromagnetic field which is due to the electric charge ,eq, of the quarks. The non relativistic interaction Hamiltonian is given by:

$$H_I = H_E + H_M = -e\sum_a \frac{q_a}{m_a}\vec{A}_a\cdot\vec{p}_a - e\sum_a \frac{q_a}{2m_a}\vec{\sigma}_a\cdot\vec{B}_a$$

where the sum runs over the quarks and $\vec{A}$ is the electromagnetic potential. $\vec{B}$ is the magnetic field, given by $\vec{\nabla}\times\vec{A}$. The first term in H_I causes electric transitions, e.g. those with $\Delta L=1$ and $\Delta S=0$, while the second term involves the spin operator causing $\Delta S=1$ transitions. The transition elements for the various processes are calculated by expressing the potential as:

$$\vec{A}(r) = \vec{\varepsilon}\, e^{-i\,\vec{k}.\vec{r}}$$

where $\vec{\varepsilon}$ is the polarisation vector and $\vec{k}$ is the momentum of the emitted photon. In the dipole approximation, only the zero order term is retained in the expansion of the exponential. This expansion thus assumes that $\vec{k}.\vec{r}$ is much smaller than one. However, for $\chi_J \rightarrow \gamma\,\psi$ transitions, this parameter is of the order of unity. Hence, higher order terms may contribute significantly to these transitions.

While only poor measurements of the total widths of the χ_J states exist, their branching ratios to $\gamma\psi$ are fairly well measured. With this experimental input, the total widths may be estimated by using the calculations of the radiative widths. This procedure seems to produce widths which are larger than those estimated from zero order QCD .

1.5 Charmonium in Antiproton-Proton Collisions.

Most of the experimental data on charmonium come from e^+e^- annihilation. This means that the charmonium states that do not carry the quantum numbers of the photon will be reached mainly through decays of higher lying states. This results in rather poor measurements of the properties of these states, as is clearly seen in table 1.1.

In antiproton-proton collisions, all states may in principle be formed directly. Hence mass and width measurements depend on the beam characteristics rather than detector performance. In the limit of massless quarks, the QCD helicity selection rule prohibits formation of states with net helicity zero. The validity of this rule is however questionable at charmonium energies. Measurements of the angular distribution in $e^+e^- \rightarrow p\bar{p}$ [34,35] show that:

$$\frac{d\sigma}{d\theta} \propto 1 + .6\cos^2(\theta)$$

This angular distribution is parametrized as:

$$\frac{d\sigma}{d\theta} \propto 1 + (B_1^2 - B_0^2)/(B_1^2 + B_0^2)\cos^2(\theta)$$

where B_0 and B_1 are the net helicity components 0 and 1 respectively. Thus, the experimental measurement yields $(B_0/B_1)^2 \approx .25$. Hence it seems reasonable to assume that all charmonium states may be formed in $p\bar{p}$ collisions, although the formation of some states will be suppressed by a factor of four if they must be formed through net helicity zero (e.g. the $^1S_0$ states and the $^1P_1$ state).

The cross section for charmonium formation as function of the centre of mass energy, E, is given by the Breit-Wigner formula:

$$\sigma(E) = \pi\lambda\!\!\!^-{}^2 \frac{(2J+1)}{(2S_1+1)(2S_2+1)} \times \frac{B_i B_f \quad \Gamma^2}{(E-M_r)^2 + (\Gamma/2)^2}$$

where $\lambda\!\!\!^-$ is the de Broglie wavelength of the initial state, J is the spin of the resonance, S_1 and S_2 are the spins of the initial particles, B_i and B_f are branching ratios to initial and final states, Γ is the total width of the resonance, and M_r is the resonance mass.

The energy spread of the beam will be of great importance when estimating the rate at which the resonances may be formed, whenever the widths of the charmonium states are of the same order of magnitude as the expected energy spread of the beam. The formation rate is thus:

$$R = \int r(E)\, dE$$

where

$$r(E) = \sigma(E)L(E)$$

and L(E) is the interaction luminosity. This rate is expected to be of the order of 0.05-1 per nb^{-1} for realistic beam characteristics and feasible estimates of branching ratios and detector efficiencies [36].

Suitable final states have to be picked out for detection. Hadronic final states will be very hard to distinguish from the background, since this background rate is at 7×10^{7} per nb^{-1}. However, electromagnetic final states may be picked out in a large hadronic background. These final states are indeed those which are detected in the experiment R704.

2. DESCRIPTION OF THE R704 EXPERIMENT.

2.1 Introduction.

Once it became clear that the ideas of stochastic cooling actually worked in practice [42], the developement and construction of the CERN antiproton complex started. The subsequent success of the operation of the antiproton accumulator, made antiprotons available for exeperimenters in much higher numbers than what was previously possible.

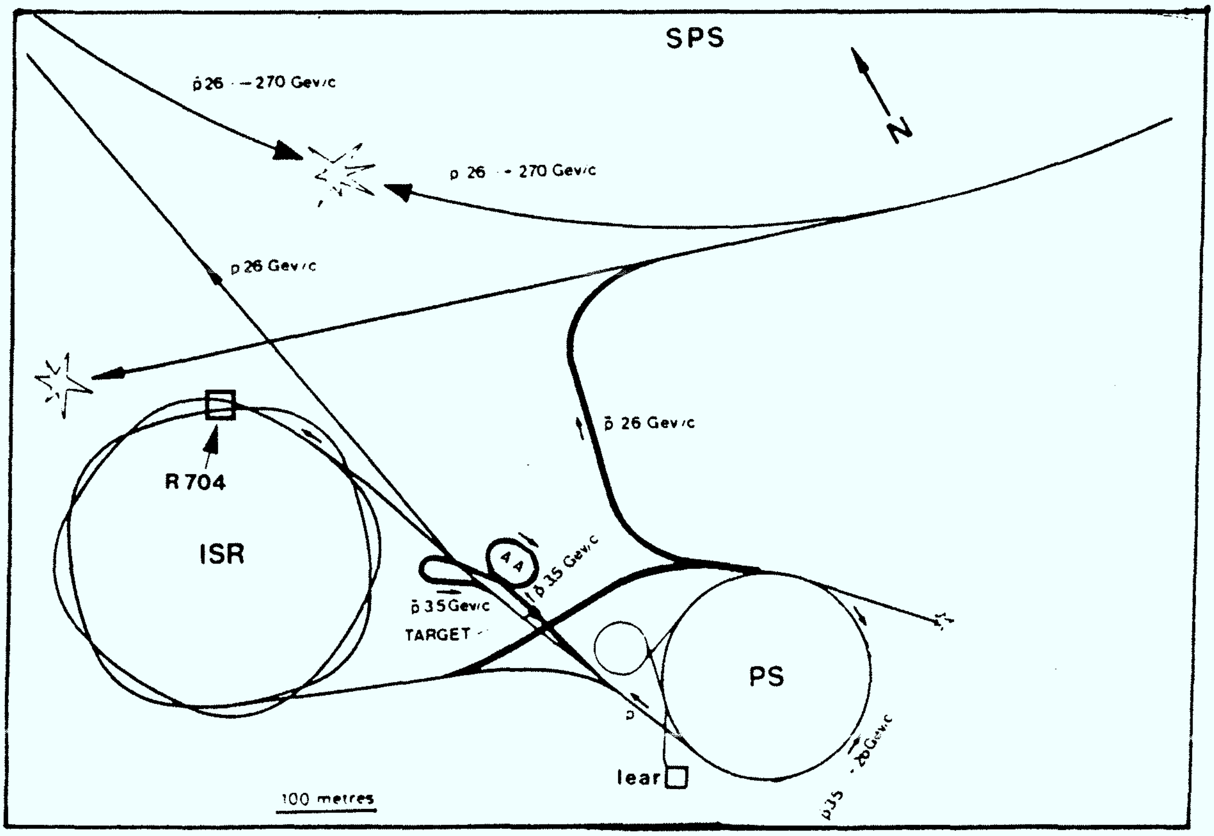

Fig. 2.1: The CERN antiproton complex. From [45].

In the experiment R704, proposed in 1980 [36], intense antiproton beams circulated in the ISR, and collided with a clustered hydrogen gas "jet" target. In this way, antiproton-proton collision luminosities larger than 10^{30} cm^{-2} s^{-1} were obtained. The aim of the experiment was to form charmonium directly in $p\bar{p}$ collisions, in particular the states which are not directly accessible in e^+e^- collisions, and provide new, improved measurements of masses,widths and some branching ratios of these states. In this chapter we describe the antiproton beam system, the gas-jet target system and the R704 detector which is designed to pick a signal of about 100 pb out of a total cross section of 70 mb by tagging electromagnetic final states. Fig. 2.1 shows an overview of the CERN antiproton complex.

2.2 Antiprotons for R704.

The antiprotons are produced by bombarding a tungsten target with protons at a momentum of 26 GeV/c. For a pulse of 10^{13} protons hitting the target, some 2.5×10^{7} antiprotons are collected in the Antiproton Accumulator (the AA) at a momentum of 3.5 GeV/c. Here they are precooled for two seconds before they are displaced to the innermost side of the AA, where they are merged with the rest of the antiproton stack. This procedure takes place within the .4 seconds available before a new bunch of antiprotons is collected. The production cycle has a repetition period of 2.4 s. Accumulating antiprotons for about 24 hours should leave a stack of 1 - 2 x 10^{11} antiprotons in the AA available for physics [43].

Several modifications of the beam handling system of ring 2 of the ISR were necessary before it could operate at the momenta required for charmonium formation. Contrary to the normal ISR momenta of 26-31 GeV/c, operation was requested in the momentum range between 3.5 and 6.5 GeV/c. These energies are below the ISR transition energy, necessitating a 180^0 change of phase of the RF system. Furthermore, covering this energy range requires the RF system to cover a frequency range of about 200 kHz (from 9.2 to 9.4 MHz), whereas a frequency sweep of 7 kHz is sufficient to cover the whole ISR range above 11 GeV/c. For this reason, the ISR frequency synthesizer was replaced. Another problem was that the normal stacking procedure of the antiprotons in the ISR, i.e. transferring the antiprotons in small slices, would not work due to the large emittance of the 3.5 GeV/c antiproton bunches and the limited area of an ISR RF bucket. Furthermore, the ISR RF system could not recieve all AA antiprotons in one bunch because the smallest possible AA bunch would have a length of 85 ns and a $\Delta p/p$ of 10^{-3}, while the largest bunch the ISR RF system could trap would have a length of 50 ns and a $\Delta p/p$ of 10^{-3}. The PS could have been used to reduce the length of the bunch, but at the cost of deteriorating the momentum spread to an unacceptable level.

The solution to these problems was to refrain from using the PS and ISR RF systems, except for timing of the three machines, and to rely uniquely on the magnet settings to guide the antiprotons from the AA to the ISR. The antiprotons were transferred in two, possibly three slices, each 300ns long, making just half a turn in the PS before being injected into the ISR. Before the second pulse arrived, the antiprotons circulating in the ISR were displaced away from the injection orbit, and finally, after injection of the second pulse, the two pulses were merged by momentum cooling. The efficiency of this transfer was about 70% [44]. Fig. 2.2 shows ISR beam profiles at different stages of this procedure.

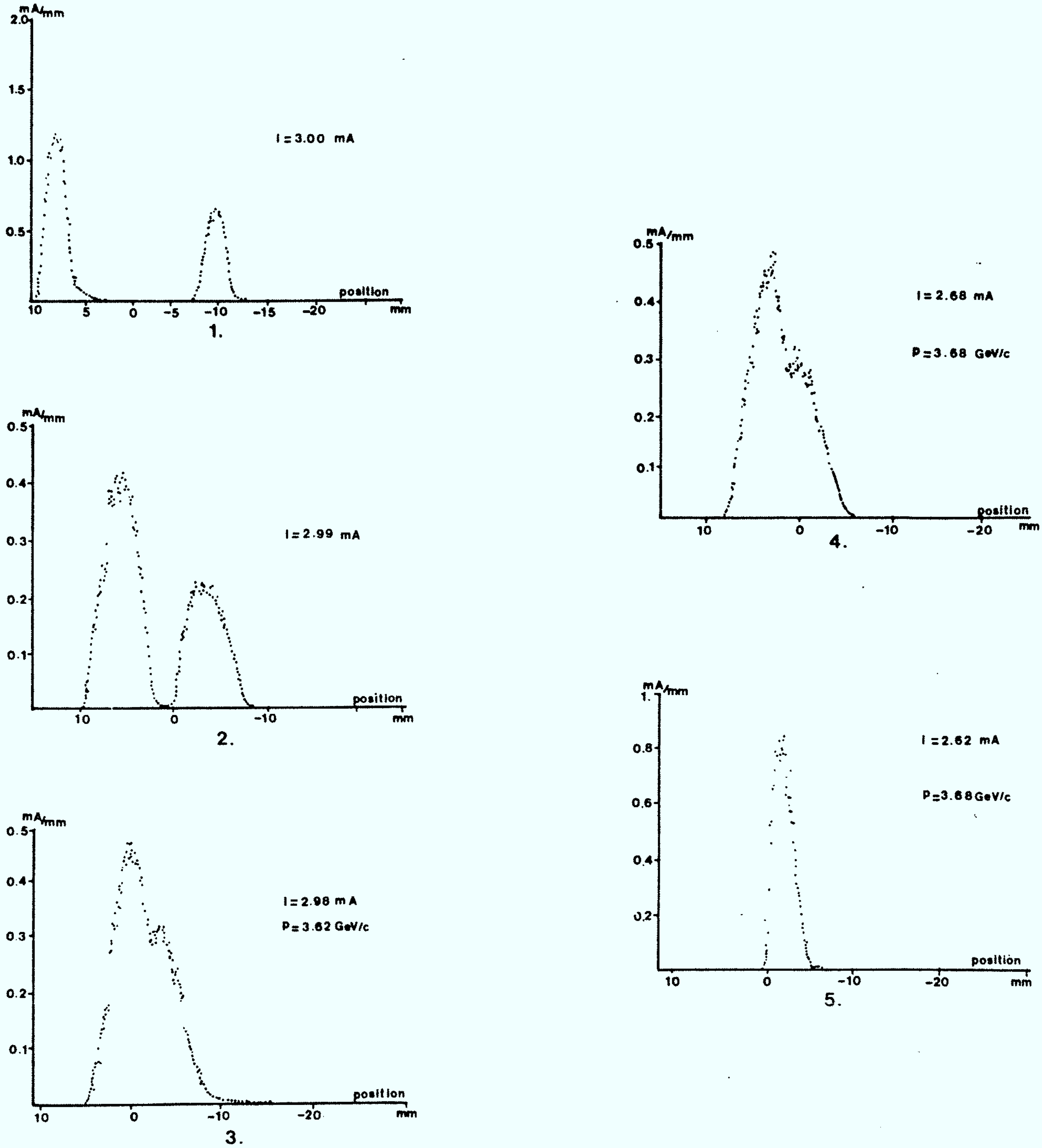

<u>Fig. 2.2:</u> Beam profiles at five stages of the injection procedure.
1. After displacement of the first pulse, a second one is injected at a different radial position.
2 -4. The two beams are merged by the momentum cooling system.
5. The beam profile after 10 hours of momentum cooling.
From [45].

Due to the internal gas-jet target, the stochastic cooling system was absolutely vital to prevent a too quick blow-up of the beam, and ensure a reasonable lifetime of the beam. Moreover, the momentum spread had to be kept as low as possible in order to keep the formation rates of the narrow charmonium resonances at reasonable levels. Low momentum spread was also necessary to fulfill the goals of the experiment, namely to perform accurate measurements of the masses and widths of several charmonium states. Both the vertical betatron cooling and the horizontal simultaneous betatron and momentum cooling system turned out to work very well. In fact, the minimum relative momentum spread obtained was smaller than $\pm 4\times10^{-4}$, while it would remain at about $\pm 5\times 10^{-4}$ throughout a typical physics run. This corresponds to a mass resolution of about 500 keV at the ψ energy. The half-life of the antiproton beam was about 60 hours, and a typical physics run would last for four to five days. A period of five days was also the longest duration of continuos operation of the target system before recycling the cryogenic pumps. Recycling the pumps required acces to the experimental area.

Due to the method of beam transfer, bunched beam acceleration was not possible. Instead, RF acceleration was obtained by the phase displacement method. Acceleration from 3.5 to 6 GeV/c by this method caused a beam loss of about 10%. The minimum momentum step using this method was 3-6 MeV/c. However, the beam momentum could be finely adjusted by using the cooling system to slightly shift the central position in the beam pipe.

It was of great importance to know the momentum calibration as accurately as possible. Initially, momentum measurements were performed by measuring the closed orbit and the revolution frequency of protons at each energy. This was only possible when operating in bunched mode, thus not during normal antiproton operation. At these low momenta, this method gave the most accurate measurement, and was used to cross-check the calibration of the magnetic field measurements later on. The systematic error of the momentum measurements turned out to be less than 1 MeV/c. This is nicely reflected in R704 measurement of the ψ mass, where we obtain a mass of the ψ of [45]:

$$m = 3096.95 \pm .1 \pm .27 \text{ MeV/c}^2$$

based on a sample of just 193 events of the type $p\bar{p} \to \psi \to e^+ e^-$. This may be compared with the world average value, $m = 3096.9 \pm .1$ MeV/c^2 [8].

2.3 Target System

The most original feature of this experiment is the target system consisting of a beam of clustered hydrogen molecules crossing the ISR beam tube. This system offered several advantages over conventional fixed targets. First of all, very high luminosities were obtainable, since the antiprotons circulating in the ISR ring for several days are passing through the target over and over again. Secondly, this system provides a very small interaction region of about 1 cm^3, which eases the design of the detector system, and facilitates the identification of several neutral final states, where the small interaction volume imposes a severe kinematical constraint on the events. Finally, very high momentum resolution is provided, since the blow up of the beam due to beam-target interactions is continously counteracted by the momentum cooling system.

The gas-jet system was required to produce a target thickness of 10^{14}

atoms/cm^2 in order to provide the expected luminosity of 10^{31} $cm^{-2}s^{-1}$ with 3×10^{11} antiprotons circulating in the ISR. When designing the target system, great care had to be taken to prevent the ISR vacuum from deteriorating to an unacceptable level due to residual hydrogen gas stemming from the target, hence causing a too quick blow-up of the antiproton beam.

The final gas-jet design consisted of hydrogen gas at a pressure of 10-15 bar and a stable temperature of 77 K, expanding through a thin trumpet shaped nozzle(fig.2.3) with a diameter of just 30µm. The small diameter, much smaller than the mean free path of the gas molecules, is necessary for good directionality of the jet. A rather long trumpet shaped nozzle was found to give the best clusterisation of the jet, hence the optimum target density [44].

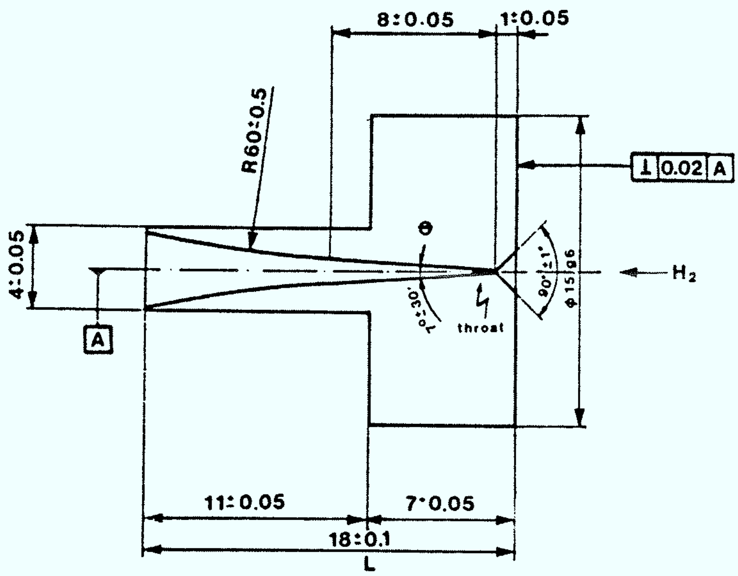

Fig. 2.3: The final design of the nozzle of the gas-jet system. From [44].

A sophisticated pumping and skimmer system was also required to keep the beam of H_2 clusters as narrow as possible, facilitating the collection of the gas in the sink system, and minimising the amount of residual gas in the ISR. The pumping system consisted of six vacuum pumps, three before the gas jet crosses the beam tube, and three pumps in the sink system (fig.2.4). The direction of the gas jet beam could be steered in order to maximize the antiproton proton interaction luminosity.

This target system worked beautifully throughout the whole experiment, and the maximum luminosity reached was 2.7×10^{30} $cm^{-2}s^{-1}$ for a stack of about 1.1×10^{11} antiprotons. The design luminosity of $10^{31}cm^{-2}s^{-1}$ was not reached because of the unexpectedly low number of antiprotons accumulated in the AA.

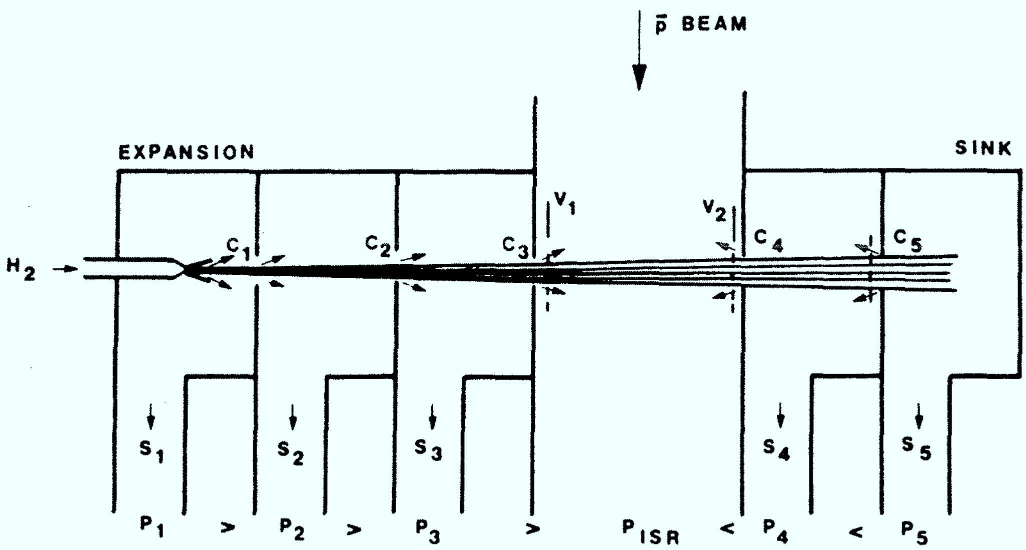

Fig. 2.4: Schematic overview of the vacuum pump and sink system. S_4 consists of two pumps. From [44]

2.4 Detectors

The R704 detector was non-magnetic, and may be divided into three main parts:

- The two main arms, which consisted of a set of detectors for charged particle identification and track reconstruction, followed by an electromagnetic calorimeter with high position resolution. The two arms were symmetrically arranged around the intraction vertex, and covered each 45 degrees in the azimuthal angle and ranges from 17 to 66 degrees in the polar angle.

- The veto counters, which nearly covered all the rest of the forward hemisphere. Apart from being used for vetoing an event, these counters could be used actively in the process of event identification.

- The luminosity monitoring detectors which were detecting low energy recoiling protons.

Fig 2.5 shows a general overview of the experimental area, with the target system and the two main arms. In the following we describe the different parts of the main arms, the veto system and the luminosity detectors.

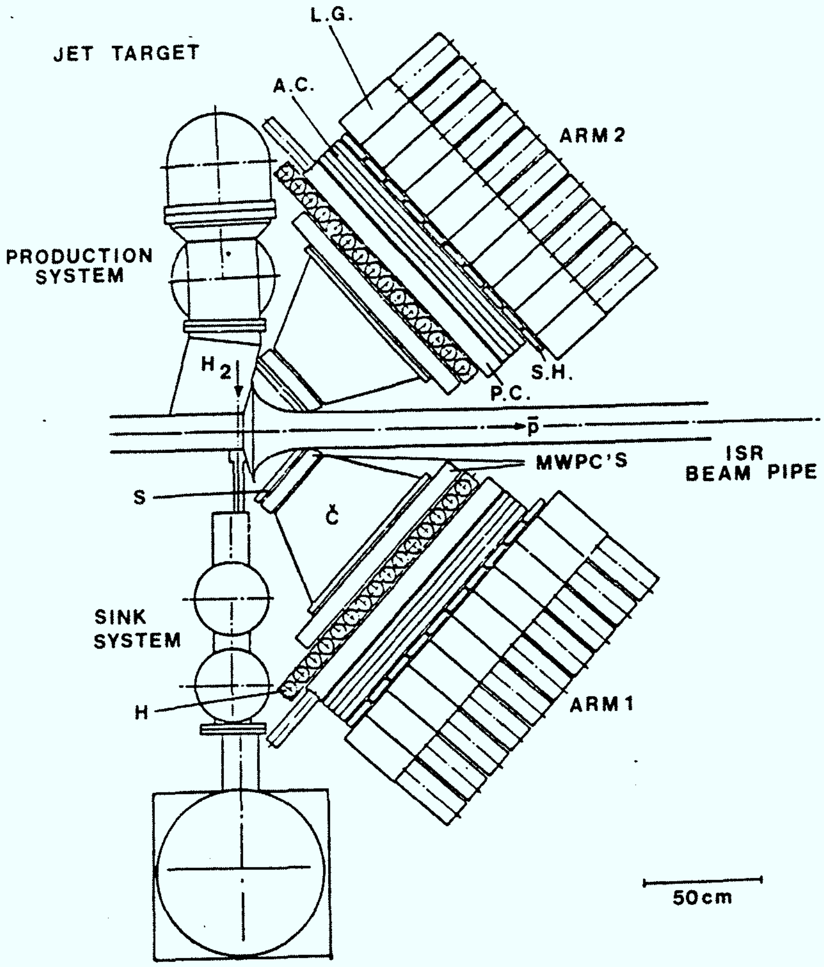

S	Scintillator
MWPC	Digital chambers
C	Cherenkov
H	Hodoscope
PC	Precalorimeter
AC	Analog chambers
SH	Shower hodoscope
LG	Lead glass

Fig. 2.5: General overview of the experimetal setup, showing the two main detector arms and the actual layout of the target system. From [44].

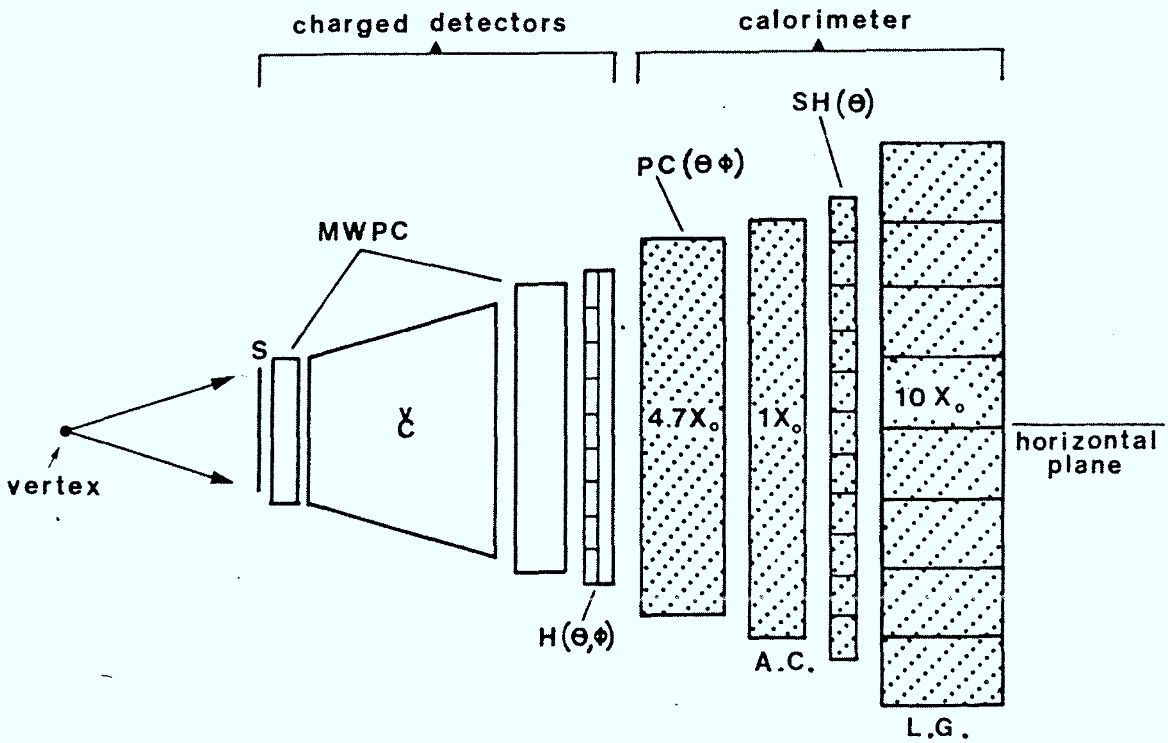

Fig. 2.6: Schematic sketch of one of the detector arms. From [44].

2.4.1 The Main Arms.

Each detector arm consisted of a charged particle triggering and tracking device followed by an electromagnetic calorimeter. The first part consisted of trigger hodoscopes, a threshold Cerenkov counter for electron identification, and two MWPC chambers consisting of three wire planes each.

The calorimeter was designed to measure the position and energy of electromagnetic showers. We mainly searched final states with one energetic electron or photon in each detector arm. Due to the large background of events containing π^0s, one versus multishower discrimination was important. The calorimeter was divided longitudinally into three main parts, the middle one being a position sensitive device. The two outer parts, the precalorimeter and the lead glass, were used for measuring the energy of the incoming particles. A set of scintillators, the shower hodoscope, was placed between the precalorimeter and the lead glass for triggering purposes. Construction details and details concerning the monitoring may be found in [44] and [46].

Fig. 2.6 shows schematically one of the detector arms.

2.4.1.1 Trigger Hodoscopes.

In each arm, the trigger hodoscopes consisted of four sets of scintillator planes, S, $H\theta$, $H\varphi$ and SH (see fig. 2.6) The first, S, was placed in front of the detector arm, at a distance of 290 mm from the vertex region. It consisted of just one single scintillator plate, covering the whole detector acceptance. Its thickness was 5 mm, and except for providing a trigger signal, the pulse height of the signal was recorded.

The second set of scintillators consisted of ten vertical bars, each 87 mm wide, placed at a distance of 915 mm from the interaction region. The angular segmentation was $\Delta\theta = 4.9^0$. This hodoscope plane was followed by a plane of six wedge shaped scintillator bars, placed horizontally, each covering an azimuthal angle of 7.5^0 when seen from the interaction region. All these counters had a thickness of 10mm. Fig. 2.7 shows schematically the grid which was formed by these two planes.

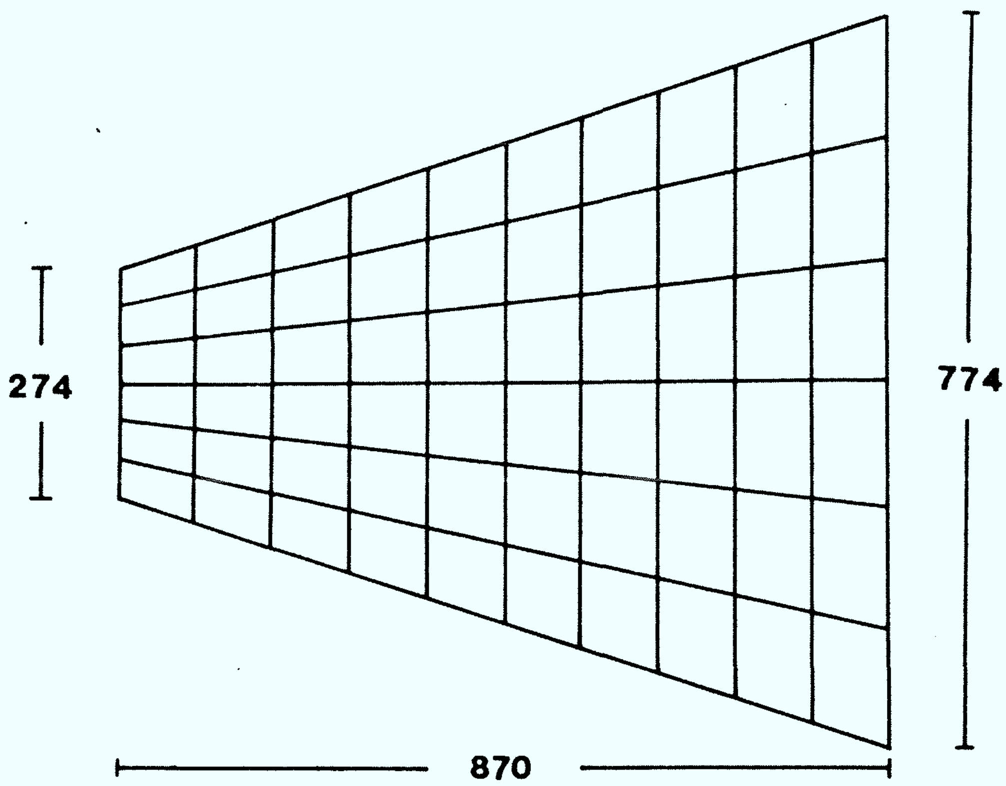

Fig. 2.7: Front view of the grid formed by the two hodoscope planes, $H\theta$ and $H\varphi$. Dimensions in mm. From [46].

The final scintillator plane is placed between the precalorimeter and the lead glass, and consists of 14 vertical scintillator bars, each 86 mm wide with a thickness of 10 mm. They should detect the neutral gamma rays after being converted in the precalorimeter.

2.4.1.2 The Cerenkov Counters

The purpose of the Cerenkov counters is to tag electrons at the trigger level. These counters were filled with freon-13 at atmospheric pressure. The detection threshold was .013 GeV/c for electrons and 3.68 GeV/c for pions. The two Cerenkov counters in coincidence greatly reduced the trigger rate. Each counter had a length of 450 mm and was placed between the two sets of MWPCs. The Cerenkov light was collected by two mirrors and viewed by two photomultipliers (fig.2.8). The average number of photoelectrons collected for a relativistic electron was 5.5. The Cerenkov signals were also integrated and the ADC converted result was written to tape.

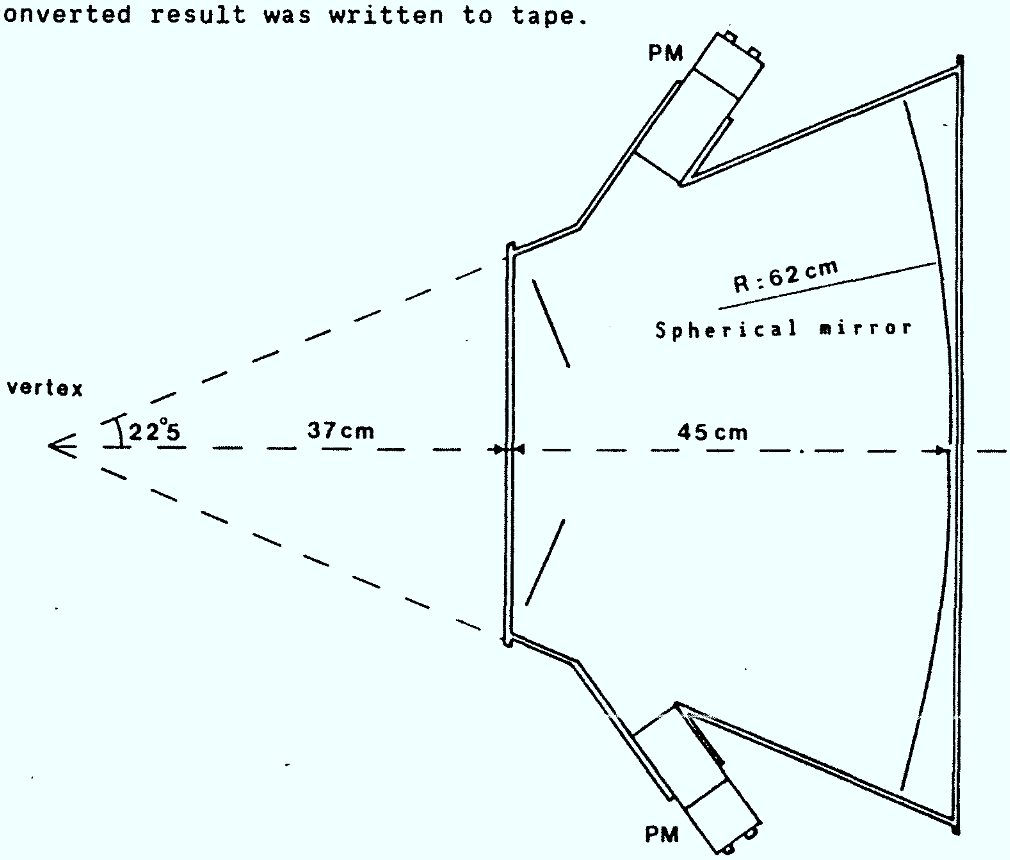

Fig. 2.8: Design of the Cerenkov counters. From [45].

2.4.1.3 The MultiWire Proportional Chambers.

Each arm had two sets of MWPCs, each consisting of three planes of wires. The relative orientation of the wires were as shown in fig. 2.9. The first chamber was placed at 300 mm from the vertex region, and the second one was at 825 mm from the vertex. The reconstruction efficiency was about 95% per arm, slightly variyng throughout the data taking periods. The gas mixture used in the MWPCs was 69.6% argon, 30% isobutane, and 0.4% freon. The high tension planes were made of mylar covered with graphite, and the operating voltage was typically 4kV. Table 2.1 summarises some features of the MWPCs. The angular resolution of reconstruction was about 4 mrad (fig 2.10).

		Chamber 1	Chamber 2
No of planes		3	3
Wire spacing		2mm	2mm
Wire diameter		20μm	20μm
No. of wires in X plane		150	384
No. of wires in Y plane		157	501
No. of wires in U (V) plane		180	501
Dimensions (fig.2.9)	L_1	140mm	460mm
	L_2	357mm	1117mm
	H	350mm	1059mm

Table 2.1: Mechanical properties of the MWPCs.

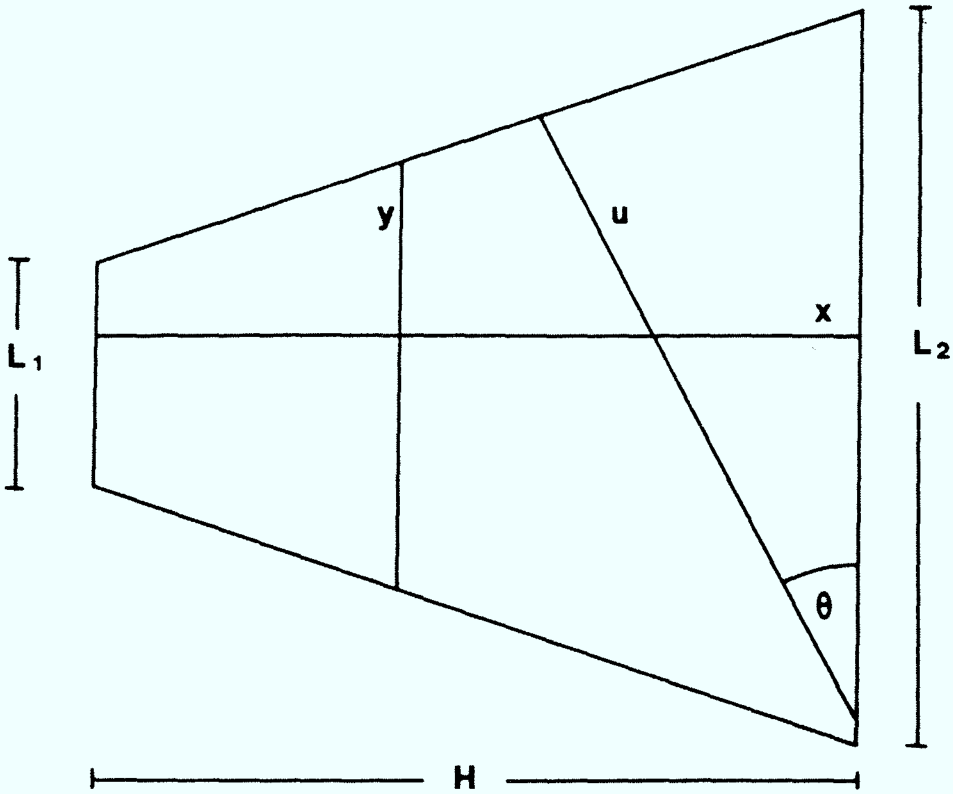

Fig. 2.9: Relative orientation of the wires in the MWPCs. $\theta=28^0$ for the large chambers, and $\theta=-28^0$ for the small ones. The dimensions are found in table 2.1. From [46].

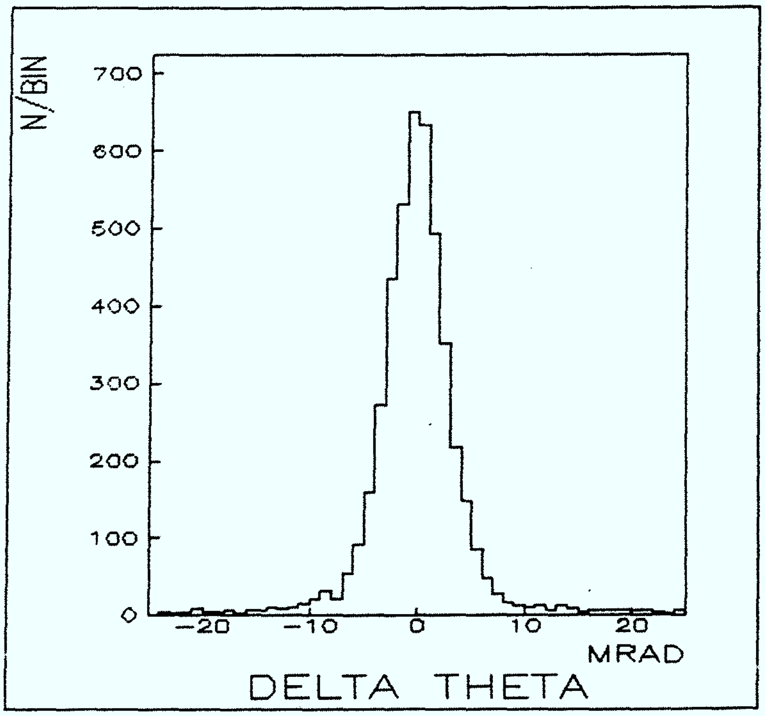

Fig.2.10: Angular resolution of the MWPCs. For elastic events, the plot shows expected minus reconstructed polar angle of the track in one arm, when the direction in the other arm is reconstructed.

2.4.1.4 The Precalorimeter.

The precalorimeter consisted of a lead-scintillator sandwich of length 4.7 X_0. The entrance face was an iron plate with a thickness of 1cm. Following this we find a sandwich consisting of ten layers of scintillator rods, each 0.5 cm thick, interspaced with nine sheets of lead of a thickness of 0.25 cm. The ten layers of scintillation counters were alternately segmented into 29 vertical and 14 horizontal wedge shaped rods as shown in fig 2.11. The scintillators had a thickness of 3.5 cm. The scintillator signals were read out by 29 + 14 PMs as indicated on the figure. In order to improve the dynamic range of the precalorimeter, the output signals were split into two parts, one containing 9/10 of the original signal, the other containing the remaining 1/10. The signals were time integrated and digitized in ADCs of the type LRS 2249A.

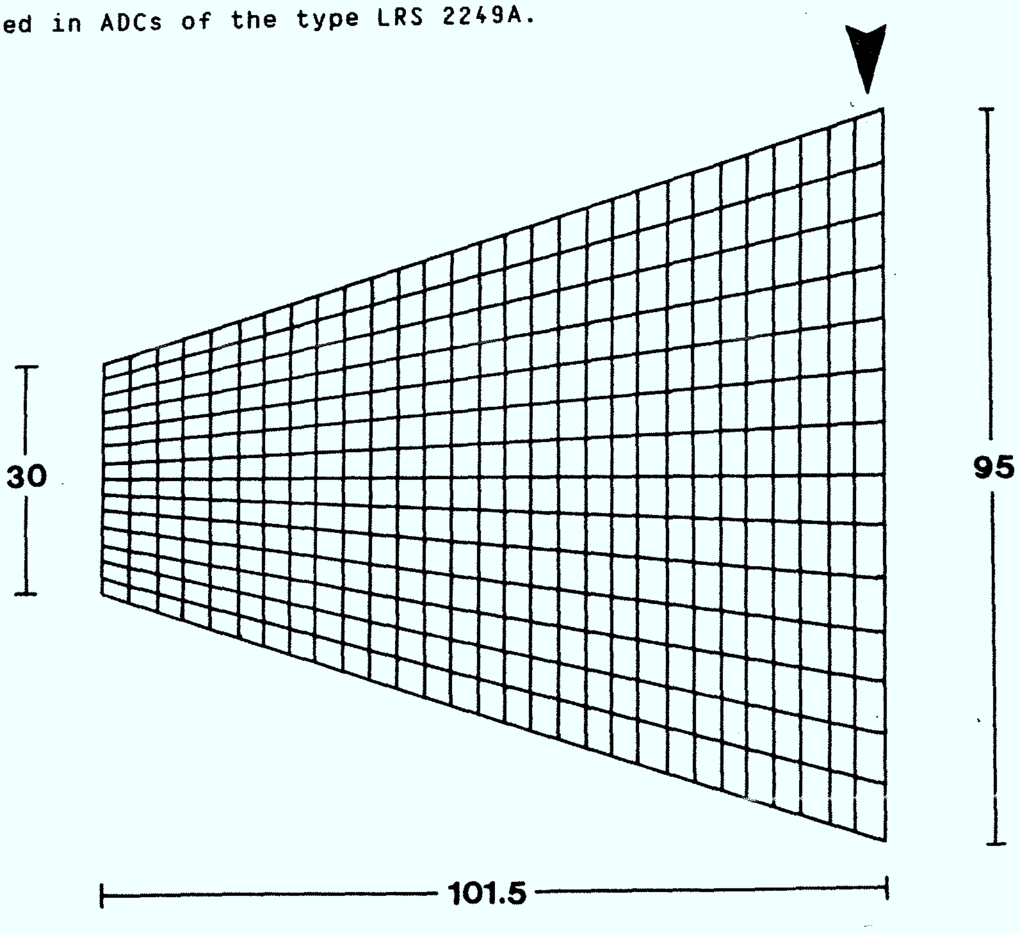

Fig.2.11: Front view of the grid formed by the precalorimeter scintillator bars. The arrow indicates a PM readout point. Dimensions in cm. From [46].

2.4.1.5 The Analog Chambers.

Each of the five chambers consisted of two cathode planes on each side of an anode plane. The anode plane was a set of wires at high tension. The cathodes were at ground potential. They were made of 9mm wide strips of copper, 1 mm apart. Only four of the five chambers were read out, the fifth chamber was a spare one, intended for use in case of breakdown of one of the other chambers. The signals from the strips were linearily amplified and integrated in ADCs of the type LRS 2282. A lead plate of thickness 1 mm is placed in between each chamber. The purpose of this was to absorb soft highly ionizing particles which may produce spurious signals in some of the strips, leading to double peaks in the signal distribution caused by a single shower event. Figs. 2.12 and 2.13 show the layout of the chambers. The amount of material in the set of analog chambers corresponded to $1X_0$.

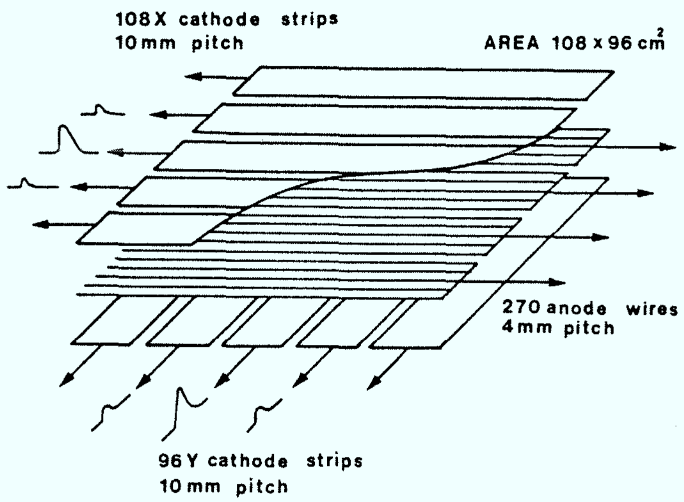

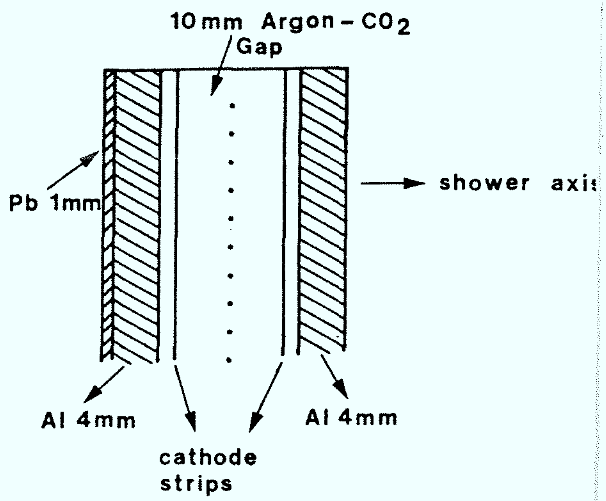

Fig.2.12: Layout of the analog chambers. From [44].

Fig.2.13: The longitudinal structure of the analog chambers. From [44].

2.4.1.6 The Lead Glass Wall.

The lead glass wall consisted of 66 blocks of dimensions 15 X 15 X 30.5 cm^3 of F2 glass from Schott [47]. Their length of 30.5 cm corresponds to 10 X_0 of material, ensuring full shower containment. The blocks were arranged as shown in fig. 2.14. Each block was viewed from behind by an EMI 9928KA phototube with a cathode diameter of 5 inches. The PM signals were digitized in LRS2249W ADCs. Construction details are found in [44] and [46].

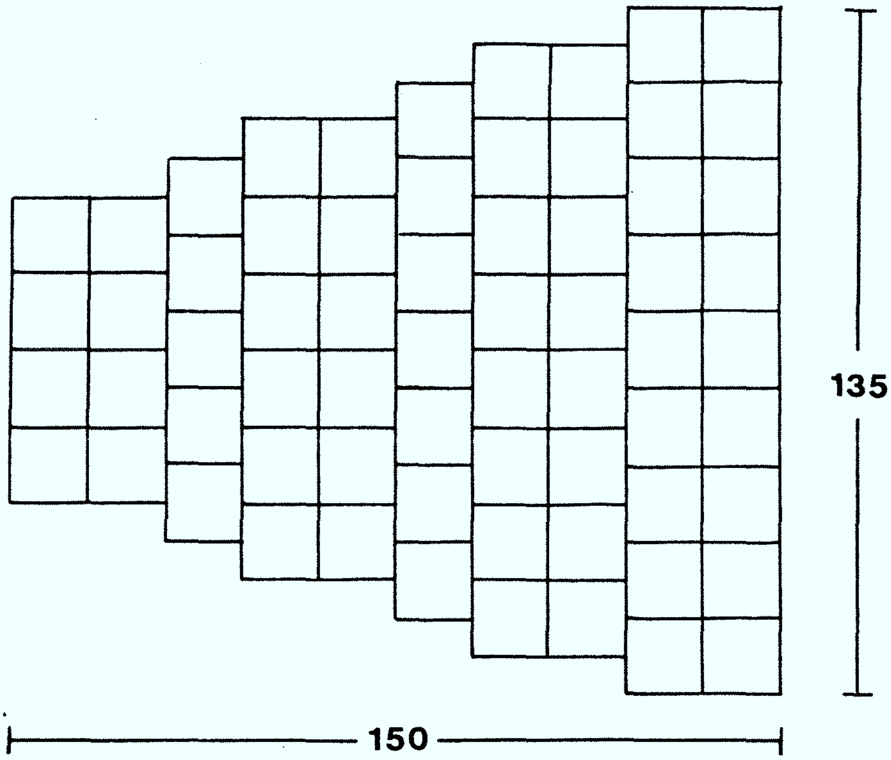

Fig.2.14: Front view of the lead glass wall. Dimensions in cm. From [46].

2.4.2 Veto Counters.

Most of the forward hemisphere not covered by the main arms, were covered by veto counters. The angular coverage of these counters is shown in fig.2.15. These counters were used actively in the detection of three body final states, e.g. the $e^+ e^- \gamma$ final state stemming from a χ_J decay. The vetos consisted of two parts, the "charged" and the "neutral" part. The charged part was a set of simple scintillator counters, while the neutral part consisted of lead-scintillator sandwiches, $4.5X_0$ long. Hence, these counters would detect photons causing electromagnetic showers. There were 50 of these counters, arranged as shown in fig 2.16. Coarse position resolution was provided by these counters.

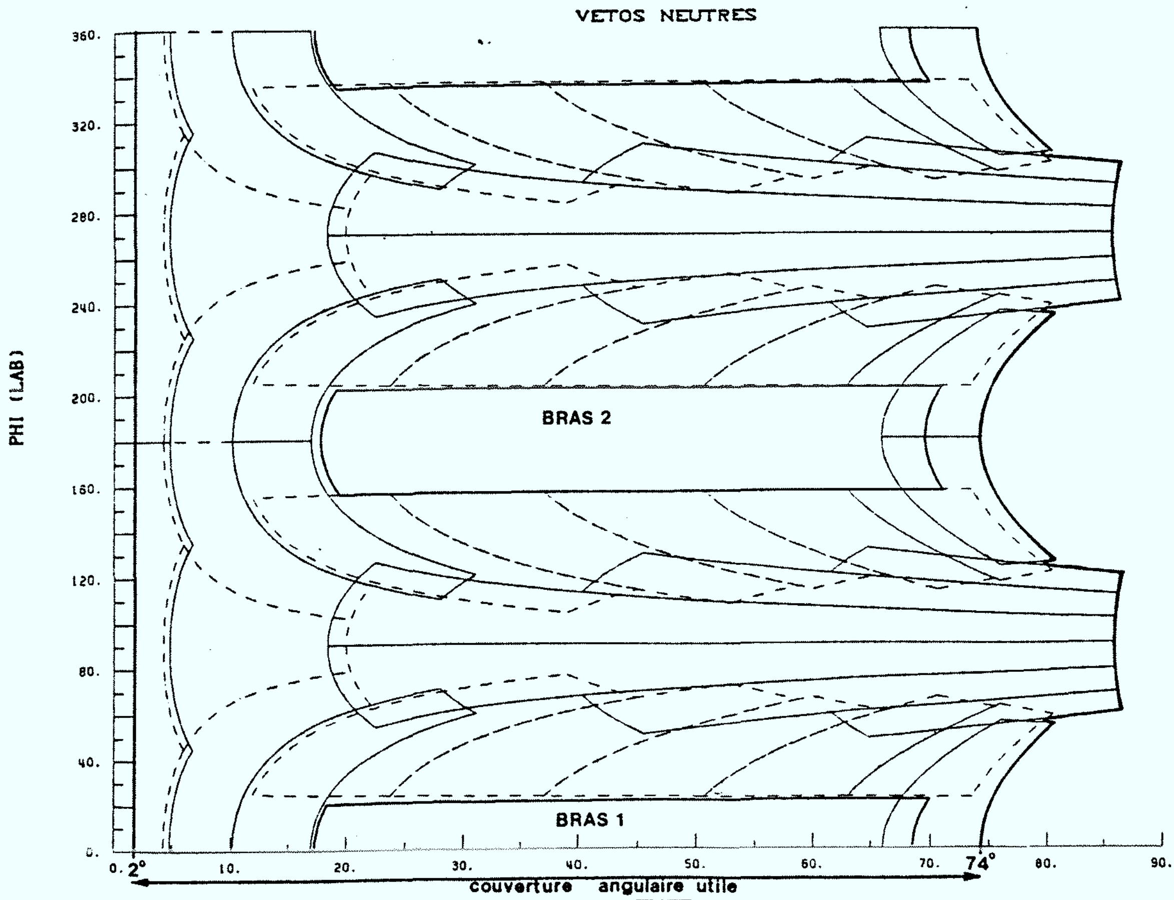

Fig.2.15: Angular coverage of veto counters. From [45].

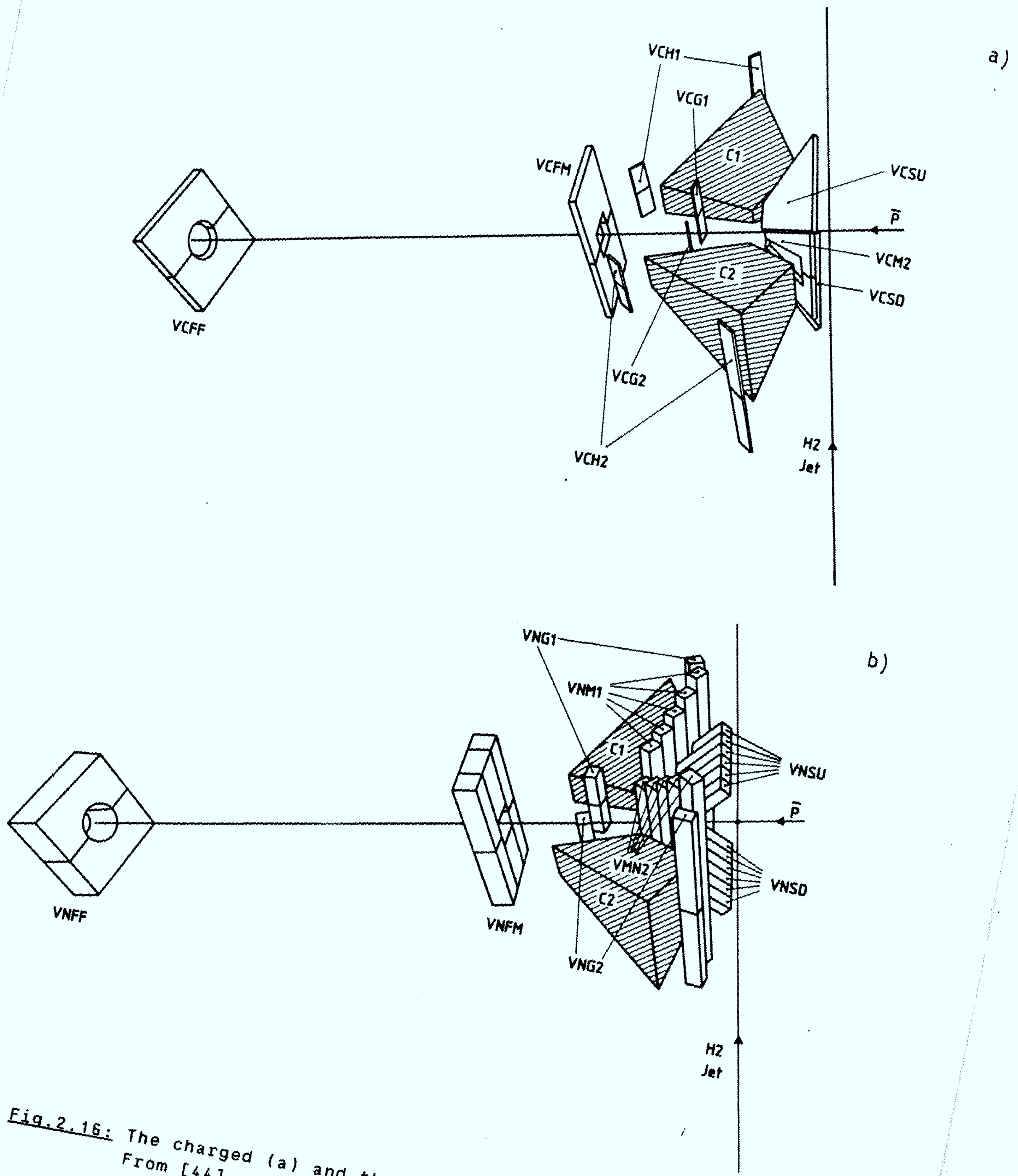

Fig.2.16: The charged (a) and the neutral (b) veto counters. From [44].

2.4.3 Luminosity Counters and Measurements.

The antiproton-proton interaction luminosity was measured by counting the rate of elastically scattered events in a momentum transfer range of $0.001 < -t < 0.005$ $(GeV/c)^2$. At these t, the protons recoil at angles close to 90^0 with respect to the antiproton beam. Eight silicon detectors measured the kinetic energy of the protons emerging at angles ranging from 82^0 to 90^0 with respect to the beam axis. Two of these were placed at an angle larger than 90^0, and measured the background rate. Six of the detectors were placed in the ISR vacuum, mounted in a trumpet shaped vessel (fig. 2.17). The two remainig ones were also placed in the vessel, but behind a thin stainless steel window, hence outside the ISR vacuum. The reason for this was that these detectors could not withstand the ISR bake-out temperature.

During a time interval ΔT, the number of protons detected is given by:

$$N = A\ L\ \Delta T \int_{t_2}^{t_1} dt(d\sigma/dt)$$

where t is the square of the four momentum transfer, A is the detecor acceptance, L is the inteaction luminosity, and $d\sigma/dt$ is the differential elastic cross-section. The limits of integration, were fixed by offline studies of the energy spectra produced by each detector. A plateau in the number of counts is clearly seen (fig.2.18), in the range of energy expected by the recoiling protons.

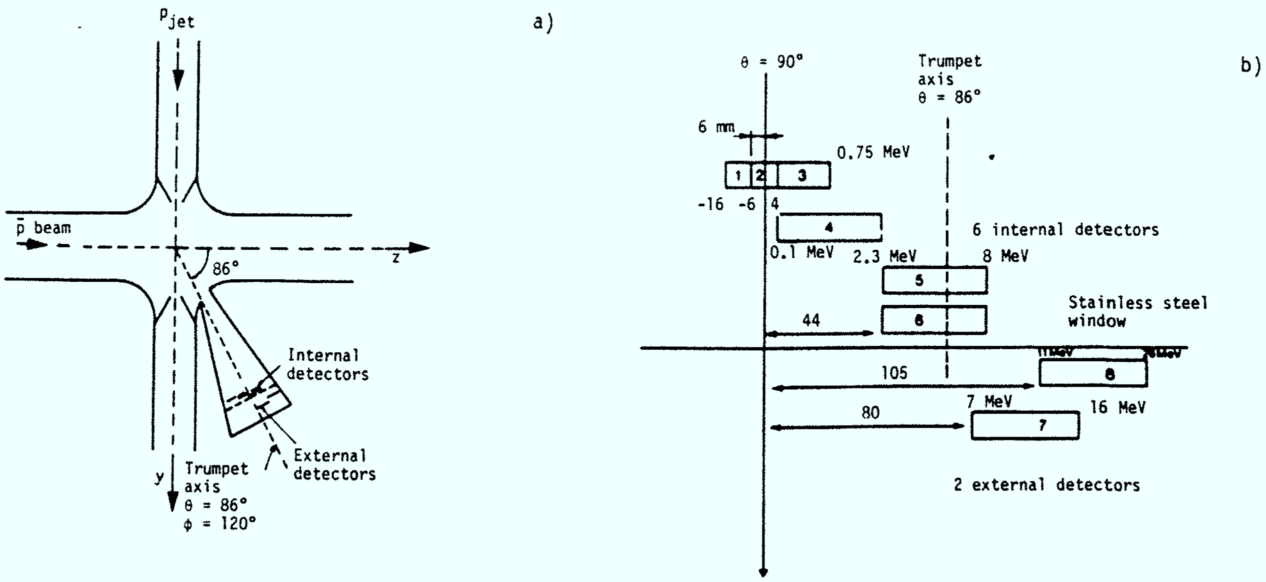

Fig.2.17: Set-up of the luminosity counters. a) Top view. b) A more detailed view of the position of the various counters From [44].

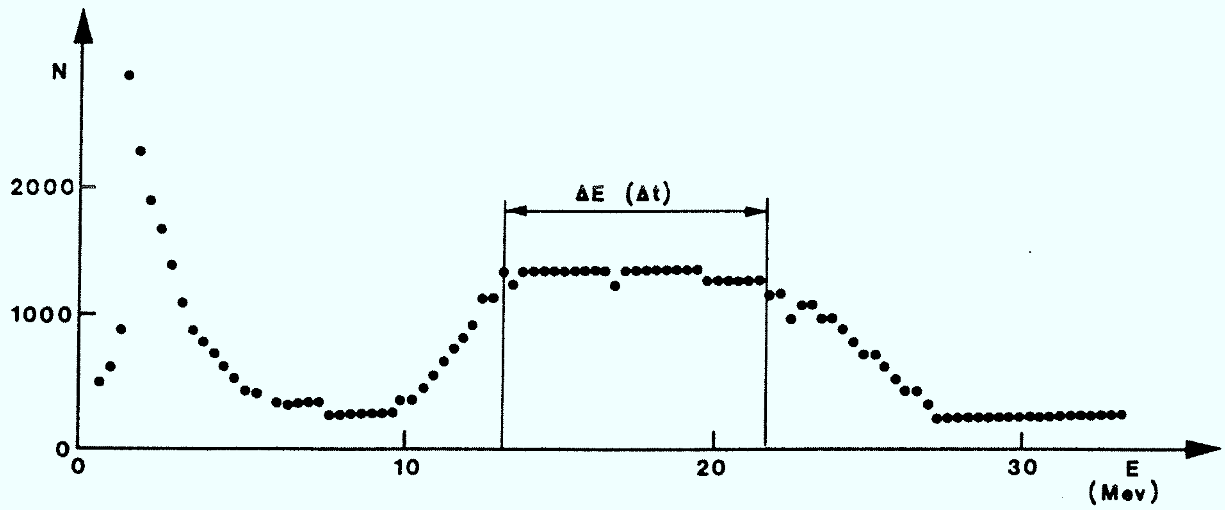

Fig.2.18: Energy spectrum from one of the luminosity counters, showing the backgound peak due to minimum ionizing particles, and the broad plateau due to protons within the momentum transfer range covered by the detector. From [44].

The data aquisition from the luminosity detectors was taken care of by a microprocessor producing energy spectra such as the one shown in fig.2.18. Once every ten minutes, data were transferred from the microprocessor to tape via the Nord 10 computer. The processor also gave an online estimate of the luminosity.

Three factors determined the accuracy of the luminosity measurements. These were the accuracy of the intergration limits, the precision with which the differential cross section is known (from earlier dedicated experiments), and finally there was an incertitude in the estimated geometrical acceptance. The luminosity measurements were estimated to have an uncertainty of about 5% [44]. Relative luminosities were measured with higher precision.

As a cross check of the stability of the luminosity system, two simple coincidence count rates were measured, the first one being the rate of coincidences between S1 and S2, while the second one was the count rate of coincidences between two veto counters (VCSU and VCSD in fig. 2.16)

2.5 Calibration of the Calorimeters.

The energy measurements of electrons and photons were performed by the precalorimeter and the lead glass wall. Calibration of each arm was done separately in an electron beam, where the calorimeter setup was simulated. In the setup, the analog chambers were simulated by placing a configuration of material equivalent to the analog chambers and the shower hodoscopes between the precalorimeter and the lead glass. The whole setup was placed on a support which could be rotated about a point simulating the interaction point. Hence the incident electrons were at the exact angle expected for the actual data-taking.

The first part of the calibration consisted of finding the response of each detector element to a minimum ionizing particle. This eneabled us later on to express the calorimeter response in units of the equivalent number of minimum ionizing particles (mip) necessary to produce the measured response. The unit mip should be independent of the individual detector response and corresponded to a definite electron energy for each detector type. In the precalorimeter, one mip corresponded to an energy deposition of roughly 35 MeV, while one mip in the lead glass corresponded to about 350 MeV.

The second step of the calibration procedure consisted of exposing the calorimeter to electrons, and recording the detector response at several points on the detector. The individual detector responses were then expressed in units of mips and calibration constants were found by comparing the response to the known incident energy.

The algorithm used for energy reconstruction is described in ref. [44], and the energy resolution of the calorimeter was $\Delta E(FWHM)/E = 29\%/\sqrt{E}$. The moderate resolution obtained is of course due to the analog chambers which are inactive in the energy reconstruction. The mass resolution of reconstructed $\psi \to e^+e^-$ events was 16% (FWHM) (see fig. 3.2 in chapter 3).Since the mass measurements of this experiment is performed by measuring the beam momentum, the energy resolution of the calorimeter is not an important parameter. The important point is the ability to identify electrons and photons with a good rejection of hadrons and muons.

2.6 Trigger and Data Aquisition.

In this experiment, we were mainly looking for final states consisting of electrons and photons. It was mandatory to define triggers with very large rejection power in order to be able to handle the large background of hadronic final states. Except for kinematical correlations, the electrons and photons were recognized by having all their energy deposited in the calorimeter. Furthermore, electrons were identified by the signals they produced in the Cerenkov counters.

The data aquisition system could handle two different physics triggers simultanously. Normally one charged and one neutral final state were sought at the same time. In addition, a monitoring trigger activated the calorimeter monitoring system at regular intervals.

The physics trigger logic is arranged at three levels. The first level of decision was made within 50 ns, and was based on information from the hodoscopes, the Cerenkov counters and the veto system. Four sets of coincidence matrices were used, one for charged correlations in the polar angle (MHθ), one for azimuthal correlations (MHφ), and two for correlations within the shower hodoscopes (MSH1 and MSH2). The matrix settings (MHθ, MHφ, MSH1 and MSH2) for the different states were found by Monte Carlo simulations. Two Programmable Logic Units (PLUs) of the type LRS 4508 were in use. The LRS 4508 consists of two separate units with eight inputs, and can be programmed to give a signal according to any configuration of the eight input signals. The inputs to the first PLU were signals from S_1, S_2, C_1, C_2 and the charged vetoes (VC), and the outputs produced logical "yes" or "no" according to sought logical configurations between these inputs. Inputs to the second PLU were the outputs from the matrices and from the first PLU. The outputs from this unit were the two first level physics triggers. For example, the two triggers while searching inclusive $\psi \to e^+e^-$ and $\gamma\gamma$ pairs would be the following:

$$T1(e^+e^- + X) = S_1 * S_2 * C_1 * C_2 * MH\theta * MH\varphi * MSH1$$
$$T2(\gamma\gamma) = \overline{S_1 + S_2} * \overline{MH\theta} * \overline{MH\varphi} * MSH2 * \overline{VC}$$

The matrices and the PLUs were programmed via a Super Caviar micro-processor. The trigger could be swiftly changed by reprogramming the processor using prepared diskettes.

The second level of the trigger made a decision within 200 ns according to the multiplicities of signals in the different hodoscopes and the veto counters. The multiplicities were found by adding the logic signals from all counters of interest (e.g. all Hθ elements in arm 1), and a decision was taken according to wether the signal was below a certain level or not. For the two examples above, the following requirements on the multiplicities were made in order to produce a trigger at the second level: (VN1 are the neutral vetoes in the forward direction, VN2 are the rest of the neutral vetoes)

Multiplicity	H1θ	H2θ	Hφ	SH1	SH2	VC	VN1	VN2
TT1 =	≤2	≤2	≤ 3	>0	>0	>0	>0	>0
TT2 =	0	0	0	>0	>0	0	0	0

Finally, at the third level, the energy information was taken into account. This was done in a CAB (CAmac Booster) processor which read the ADCs of the calorimeters and estimated crudely the energy in each arm. If the total energy was above a certain level, the trigger was accepted, and data were transferred to tape. The time needed for the third level of the trigger to make a decision was about 450 μs.

In addition, we made use of another processor, the MICE, which would use the MWPC and the CAB information to reconstruct the e^+e^- invariant mass within a time of 2.2 ms. This was not implemented in the trigger, but solely used for monitoring the experiment.

The data aquisition system was controlled by a ND10 computer which was used for several purposes. First of all, once we had a trigger, all Camac units should be read, the data should be transferred to tape and all registers should be reset before accepting another trigger. In addition, information on the antiproton beam momentum and momentum spread was transferred from the ISR control room via the ND10 and written to tape. Finally, sampling programs were running, providing information on the status of the detectors etc.

2.7 Use of Luminosity in the Experiment R704.

R704 was ready for data taking in the beginning of 1983. We had three periods of data-taking with antiproton-proton collisions. The two first periods were mainly devoted to testing our capability of extracting the expected signals. During the first period, from May 11. to May 15. 1983, we found several exclusive e^+e^- events at the ψ mass, giving confidence in the method. During the second period, in July and August 1983, our ability to find inclusive ψ events was demonstrated by the presence of four events compatible with the cascade decay $\chi_2 \rightarrow \gamma\psi \rightarrow \gamma e^+e^-$. Our ability to find $\eta_c \rightarrow \gamma\gamma$ events was however not demonstrated at this stage, but the offline analysis suggested a low background level. Finally, we had nearly three months of data-taking from March to June 1984. During this period, measurements and searches were done on four charmonium states, the η_c, the χ_1, the χ_2, and the $^1P_1$ state. Table 2.2 gives more details on the data-taking periods.

In total, R704 recorded an integrated luminosity of 3628 nb^{-1} by the expenditure of 9.7×10^{11} antiprotons. The maximum luminosity obtained was 2.7×10^{30} $cm^{-2}s^{-1}$.

Period	Current in ISR (at injection) (mA)	Integrated luminosity (nb^{-1})	Particle studied
11.5.83-15.5.83	0.35	9	J/ψ
19.7.83-22.7.83	0.47	8	J/ψ
		12	χ_2
25.7.83-29.7.83	1.82	18	J/ψ
		100	χ_2
1.8.83-5.8.83	1.04	38	η_c
		22	J/ψ
8.8.83-9.8.83	3.00	45	η_c
21.3.84-24.3.84	1.66	52	η_c
		63	J/ψ
26.3.84-30.3.84	1.29	105	η_c
4.4.84-7.4.84	5.20	20	J/ψ
		221	χ_2
13.4.84-19.4.84	4.83	542	χ_2
3.5.84-5.5.84	3.57	142	η_c
10.5.84-14.5.84	3.57	189	η_c
16.5.84-18.5.84	4.23	169	η_c
22.5.84-27.5.84	5.25	494	χ_1
29.5.84-2.6.84	5.27	500	$^1P_1$
6.6.84-7.6.84	4.78	200	$^1P_1$
19.6.84-25.6.84	2.31	319	$^1P_1$

Table 2.2: Overview of the different data-taking periods of R704.

3. *INCLUSIVE ψ ANALYSIS*

In this chapter we describe an analysis chain to find events of the type:

$$\bar{p}\,p \rightarrow \psi + X$$
$$\quad\;\; \hookrightarrow e^+e^-$$

where the electron-positron pair is found in the main detector arm.

The whole sample of 1.8×10^6 inclusive ψ triggers was analysed in search of events compatible with the $^1P_1$ charmonium state decaying into a ψ and one or several extra particles (denoted by X). The triggers at the χ_1 and χ_2 energies were analysed in order to check the consistency of the analysis, and also to study the background. The efficiency of the analysis was found by comparing the results to results stemming from dedicated studies of the reactions $\bar{p}p\rightarrow\chi_{1,2}\rightarrow e^+e^-\gamma$ and the reaction $\bar{p}p\rightarrow\psi\rightarrow e^+e^-$ [48,49,50].

3.1 Data Reduction.

The main signature of a ψ decaying into an electron-positron pair is the large energy deposition in the calorimeters, giving an invariant mass of the e^+e^- pair compatible with the ψ mass. Even at the trigger level, events were rejected unless a minimum energy deposit was present. The cut in energy was rather loose, and the primary aim of this cut was to reject minimum ionising particles (mips).

The first stage of the offline analysis consisted of cutting more severely in energy. This energy filter required that more than 75% of the total laboratory energy should be deposited in the calorimeters. This requirement reduced the amount of data to 555727 triggers, about 30% of the original sample. This stage of the analysis was done immediately after aquisition of the data, and provided various checks of the experimental apparatus as well.

The second stage of the analysis aimed at reducing the amount of data by a factor of about 10^2 with no loss of good events. A rather complete analysis of each event was required. The basic philosophy was to reconstruct tracks in the MWPCs and the analog chambers, associate these tracks with clusters of energy deposition in the precalorimeters (the PCs) and the lead glass walls (the LGs), and calculate the invariant mass of any pair of lines. The key cut parameter was the invariant mass, which should be compatible with the ψ mass. All events were passed through two chains of analysis, one based on lines found in the MWPCs, the other one was based on lines found in the analog chambers, where a line is defined by extrapolating a set of correlated peaks back to the centre of the interaction region. Events accepted by any one of the two analysis chains were retained for further analysis.

The structure of this part of the analysis is summarized as follows:

1. All lines which could be formed from the cluster pattern in the MWPCs and the analog chambers were found.

2. Every line was projected onto the precalorimeter and the lead glass, and the distance of this line to all clusters found in the calorimeter was calculated.

3. If the distances between the line and the clusters in the precalorimeter and the lead glass were smaller than some predefined cut values, the cluster energies should be associated to this line. Every energy cluster is tried against every line, so a line may, after this part of the analysis, have several energy assignments.

4. The invariant mass of every pair of lines (one line in each arm) was computed, and the event was accepted for further analysis if an invariant mass larger than some cut was found.

The cuts used in this production part of the analysis were loose, but provided a good rejection factor. Cut values for cluster assignments were at 10 cm for PC clusters and 15 cm for LG clusters. Only events containing a mass which was greater than 2.4 GeV/c^2 were accepted for further analysis. An additional cut on the MWPC cluster pattern had to be introduced in order to save CPU time. Triggers with two clusters or more in at least two of the three planes of at least one of the two small MWPCs were rejected from the MWPC analysis. This cut was motivated by the fact that we were primarily looking for events with just one particle in each detector arm, hence a clean event should contain just one cluster in each plane. The good events lost due to this cut, about 10%, were recovered in the alternative analysis. Only 6033 (1.1%) of the 555727 events subjected to this analysis survived these cuts. Table 3.1 gives some details of this part of the analysis.

The number of events decreases rapidly with increasing mass. This is illustrated in fig. 3.1, where the mass distribution of a subsample of the events passing the MWPC analysis is shown.

Sample	Triggers to be analyzed	Triggers left (analog part)	Triggers left (digital part)	Triggers left (total)
χ_1	165281	1478 (0.9%)	374 (0.2%)	1598 (1.0%)
χ_2	121749	1385 (1.2%)	385 (0.3%)	1513 (1.3%)
$^1P_1$	268697	2685 (1.0%)	613 (0.2%)	2922 (1.1%)
Total	555727	5548 (1.0%)	1372 (0.2%)	6033 (1.1%)

Table 3.1 : Production statistics.

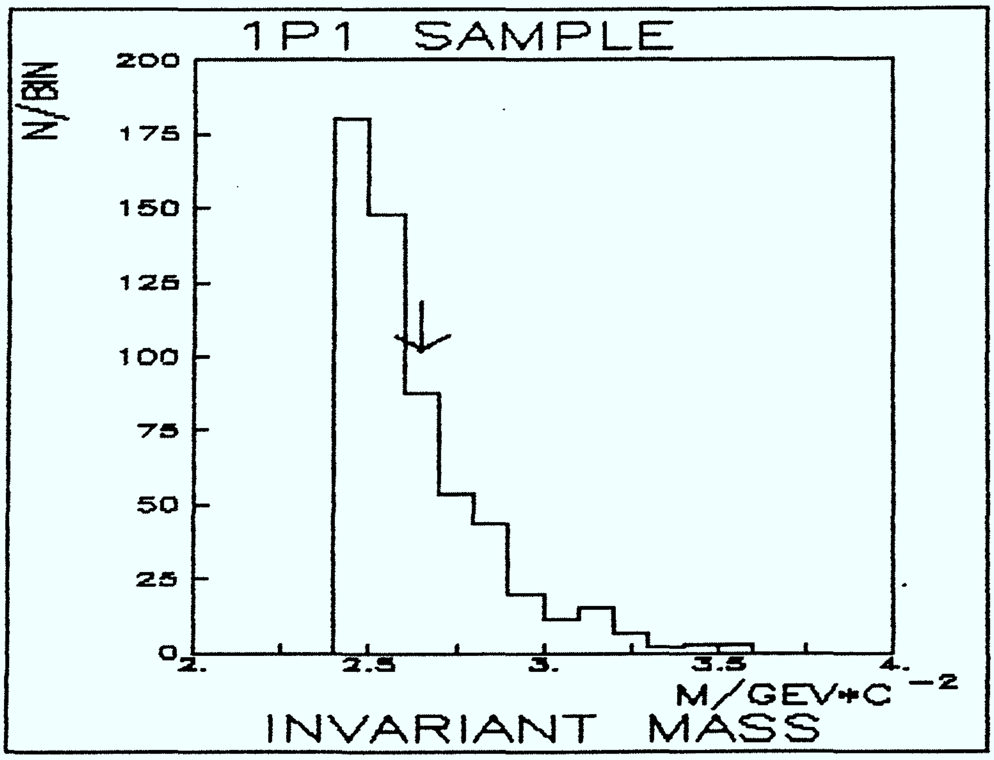

Fig. 3.1: Invariant mass distribution of e^+e^- pairs passing the MWPC analysis. The arrow indicates the value of the eventual cut in mass (2.65 GeV/c^2).

3.2 Final Analysis.

3.2.1 The ψ as an Analyser.

Throughout the data taking, considerable time was spent on collecting exclusive ψ candidates, i.e. adjusting the beam momentum so as to allow for resonant formation of the ψ. The signature of a ψ, in the reaction $\bar{p}p \to \psi \to e^+e^-$, is very clear, since in addition to mass and topological requirements, the simple two-body kinematics is very constraining on possible ψ candidates. A sample of 187 ψ candidates, essentally background free, has been extracted from the data [48]. The properties of this sample of events were studied in order to tune the cuts to be used in the search for inclusive ψ candidates.

We are searching events which contain one electron (or positron) in each detector arm. Such events would be characterized by a number of properties. We should have signals in the scintillators S_1 and S_2 which are compatible with the response of minimum ionizing particles. In the Cerenkov counters we should also have signals which do not deviate too much from the average response of an electron (about 5.5 photoelectrons). This average is determined from separate tests as well as from the ψ sample. A high signal could for instance be caused by an early γ conversion. Furthermore, the lines found in the MWPCs should be compatible with the clusters found in the calorimeters. Finally an electromagnetic shower should be found in each calorimeter. An electromagnetic shower is characterized by a large energy deposition in the PC, while hadronic showers may be initiated in the LG. The transverse properties of the showers in the PC and the analog chambers were studied in order to reject events which have two close showers. In figs. 3.2-3.9 we show plots of properties of the ψ events which are exploited in the following analysis.

3.2.2 The Final Event Selection.

The final cuts were applied in two steps. In the first step, we retained events even though no charged track was found in the MWPCs. In the second step, a good MWPC line was required in each arm. This proved very effective in reducing the background, at the expense of a loss of about 8% of the events due to MWPC inefficiencies.

We applied the following cuts on the sample of 6033 triggers left in the analysis chain:(The unit mip is the average signal of a minimum ionizing particle passing through a detector).

1. Mass cut at 2.65 GeV/c^2 (fig. 3.2)

2. Tightening of requirements for cluster association:
   3.2 cm in the PC and 8.6 cm in the LG for association of clusters to lines found in the MWPCs (fig. 3.3).
   4.2 cm in the PC and 8.6 cm in the LG for association of lines found in the analog chambers.

3. Scintillator and Cerenkov response should be consistent with an electron. A good rejection factor without losses of too many good events was obtained by rejecting events where both the S and C response were "abnormal". An event was rejected if: S_1 > 2.2 mip and C_1 > 8.7 photoelectrons (p.e) (fig. 3.4), <u>or</u> S_2 > 1.9 mip and C_2 > 10.0 p.e (fig. 3.5), <u>or</u> S_1+S_2 > 4.4 mip.

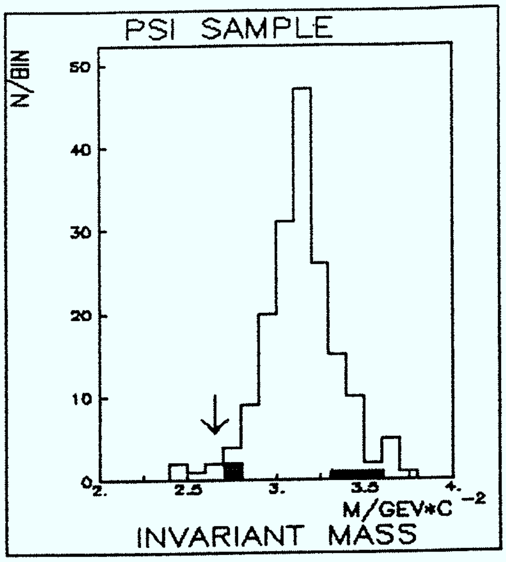

Fig. 3.2

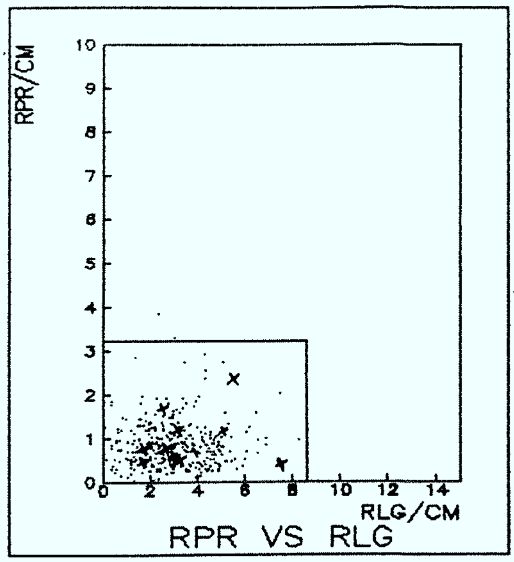

Fig. 3.3

Fig. 3.2: Invariant mass distribution of exclusive ψ events. The masses of the 5 $^1P_1$ candidates are indicated in black.

Fig. 3.3: Distance of precalorimeter cluster to the MWPC line vs the distance of the lead glass cluster to the MWPC line for ψ (dots) and $^1P_1$ events (crosses).

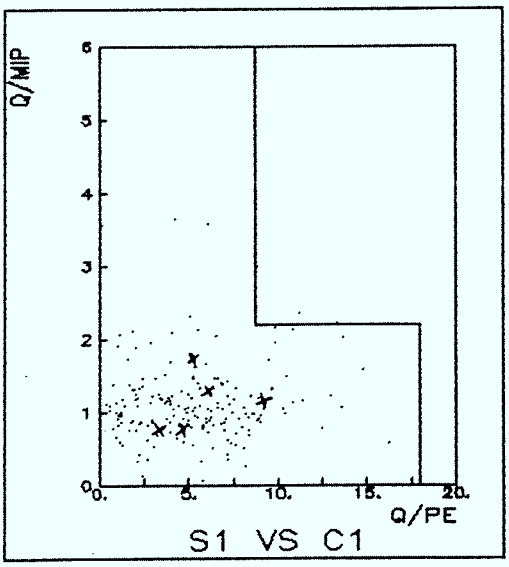

Fig. 3.4

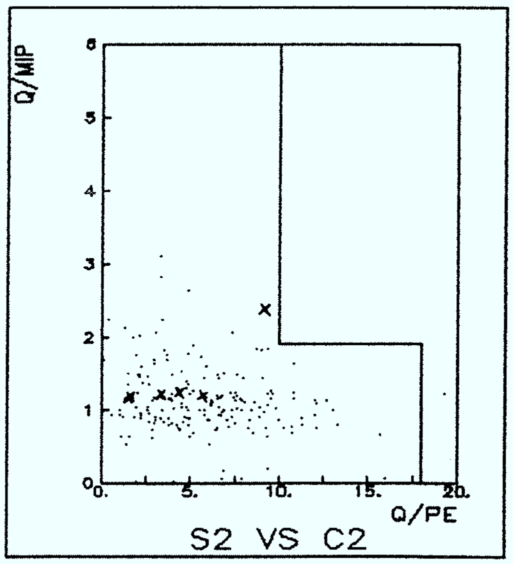

Fig. 3.5

Fig. 3.4: Response of the small scintillation counter in arm 1 vs. response of the Cerenkov counter in arm 1 for ψ events (dots) and $^1P_1$ candidates (crosses). The allowed region of response is also indicated.

Fig. 3.5: As fig. 3.4 for the counters in arm 2.

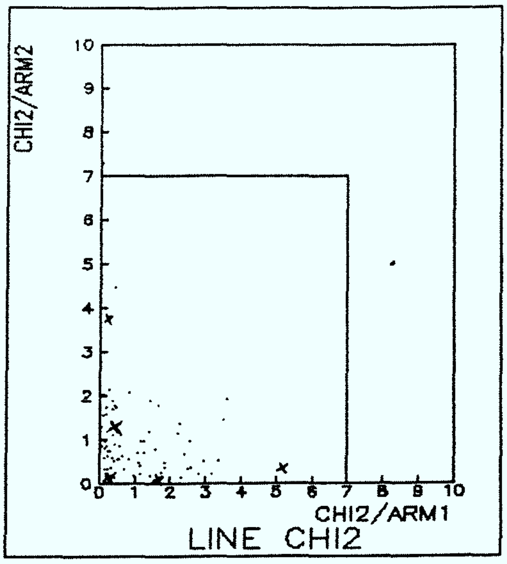

Fig. 3.6

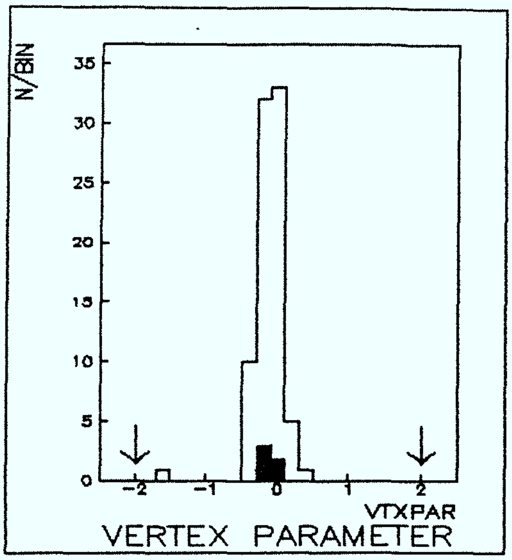

Fig. 3.7

Fig. 3.6: χ^2 of fitted line in arm 2 vs. χ^2 of fitted line in arm 1 for ψ events (dots) and for the 5 $^1P_1$ candidates (crosses). Only ψ events with one fitted line per arm are shown.

Fig. 3.7: Vertex parameter for ψ events with 1 line per arm. In black the distribution of this parameter for the $^1P_1$ candidates.

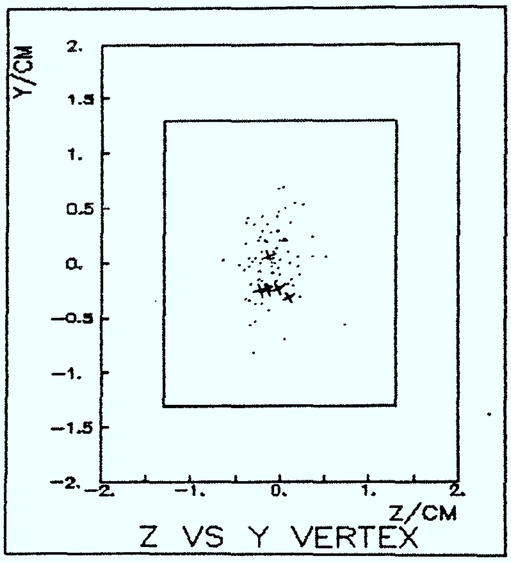

Fig. 3.8

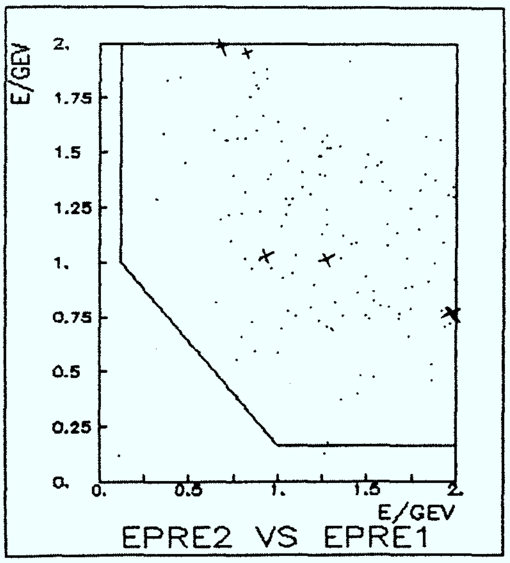

Fig. 3.9

Fig. 3.8: z- coordinate vs. y-coordinate of the vertex for the ψ events with one line in each arm (dots) and for the $^1P_1$ candidates (crosses).

Fig. 3.9: Associated cluster energy in the precalorimeter of arm 1 vs. associated cluster energy in the precalorimeter of arm 2 for ψ events (dots) and $^1P_1$ candidates (crosses).

These cuts reduced the data sample to 590 events. Most of these did not pass the MWPC analysis, and contained probably neutral energetic photons in the detector (e.g. from π^0 decays).

Now we impose the requirements of the existence of MWPC lines with a certain quality. A fitted line should have a $\chi^2 < 7$ (fig. 3.6), the vertex parameter should be less than 2.0 cm for a pair of lines used in the analysis (fig. 3.7) and the actual vertex should be reconstructed to lie in the p $\bar{p}$ interaction region; y and z coordinates should lie between -1.3 cm and 1.3 cm (fig. 3.8) (The coordinate systems are defined in appendix 1). No constraint is imposed on the x coordinate, because the radial position of the antiproton beam could change by nearly 10 cm in the ISR. These requirements reduced the data sample to 203 events, 61 from the χ_1 scan, 81 from the χ_2 scan and 62 from the $^1P_1$ scan. The invariant mass distributions of these samples are shown on figs. 3.10a, 3.11a and 3.12a.

To further reduce the sample, the mass cut was imposed by considering only the calculations using the MWPC lines. The response of the calorimeters was studied more closely in order to reject events with hadronic showers and events containing several close showers. Hadronic showers are recognized by a low energy depostion in the precalorimeter. Furthermore, a cut on the Cerenkov response was imposed before all events were scanned visually. The final selection required events to fulfill the following criteria:

1. Mass (of charged pair of tracks) > 2.65 GeV/c^2.

2. Electronlike response in the PC; cluster energies should be larger than 120 MeV in arm 1, and larger than 160 MeV in arm 2. The sum of the two PC cluster energies should be

larger than 1.0 GeV (fig. 3.9).

3. The PC response was analysed more closely. Within a window of a total of 9 counter elements around the projected MWPC line, double peak structures were sought. If a valley was found in the response within this window which was deeper than .7 mip, the event was rejected.

4. C_1 and C_2 responses should be less than 18 photoelectrons. (figs. 3.4-3.5)

5. Finally, the events were scanned visually. A few events were rejected at this stage. Two reasons for rejection dominated; either double peaks were found in the analog chambers (often a shallow valley would also be present in the PC), or a large number of extra clusters were found in the detectors and the veto counters,excluding any interpretation as a charmonium state decaying to the ψ.

In the table below, we show the effect of the last 5 cuts on the three inclusive ψ samples and on the exclusive ψ sample.

Cut	ψ			χ_1			χ_2			$^1P_1$		
	in	rej.	out	in	rej.	out	in	rej.	out	in	rej.	out
1	164	3	161	61	8	53	81	4	77	62	14	48
2	161	1	160	53	11	42	77	6	71	48	16	32
3	160	11	149	42	11	31	71	16	55	32	24	8
4	149	1	148	31	1	30	55	2	53	8	3	5
5	not scanned			30	3	27	53	7	46	5	0	5

Table 3.2: The effect of the last cuts.

We are now left with an event sample of 27 inclusive ψ candidates at the χ_1 energy, 46 at the χ_2 energy and 5 from the search for the $^1P_1$ charmonium state. Their invariant mass distributions are shown in figs. 3.10b, 3.11b and 3.12b, where the the events rejected in the visual scan are included (in black).

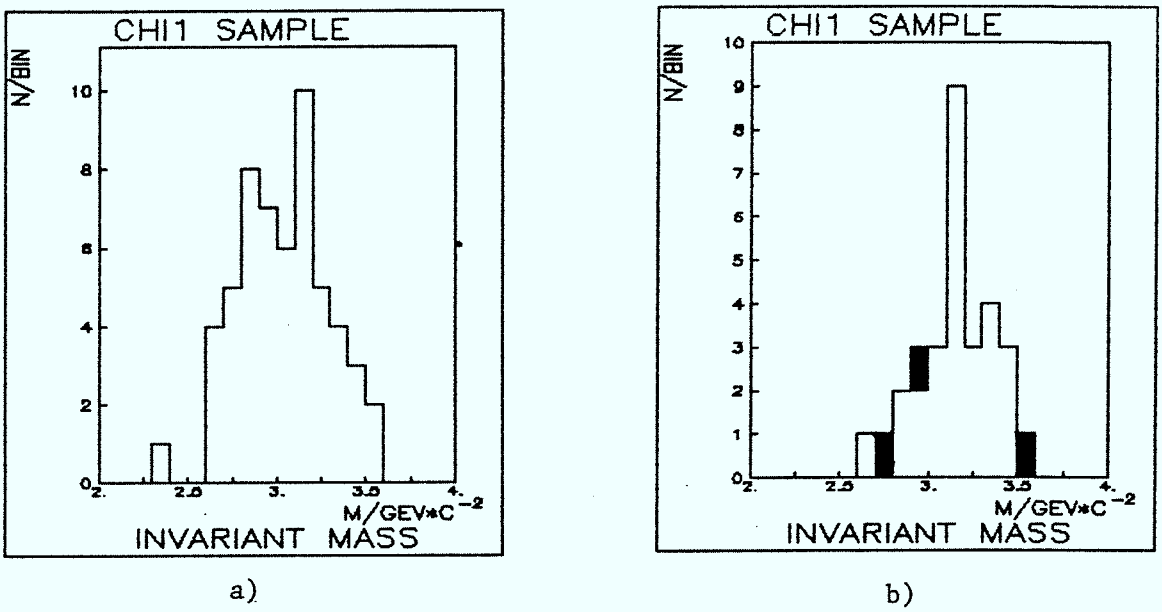

Fig.3.10: Invariant mass distribution of χ_1 sample before the final cuts (a). (b) shows the invariant mass distribution of the events before they were scanned visually. The events rejected during the scan are shown in black.

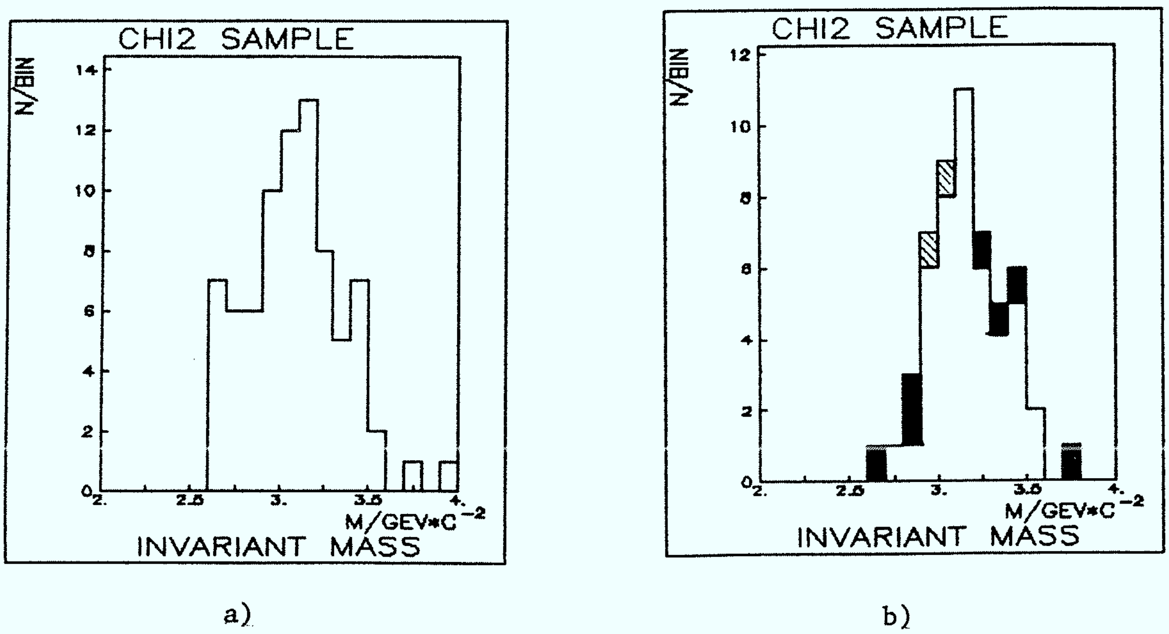

Fig.3.11: As fig. 3.10 for the χ_2 sample. The two shaded events are those which are incompatible with a $\psi\gamma$ final state.

a)

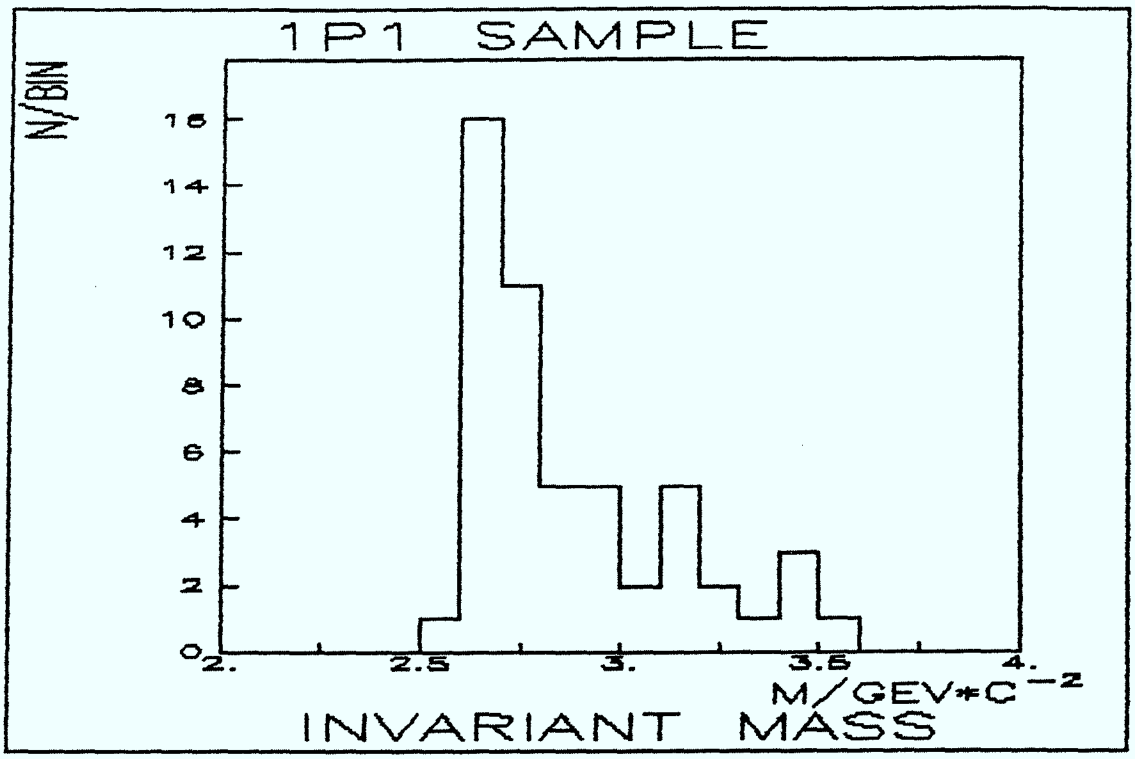

b)

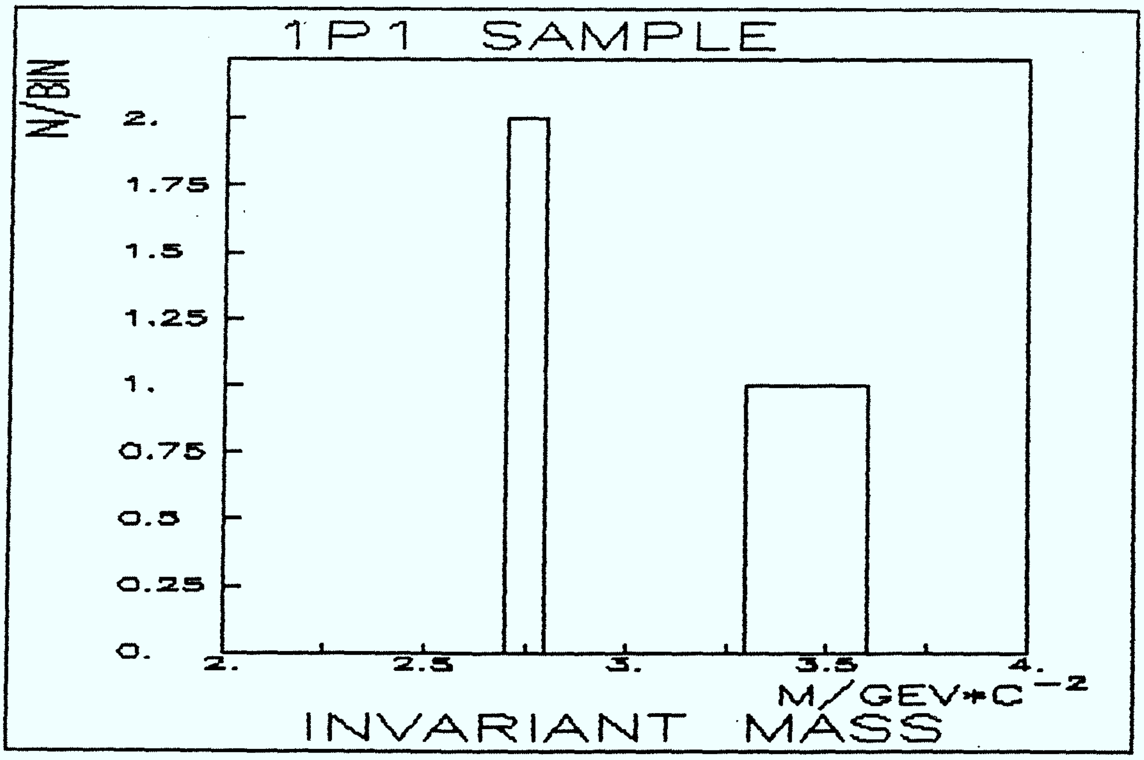

Fig.3.12: As figs. 3.10 and 3.11 for the $^1P_1$ candidates. No events were rejected during the visual scan.

3.2.3 Comments on the Event Samples.

A few properties of the five ${}^1P_1$ candidates are found in table 3.3. These properties are also histogrammed in figs. 3.2-3.9. From these plots we see that the values of the cut parameters seem, in many cases, to be excessively loose. This is to remain as efficient as possible. It should be noted that all the ${}^1P_1$ candidates have properties which in general seem to be well within the cuts. A possible exception to this is the event no. 10155 of run 1248, which is close to the values of the cut parameters in three cases (combined S-C cut, distance track-cluster cut and χ^2 of line cut).

Event	Run	Trigger	Mass (GeV/c^2)	Dist. to cluster (cm) PC1	LG1	PC2	LG2	PC Energy (GeV) PC1	PC2
1	1178	5688	2.70	1.2	5.0	0.7	2.6	2.8	0.8
2	1179	4718	3.44	0.8	2.0	1.7	2.8	0.9	1.9
3	1200	708	3.50	0.5	1.8	0.4	3.4	1.3	1.0
4	1230	1720	3.36	1.2	3.2	0.5	3.0	1.0	1.1
5	1248	10155	2.74	2.3	5.9	0.4	7.6	0.8	2.5

Event	S_1 (mips)	S_2	C_1 (p.e.)	C_2	Vert. par. (cm)	Vert.pos.(cm) y	z	Line χ^2 arm1	arm2
1	0.7	1.2	3.6	1.7	-0.11	-0.1	0.1	0.1	3.9
2	1.2	1.3	6.9	3.7	-0.09	0.2	0.4	1.7	0.1
3	1.7	1.2	5.3	5.9	-0.18	0.0	-0.3	0.3	1.4
4	0.7	1.3	4.7	4.3	-0.05	-0.1	-0.3	0.1	0.2
5	1.1	2.3	6.0	9.1	-0.27	-0.2	-0.3	5.1	0.3

Table 3.3: Properties of selected ${}^1P_1$ candidates.

Unfortunately, we were not able to determine exactly the final state of the five $^1P_1$ candidates, due to the low acceptance and the rough segmentation of the veto counters. However, two of the events seem to contain extra charged particles in the final state, the other three seem to contain neutral particles in the final state. Two of the events are compatible with both a $\psi\gamma$ final state, and a final state containing a ψ plus one or several π^0s.

Two inclusive ψ candidates from the χ_2 sample are incompatible with a $\psi\gamma$ hypothesis. The rest of the events of the χ_1 and χ_2 samples are compatible with a $\psi\gamma$ final sate. Most of these events are also accepted as $\psi\gamma$ events in the dedicated χ studies [49,50,51]. Since the cuts are different in the different analysis chains, the event samples do not overlap completely.

3.2.4 Efficiency of the analysis.

The ψ control sample is used to find the efficiency of the analysis. Out of the 187 ψ events, 148 survived the cuts we applied. This should give an efficiency of the analysis chain of 79 $\pm$ 6 %. This includes track reconstruction efficiencies and cut efficiencies. The main trigger inefficiency is due to the Cerenkov counters. In order to determine the detection efficiency for the processes $p\bar{p} \to \chi_J \to \psi\gamma \to e^+e^-\gamma$, a Monte Carlo simulation was performed. This simulation took into account the geometrical acceptance and the Cerenkov efficiency as parametrised in ref. [52].(See also sect. 4.4.) For the χ_1 we found a detection efficiency of 8.0%. Since we do not know exactly the final state of our five $^1P_1$ candidates, we take the χ_1 figure as the detection efficiency for these events as well. The uncertainties in estimates based on these events will in any case be dominated by the statistical uncertainty due to the small number of events. Hence we estimate the total detection efficiency to be 6.3 $\pm$ .6 %.

3.3 Interpretation of the events.

3.3.1 The χ Samples.

All events, except for two at the χ_2 mass, may be interpreted as $\psi\gamma$ events. The two non-$\psi\gamma$ events could be hadronic transitions from the χ_2 to a ψ. The fact that they are produced at an energy which coincides with the peak of the χ_2 exitation curve, supports this hypothesis. With the remaining events, a total of 71, two exitation curves (fig. 3.13) may be formed. The background level which is indicated in the figure is an upper limit based on data taken off resonance during the $^1P_1$ scan (a total of 309 nb^{-1} yields a background level which is given by σ_B^{eff} < 7.4pb). We refer to [51] for results on the χ_1 and χ_2 masses and widths extracted from R704 data. The point here is to show that we have been able to extract a sample of events which does not seem to be contaminated due to some background. In fact, out of the 71 events, 63 are also found in the sample of 80 events qouted in [51]. This is in reasonable agreement with expectation, bearing in mind that the latter sample is selected with an efficiency of 93%. (With two independent event selection chains with efficiencies of 79% and 93% respectively, the probability for an event to be found by the first one and missed by the second one is .79x(1-.93) = 5.5%.)

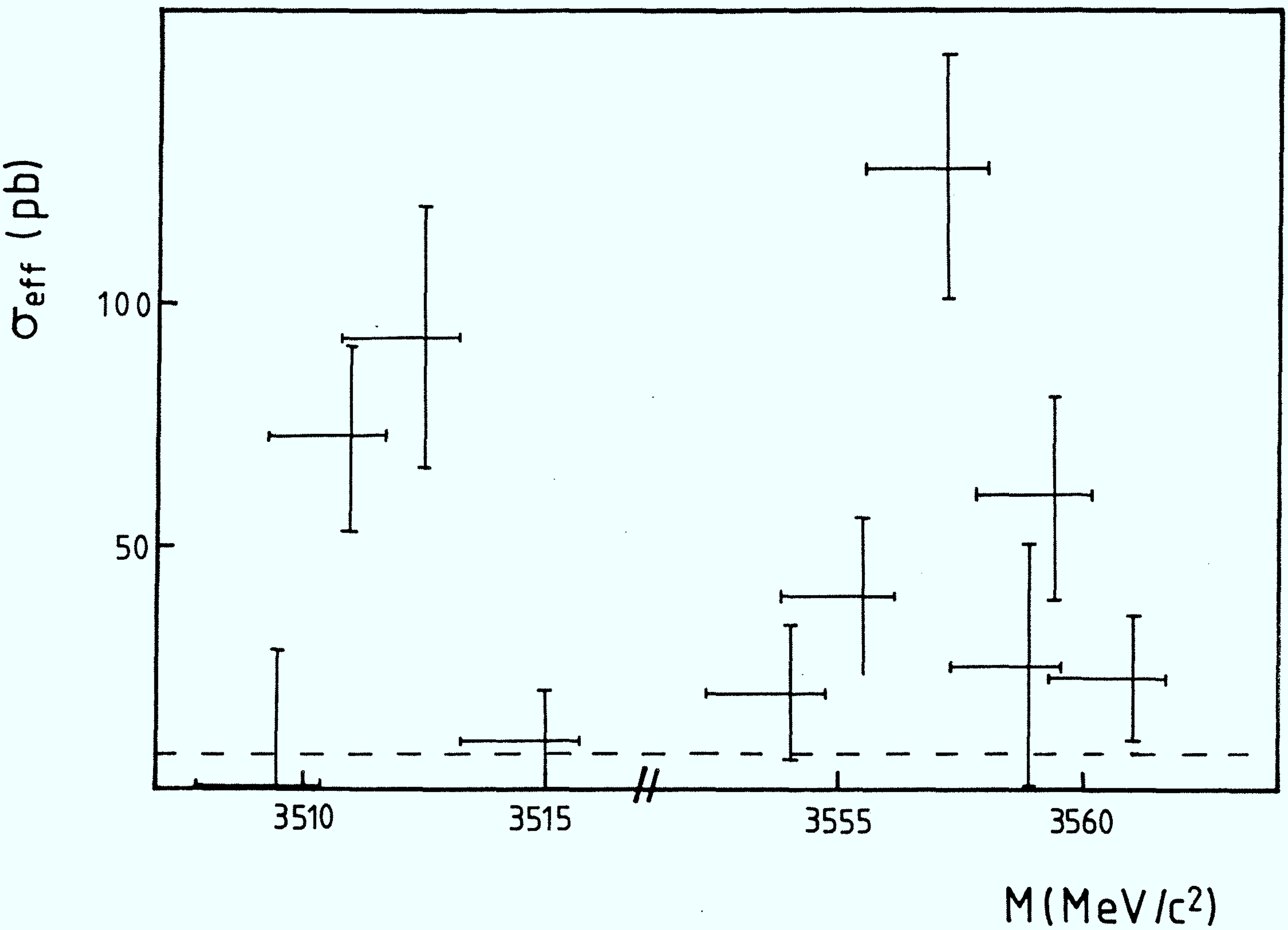

Fig.3.13: Exitation curves formed by the χ_1 and the χ_2 events. The dotted line is the 90% c.l. upper limit of the background which is found from the off resonance data (zero events in 309 nb^{-1}).

3.3.2 The $^1P_1$ Sample

The search for the $^1P_1$ state was performed in eight energy bins. Table 3.4 shows the number of events, the integrated luminosity and the CM energy of each bin. The beam profile could be approximated by two half gaussians with widths $\sigma_- = 1.6$ MeV and $\sigma_+ = .7$ MeV. The data are consistent with the hypothesis that all the events are due to the decay of a resonance with a mass of about 3525 MeV/c^2 A maximum likelihood fit of the data to a Breit Wigner distribution yields a mass of 3525.4$\pm$.8$\pm$.4 MeV/c^2 [53].

M (MeV/c^2)	L (nb^{-1})	Events
3520	62	0
3521.1	54	0
3523.3	49	0
3525	253	1
3525.5	93	1
3526.4	364	3
3528	47	0
3530	97	0
total	1019	5

Table 3.4: Integrated luminosity and number of events in each mass bin of the $^1P_1$ search.

We now proceed to discuss the significance of this result by considering the possibility that the observed events may stem from a background which is flat over the energy range of the scan. Two sources of background are possible; firstly the inclusive ψ candidates could be simulated by some other reaction, the second possibility is that the events are real inclusive ψs, but that they are produced non-resonantly.

The number of background events decreases rapidly with increasing invariant mass (see fig. 3.1). The final topological cuts on the event sample cause a removal of the pile-up of events towards low mass. If a non-ψ background is present in the final event sample, one should expect a pile-up towards low mass in the final mass distribution as well. We see from fig. 3.12b that such a pile-up is not present for the $^1P_1$ event candidates. The mean value of this distribution is in fact 3.15 GeV/c^2. Some worry might however be caused by the fact that the invariant masses of the five events are at the tails of the resonant ψ mass distribution.

The most serious non-resonant process contributing to inclusive ψ production is the reaction $p\bar{p}\to\psi\pi^0$. The cross section for this process has been calculated to be approximately 220 pb. [54]. If this estimate is correct, we expect that 1 event of this kind should be detected during the $^1P_1$ scan, taking into account the $\psi\to e^+e^-$ branching ratio and the detection efficiency. We may thus not neglect the possibility that some of the events are non-resonant $\psi\pi^0$ events. However, two of our candidates are incompatible with a $\psi\pi^0$ hypothesis.

Regardless of the origin of the events, we must test the possibility that they are pure background events. The test we choose is the one sided Kolmogorov-Smirnov test, described in e.g. ref. [55]. This test may be applied to samples of all sizes, as opposed to other tests which often are valid only for fairly large data samples.

The Kolmogorov-Smirnov test consists, in our case, of computing the accumulated number of events as a function of integrated luminosity, and comparing the cumulative distribution thus obtained with what is expected for the hypothesis which is tested. Specifically, assuming that event number i is observed after having collected an integrated luminosity of l_i , the distribution:

$$F_N(l) = \begin{cases} 0 & \text{for } l < l_i \\ i/N & \text{for } l_i < l < l_{i+1} \\ 1 & \text{for } l > l_N \end{cases}$$

where N is the total number of events, is compared to the expected cumulative distribution, denoted by F(l) (properly normalised). If the hypothesis we want to test is true, the expected distribution should not deviate too much from the observed one. Conversely, a large deviation from F(l) should indicate that we may reject the hypothesis.

We order our data in the following way: First we accumulate luminosity in the "off" region of 309 nb^{-1}, then we accumulate statistics on the "on" region (710 nb^{-1}). We assume that the events found in the "on" region are found at regular intervals. Now, assuming the background hypothesis, F(l) should rise linearily with l.

Quantitatively, we define the quantity:

$$D^- = \max\{F(l)-F_N(l)\} ;$$

D^- is a random variable which is distribution free, i.e. its distribution does not depend on the shape of F(l). Hence, a universal expression for the distribution of D^- exist, and on basis of this one may compute confidence levels*. The confidence level, denoted by α, is the probability that D^- will be larger than the observed value (D^-_{obs}) if the experiment were repeated and the background hypothesis were true. If the tested hypothesis should be rejected, a confidence level which is smaller than 5% is required. Very often, even a 1% criterion is employed.

* In this context, the term "confidence level" is frequently called the "significance level".

From fig. 3.14, we see that we observe a value D^{-}_{obs} of .373 . For a total of five events (N=5), this corresponds to a confidence level of 18.5% [80]. We could improve the significance of our experiment by including edges of the χ_1 scan, as "off" region for the $^1P_1$ scan.The χ_1 is close to the $^1P_1$ implying that the background should be similar. We cannot assume that all events seen in the χ_1 scans originate from χ_1 decays. However, we may look for background events in regions where the χ_1 resonant cross-section is neglible compared to the background level. The worst possible case is to consider all events of the $^1P_1$ scan as background events. The χ_1 resonant cross-section will be said to be neglible when it is smaller than the 84% c.l. upper limit to the background level thus obtained. Furthermore, the 84% c.l. result to the χ_1 width,Γ < .3 MeV, is used in calculating the χ_1 cross section. In this way, one is able to include another 71 nb^{-1} of background luminosity [56]. No events are found here. The confidence level of our test is in this way reduced to 13.3%. We are thus still not able to reject the background hypothesis. Finally, we note that in order to come down to a confidence level of 5 %, a total of 594 nb^{-1} should have been accumulated off resonance without finding events. The assumption that all the events found under the χ_1 are genuine χ_1 decays (they are all compatible with a $\psi\gamma$ hypothesis), will add 494 nb^{-1} to the "off" region. Under this assumption we could reject the background hypothesis if our criterion for rejection is that the confidence level should be less than 5%.

The conclusion after all this is that we may not reject the hypothesis that the events we have seen during the $^1P_1$ scan are background events unless we assume that all the events seen during the χ_1 scan are genuine χ_1 decays.

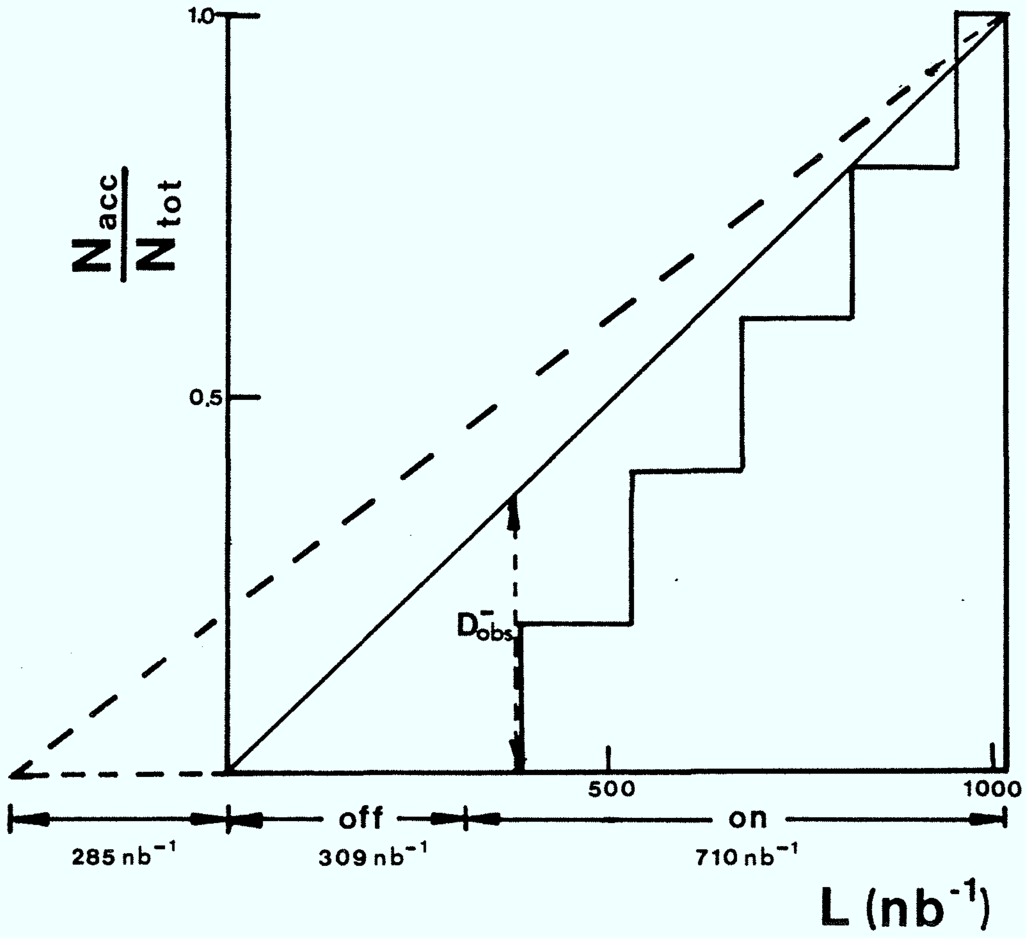

Fig.3.14: Illustration of the Kolmogorov-Smirnov test. Cumulative distribution of events. The experimental data are compared to the expected rate of accumulation for a pure background hypothesis (solid line). D^-_{obs} is the maximal deviation of the experimental distribution from the theoretical background distribution. Dotted lines shows the situation necessary for a 5% confidence level rejection.

3.3.3 The Resonance Hypothesis.

In the limit of vanishing spin-spin forces, the $^1P_1$ is expected to have a mass equal to the spin weighted average of the three ^3P_J states. In order to avoid systematic errors , we use the R704 values of the χ_1 and the χ_2 masses ($3511.3\pm0.4\pm0.4$ MeV/c^2 and $3556.9\pm0.4\pm0.5$ MeV/c^2 respectively) and shift the table value of the χ_0 mass upwards by one MeV to 3416.0 ± 1.0 MeV/c^2, when estimating the c.o.g mass. The reason for shifting the table value of the χ_0 mass by 1 MeV/c^2 is that the R704 results on the χ_1 and the χ_2 masses both are shifted upwards by 1 MeV/c^2 with respect to the previous world average. This results in a mass:

$$M_{cog} = 3526.0 \pm 0.5 \text{ MeV}/c^2$$

to be compared to the result quoted above ($M_{^1P_1}$ = 3525.4 ± 0.8 MeV/c^2) If we have seen the $^1P_1$ state , spin-spin forces are indeed of a short range nature. This is in fact in agreement with expectation of those potential models which assume "electric confinement", i.e. that the long range forces are purely scalar. This assumption also give fair predictions of the mass splittings of the triplet states [57,20].

Using the QCD sum-rule approach [15], the mass of the $^1P_1$ is predicted at (3.51 ± 0.01) GeV/c^2. This unambigous prediction is slightly below the mass of our $^1P_1$ candidate.

Finally we note that also Monte Carlo simulations within lattice QCD favour scalar confinement [23,24].

The observed mass splittings of the P states allow us to estimate the contributions of the spin-orbit, tensor and spin-spin terms to the splittings. The masses of the P states may be written:

$$M = M_0 + \Delta M = M_0 + a\langle\vec{L}.\vec{S}\rangle + b\langle S_{12}\rangle + c\langle\vec{s}_1.\vec{s}_2\rangle$$

where $\vec{s}_1$ and $\vec{s}_2$ are the spins of the two quarks, $\vec{S}=\vec{s}_1+\vec{s}_2$, $\vec{L}$ is the orbital angular momentum and $S_{12} = 3(\vec{\sigma}_1.\vec{r})(\vec{\sigma}_2.\vec{r})/r^2 - \vec{\sigma}_1.\vec{\sigma}_2$; $\vec{\sigma}=2\vec{s}$. $\vec{r}$ is a vector between the quarks. The expectation values are:

$$\langle\vec{L}.\vec{S}\rangle = \begin{pmatrix} 0 \\ -2 \\ -1 \\ 1 \end{pmatrix}, \quad \langle S_{12}\rangle = \begin{pmatrix} 0 \\ -4 \\ 2 \\ -2/5 \end{pmatrix}, \quad \langle\vec{s}_1.\vec{s}_2\rangle = \begin{pmatrix} -3/4 \\ 1/4 \\ 1/4 \\ 1/4 \end{pmatrix} \text{ for the } \begin{pmatrix} {}^1P_1 \\ {}^3P_0 \\ {}^3P_1 \\ {}^3P_2 \end{pmatrix}$$

Hence, we obtain :

$$\begin{aligned} M({}^1P_1) &= (M_0 + (1/4)c) - c \\ M({}^3P_0) &= (M_0 + (1/4)c) - 2a - 4b \\ M({}^3P_1) &= (M_0 + (1/4)c) - a + 2b \\ M({}^3P_2) &= (M_0 + (1/4)c) + a - (2/5)b \end{aligned}$$

where $M_0 + (1/4)c$ is the centre of gravity mass quoted above. Solving for a, b, and c and inserting the experimental masses, we obtain:

$$\begin{aligned} a &= 35.0 \pm 0.9 \text{ MeV}, \\ b &= 10.1 \pm 0.7 \text{ MeV}, \\ c &= 0.6 \pm 0.9 \text{ MeV}. \end{aligned}$$

This is illustrated in fig. 3.15.

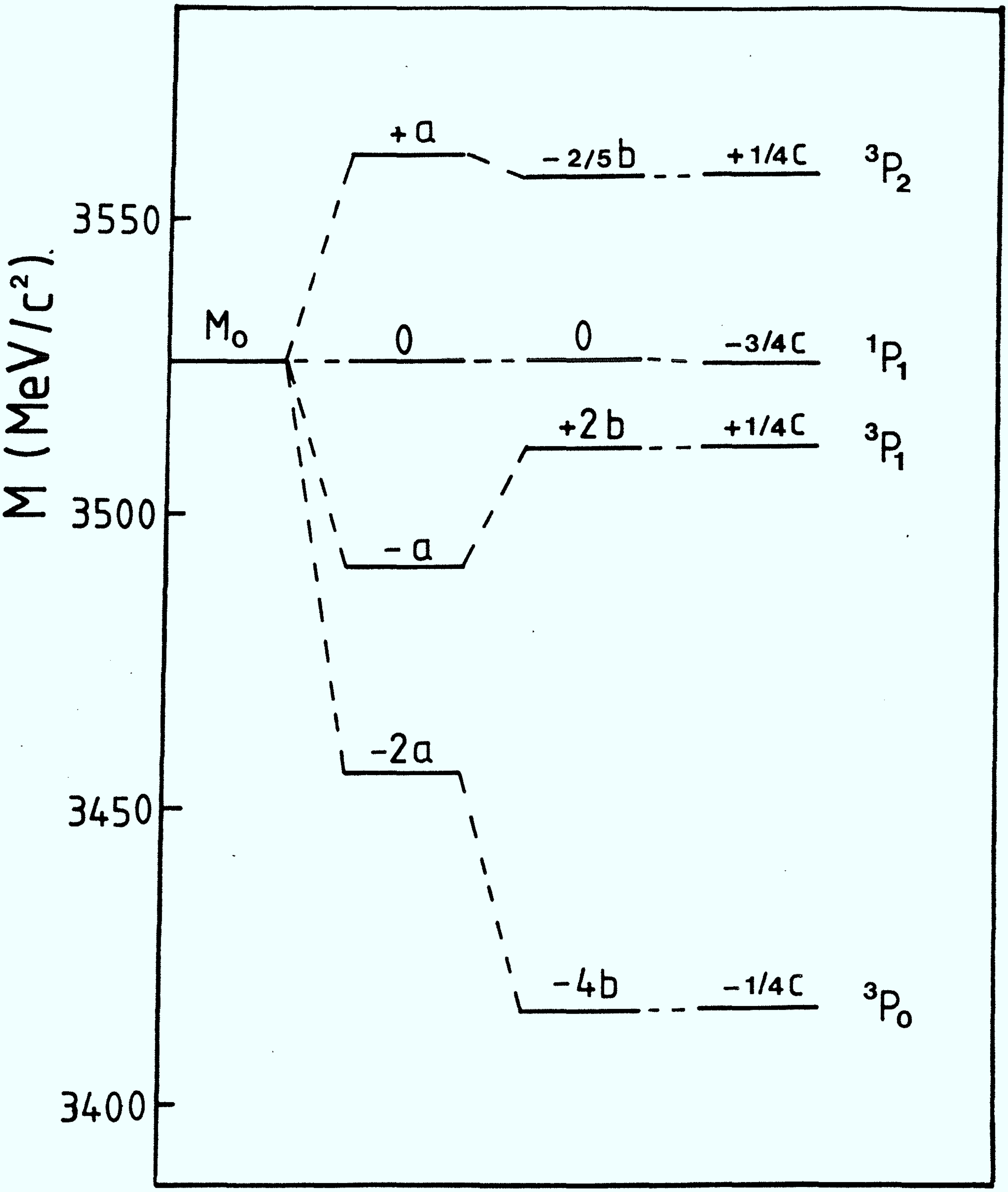

Fig.3.15: Contributions to the relative mass splittings of the four P states of charmonium, assuming that the $^1P_1$ state is 0.6 MeV/c^2 below the centre of gravity of the ^3P states. a, b and c are the spin-orbit, tensor and spin-spin contributions to the level splittings respectively.

It has been argued that the $^1P_1$ should not be formed in antiproton proton collisions at all, because such a process should be prohibited by the QCD helicity selection rule [58]. This rule is valid only in the limit of vanishing quark masses (of proton constituents). The ratio between the proton mass and its CM momentum is .6 for the process $\bar{p}p \to {}^1P_1$, so it does not seem reasonable to make this assumption at these energies. In fact, observation of the η_c decaying into a proton antiproton pair [59], rejects this hypothesis. Quantitatively we note that from studying the angular distribution of $e^+e^- \to \psi \to p\bar{p}$, it is expected that the net helicity zero contribution to the cross section should be about 1/4 of the net helicity one contribution (see sect 1.6).

The estimate of the cross-section for the process $\bar{p}p \to {}^1P_1 \to \psi + X$ must rely on a number of assumptions. We should however be able to estimate the correct order of magnitude. At the resonance peak, the Breit-Wigner cross-section is given by:

$$\sigma_p = 0.488\times10^7 \text{nb GeV}^2 \times (2J+1)B_iB_f/(m_r^2 - 4m_p^2)$$

where J is the spin of the resonance and B_i and B_f are the branching ratios to the initial and final states. m_r and m_p are the resonance and the proton masses respectively. Estimates of these branching ratios are now made by studying expected properties of the $^1P_1$ state when compared to the other charmonium states. In sect. 1.4.4 we saw that the hadronic width of the $^1P_1$ should be approximately equal to the width of the χ_1. Specifically, Novikov et.al. made the prediction [31]:

$$\frac{\Gamma(^3P_1 \to \text{hadrons})}{\Gamma(^1P_1 \to \text{hadrons})} = \frac{6}{5}$$

The best measurements on the χ_1 total width is the R704 result [51], $\Gamma(\chi_1 \rightarrow \text{all}) < 1.3$ MeV (95% c.l.). This measurement is however strongly correlated to the branching ratio to the $\bar{p}p$ initial state. Using the result $B(\chi_1 \rightarrow p\bar{p}) < 1.3\ 10^{-4}$ [8], a lower limit of 0.1 MeV is obtained. The experimental data are certainly still not very constraining. In 0 order QCD, the χ_1 hadronic width is estimated at around 0.2 MeV [32]. However it is known that 0 order QCD seems to consistently predict much too low widths. The χ_2 measurements are confirming this. On the other hand, the radiative transition rates of the χ_J states to the ψ seem to have been calculated more reliably[60]. Using this input, and the measured branching ratios of these transitions, one is able to predict hadronic widths which seem to be in reasonable agreement with experiment (i.e. in agreement with the R704 measurement of the χ_2 width). The χ_1 prediction becomes $\Gamma(\chi_1 \rightarrow \text{hadrons}) = 0.8$ MeV for a branching ratio of 28 % for the transition $\chi_1 \rightarrow \gamma\psi$. Thus, using the relation above, we arrive at an expected hadronic width of the $^1P_1$ of .65 MeV.

Two more processes are of importance when estimating the total width; the radiative (E1) transition to the η_c, and hadronic transitions to the ψ. In ref. [60], the rate of the $^1P_1$ radiative transition to the η_c is calculated to be 0.48 MeV. Finally, we note that the rate of hadronic transitions from the ψ' to the ψ are 0.11 MeV. Simply scaling with phase space (a fair assumption, since the $^1P_1$ has negative charge conjugation, just like the ψ and the ψ', and the possible transition channels are the same [61]), will give an expected rate of .08 MeV for $^1P_1$ hadronic transitions to the ψ. This estimate is based on the assumption that a P$\rightarrow$S transition has the same probability as a S$\rightarrow$S transition. Hence, we arrive at a total width of the $^1P_1$ of approximately 1.2 MeV, and a branching ratio to the ψ of 6.1%. Taking into account the ψ branching to an electron positron pair, we obtain:

$$B_f \approx 5 \times 10^{-3}$$

For a total width of the χ_1 of 1.1 MeV, we note that R704 predicts a branching ratio of the χ_1 to $p\bar{p}$ in the range $0.5\text{-}0.9 \times 10^{-4}$ [51]. Assuming that the $^1P_1$ branching ratio will be suppressed by a factor of 4, (see sect. 1.6), due to the helicity selection rule, but that the formation process is otherwise similar, gives an estimate of the branching ratio to the initial state of:

$$B_i \approx 1.5\text{-}2.5 \times 10^{-5}$$

The estimate for the cross-section at the peak of the resonance thus becomes:

$$\sigma_p \approx 0.12\text{-}.20 \text{ nb}$$

Now, the width of the beam is roughly twice the assumed width of the resonance. If the beam were centered on the resonance, we would therefore expect an effective cross-section of roughly half the peak value [45].

$$\sigma_{eff} \approx .06\text{-}.10 \text{ nb}$$

Thus, with an integrated luminosity of 710 nb^{-1} and a detection efficiency of 6.3%, one should expect to detect an average of 2 to 5 events.

In conclusion, when interpreted as a resonance, both the mass and the number of events detected during the scan for the $^1P_1$ are very reasonable within the charmonium model.

3.4 Conclusions.

We have described an analysis chain capable of measuring cross-sections of inclusive ψ production, the ψ decaying into an electron positron pair, which are at the level of 10^2 pb using the R704 detector. The analysis leads to a set of 5 events which could stem from decays of the 1^1P_1 charmonium state. Unfortunately, the amount of data taken off resonance is not sufficient to be able to reject the hypothesis that the events are just background events drawn from a distribution which is flat over the range of our scan in mass. However, we add that if we assume that all events seen under the χ_1 scan are stemming from χ_1 decays (they are all compatible with such an assumption), we may reject the background hypothesis at a confidence level which is smaller than 5%. When interpreted as a resonance, the $^1P_1$ mass is at $3525.4 \pm .8 \pm .4$ MeV/c^2, close to the centre of gravity of the ^3P masses. This would indicate that spin-spin forces are small at long distances, supporting the view that the long range forces of QCD are effectively of a scalar nature.

4. *ANGULAR DISTRIBUTIONS.*

4.1 Introduction.

Although the primary goal of the formation of χ_J states in the experiment R704 was to perform precision measurements of masses and widths, it is of interest to study the mechanisms of the reactions $\bar{p}p \rightarrow \chi_J \rightarrow \gamma\psi \rightarrow \gamma e^+e^-$ more closely. A tool for this is to study the angular distributions of the reactions, which will provide information on the formation mechanisms as well as on the nature of the χ_J decay mechanism. Specifically, one should be able to test the validity of the QCD helicity selection rule for the formation process, which applies in the limit of vanishing quark masses. The angular distributions should also provide information on the multipole character of the χ_1 and χ_2 radiative transitions to the ψ. The relative importance of the various multipole amplitudes may in turn be related to the magnetic moment of the charm quark [62,63]. Assuming that a single quark radiates the photon in the transition process (the SQR hypothesis), only the two lowest multipole amplitudes are allowed. The presence of a third multipole coefficient in the χ_2 transition to the ψ may indicate that this assumption is not valid [64]. Finally we may provide a verification of the spins of the two χ_J states under study.

The event sample used in this study is the one found in ref. [51]. In addition, 4 χ_2 events which were found in the 1983 test runs are included in the sample. Hence the data sample contains 30 χ_1 and 54 χ_2

events.

4.2 Helicity Formalism.

We adopt the helicity formalism when describing the angular distributions. Within this formalism, the distributions are expressed in terms of the helicities of the initial,intermediate and final state particles.

The helicity of a particle in flight is defined as:

$$\lambda = \vec{s}.\vec{p}/\|p\|$$

where $\vec{s}$ is the spin of the particle, and $\vec{p}$ is its momentum.

Three angles are necessary to describe the full angular distributions:

θ ; the polar angle of the photon with respect to the antiproton beam, defined in the centre of mass system.(We may choose the azimuthal angle of the photon equal to zero, since the azimuthal distribution of the photons should be isotropic).

θ'; the angle of the positron with respect to the ψ direction of flight, defined in a frame where the ψ is at rest.

φ'; the azimuthal angle of the positron in the ψ frame (the primed frame), where the x' axis is lying in the plane spanned by the photon and the antiproton.

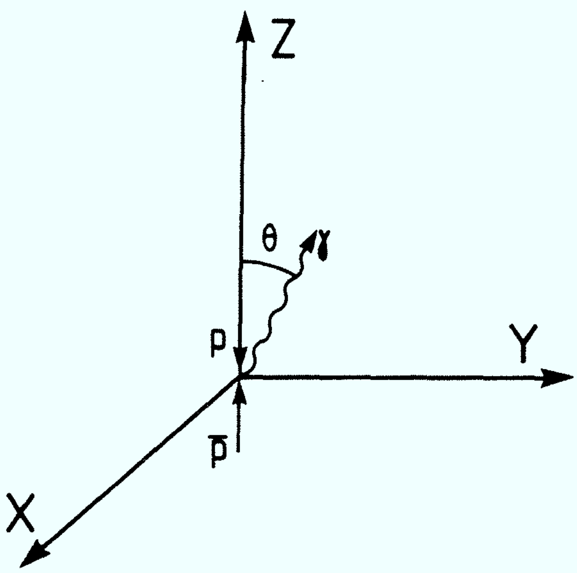

Fig. 4.1: Definition of the angle θ.

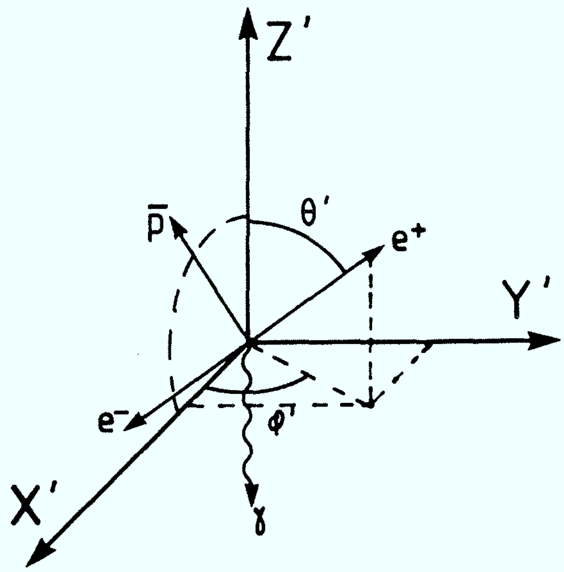

Fig. 4.2: Definition of the angles θ' and φ'.

Fig. 4.1 and 4.2 indicate the angles defined above. The choice of θ as the angle of the γ whith respect to the antiproton direction, rather than with respect to the proton direction, has no importance since the processes under study conserve parity. For this reason, the fact that we do not measure the charge of the particles, hence necessitating a random charge assignment to the electrons, does not impair the analysis either.

In the helicity formalism, the angular distribution is given by:

$$W(\theta,\theta',\varphi') = \sum_M B_M^2 \left(\sum_f \left| \sum_{\lambda_4} d^J_{M,\nu}(\theta)\, D^{1*}_{\lambda_4,\mu}(\varphi',\theta',-\varphi')\, A_\nu \right|^2 \right) .$$

where:

λ_i , i = 1,2..6 are the helicities of the $\bar{p}, p, \gamma, \psi, e^+, e^-$ respectively.

J is the spin of the χ_J state.

M is the component of the χ_J spin onto the $\bar{p}$ direction. $(M=\lambda_1-\lambda_2)$

ν is the component of the χ_J spin onto the ψ direction of flight. $(\nu=\lambda_4-\lambda_3)$

μ is the component of the ψ spin onto the positron direction of flight (in the ψ frame, $\mu=\lambda_5-\lambda_6$).

f is a final state, specified by λ_3, λ_5 and λ_6.

The d-functions are found in e.g. ref. [8], and

$$D^{J*}_{\lambda,\mu}(\alpha,\beta,\gamma) = e^{i\lambda\alpha}\; d^J_{\lambda,\mu}(\beta)\; e^{-i\mu\gamma} .$$

The sum over final states are subject to the constraints $\lambda_3 = \pm 1$ due to the masslessness of the photon, and $\lambda_5 - \lambda_6 = \pm 1$ because of the QED helicity selection rule applying when the electron and positron momenta are much larger than their masses.

B_M and A_v are parameters to be determined. In appendix 2 details on the derivation of the equation above are given. We also note that parity conservation permits us to write:

$$B_{-M} = B_M \equiv B_{|M|} \quad \text{and} \quad A_{-v} = A_v \equiv A_{|v|}$$

We have two normalisation conditions on the maximum of five parameters to be determined:

$$B_0^2 + 2B_1^2 = 1$$

and

$$A_0^2 + A_1^2 + A_2^2 = 1$$

We follow the convention of ref. [65] and put a factor 2 in front of B_1, due to the fact that the χ_J may be produced with 3 values of M, M=-1, M=0 or M=1. We are left with at most three free parameters. The number of free parameters depend on the spin of the χ_J state under study. For the different spins, we note the following:

J=0: Angular momentum conservation implies that $B_1 = A_1 = A_2 = 0$. The χ_0 angular distribution is therefore completely specified.

J=1: Angular momentum conservation implies $A_2 = 0$. Furthermore, we note that in order to conserve angular momentum, parity and charge conjugation in the annihilation process, the χ_1 must be formed in p-wave (L=1), with the proton and antiproton spins coupled to S=1. Since the component of the orbital angular momentum along the $\bar{p}$-p axis must be zero, we find that the Clebch-Gordan coefficient for coupling S=1 and l=1 to J=1 and M=0 is equal to zero. Hence, $B_0 = 0$, and the χ_1 distribution is specified by just one unknown parameter.

J=2: All three parameters are allowed by angular momentum conservation. However, assuming that a single quark radiates the photon in the transition $\chi_2 \rightarrow \gamma\psi$, only the two lowest multipole transition amplitudes are allowed [65]. Hence, the angular distribution should be specified by two unknown parameters. By allowing a non-zero value of the octupole component, we may test the single quark radiation (SQR) hypothesis [64].

The helicity amplitudes describing the $\chi_J \rightarrow \gamma\psi$ transition are related to the multipole amplitudes of the transition in the following way [66]:

$$A_v = \sum_{i=1}^{J+1} a_i \sqrt{(2i+1)/(2J+1)} \langle 1,i,v-1,1|J,v\rangle$$

where $\langle 1,i,v-1,1|J,M\rangle$ is a Clebsh-Gordan coefficient.
Explicitly, the helicity amplitudes become:

For J=1:

$$A_0 = 1/\sqrt{2}(a_1 + a_2)$$
$$A_1 = 1/\sqrt{2}(a_1 - a_2)$$

For J=2:

$$A_0 = 1/\sqrt{10}a_1 + 1/\sqrt{2}a_2 + \sqrt{(2/5)}a_3$$
$$A_1 = \sqrt{(3/10)}a_1 + 1/\sqrt{6}a_2 - \sqrt{(8/15)}a_3$$
$$A_2 = \sqrt{(3/5)}a_1 - 1/\sqrt{3}a_2 + 1/\sqrt{15}a_3$$

where a_1, a_2 and a_3 are the electric dipole, magnetic quadrupole and electric octupole contributions to the radiative transitions. The SQR hypothesis implies that $a_3 = 0$ in the χ_2 decay.

4.3 Determination of the Angles.

Unfortunately there is no direct measurement of the γ direction using the detector. Instead, the γ momentum and direction must be inferred from the reconstructed directions of the electron-positron pair. The momenta of the two electrons are also detemined in this way. This gives a more accurate determination of the momenta than the determination obtained by using the calorimeter measurements. Fig. 4.3 illustrates this point.

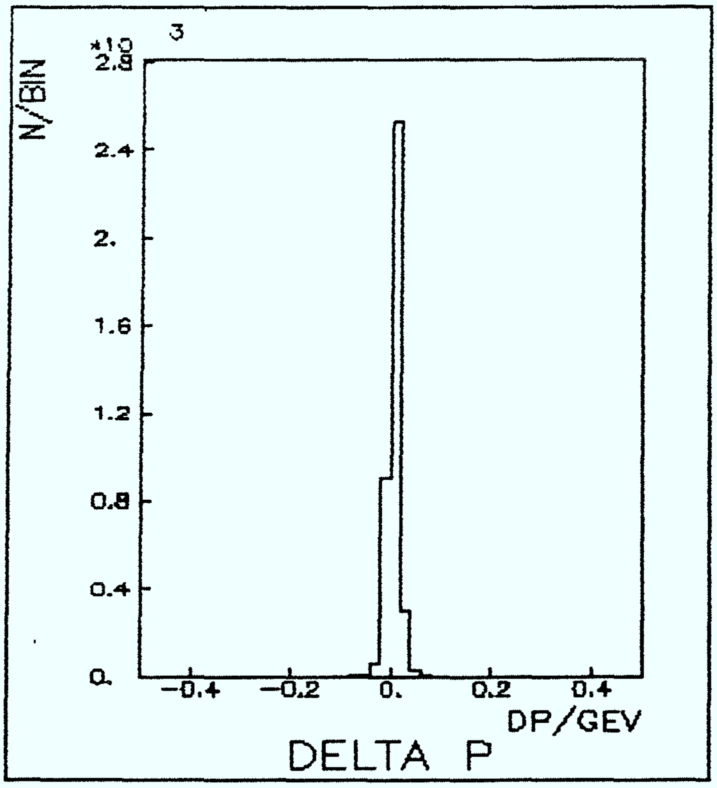

Fig. 4.3: Monte Carlo estimate of the error of momentum reconstruction using the directions determined by the MWPCs. The width of this distribution is 0.02 GeV. Determining the momenta from the calorimetric energy measurements would give a momentum resolution equal to the energy resolution of the calorimeter, 30%/$\sqrt{E}$ (E in GeV), i.e. typically 0.2 GeV.

The five unknown, the three components of the γ momentum and the magnitudes of the two electron momenta, are determined from the four equations of momentum and energy conservation and the constraint that the invariant mass of the e^+e^- pair should be the ψ mass. Details on the calculation are found in refs. [49,50]. The calculation results in solving a quadratic equation, hence two possible solutions for the five unknown are obtained. The solution which is consistent with what is found in the veto counters (signaturing the γ) is picked. Whenever the veto response was compatible with both solutions, the correct solution was easily picked by comparing the expected electron momenta with the calorimetric measurements of the electron energies. Events where the γ direction is predicted to be outside the detector acceptance, or inside one of the main arms, are also accepted for this analysis if the detector response agrees with this prediction.

Having obtained the momenta in the laboratory system, the three relevant angles were extracted in the following manner:

a) The lab momenta are boosted to the centre of mass system (where the χ is at rest). Here θ is calculated.

b) The momenta were boosted to a system where the ψ is at rest.

c) The components of the momenta were calculated in a system which has its z axis parallel to the ψ direction of flight and its x axis in the plane defined by the antiproton and the photon directions. θ' and φ' were found in this system, defined with respect to the electron (or positron) found in arm 1 of the apparatus.

The error in the determination of these angles were found by a Monte Carlo simulation program where events were generated and subsequently tracked through the detector. Signals in the MWPCs were established and coded to raw data format. The directions of the electrons were subsequently reconstructed using the same algorithm as for the real events. Finally the algorithm above was applied to find the three angles. This reconstruction was then compared to the generated angles, and on the basis of figs. 4.4-4.6 the following resolutions were deduced:

$$\sigma(\cos(\theta)) = 0.02$$

$$\sigma(\cos(\theta')) = 0.045$$

$$\sigma(\varphi') = 0.08 \text{ rad} \quad (4.5^0)$$

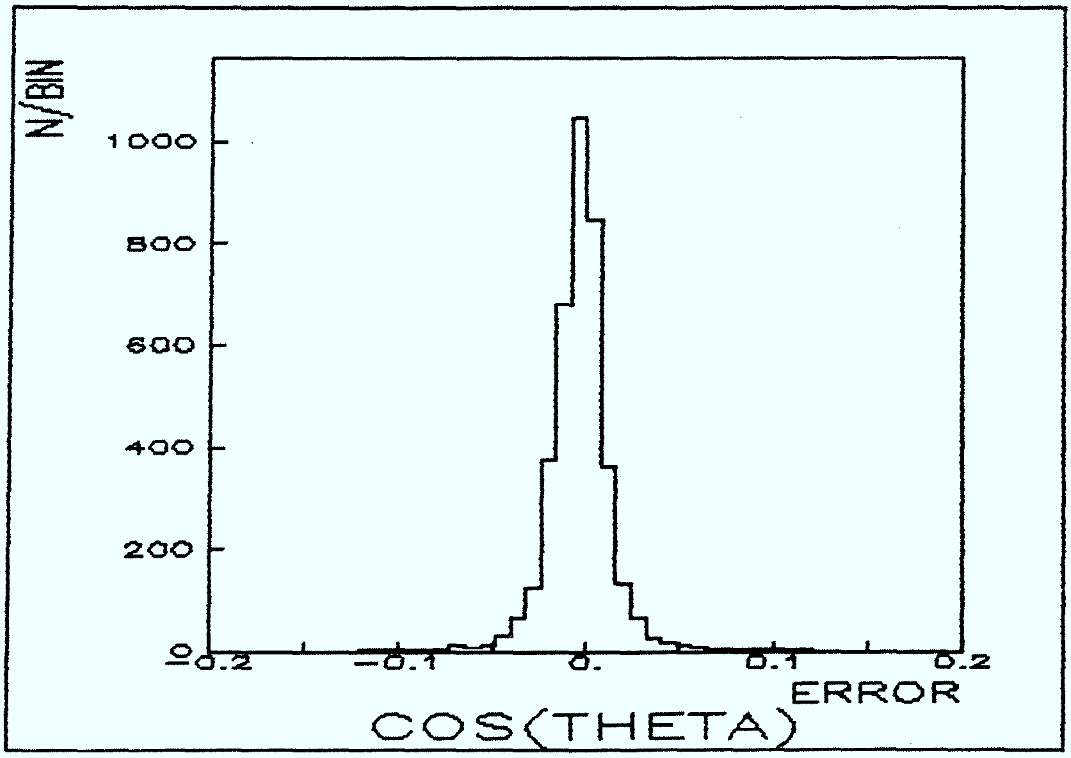

Fig. 4.4: Distribution of the error in the reconstruction of cos(θ). (from Monte Carlo simulations)

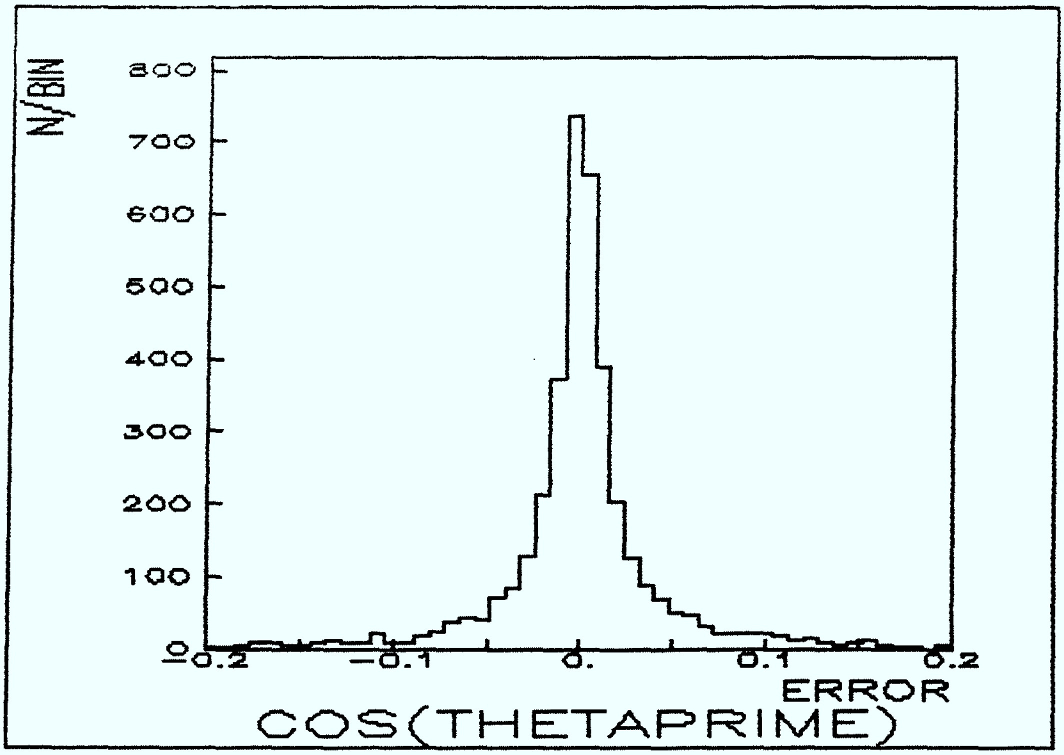

Fig. 4.5: Distribution of the error in the reconstruction of cos(θ'). (from Monte Carlo simulations)

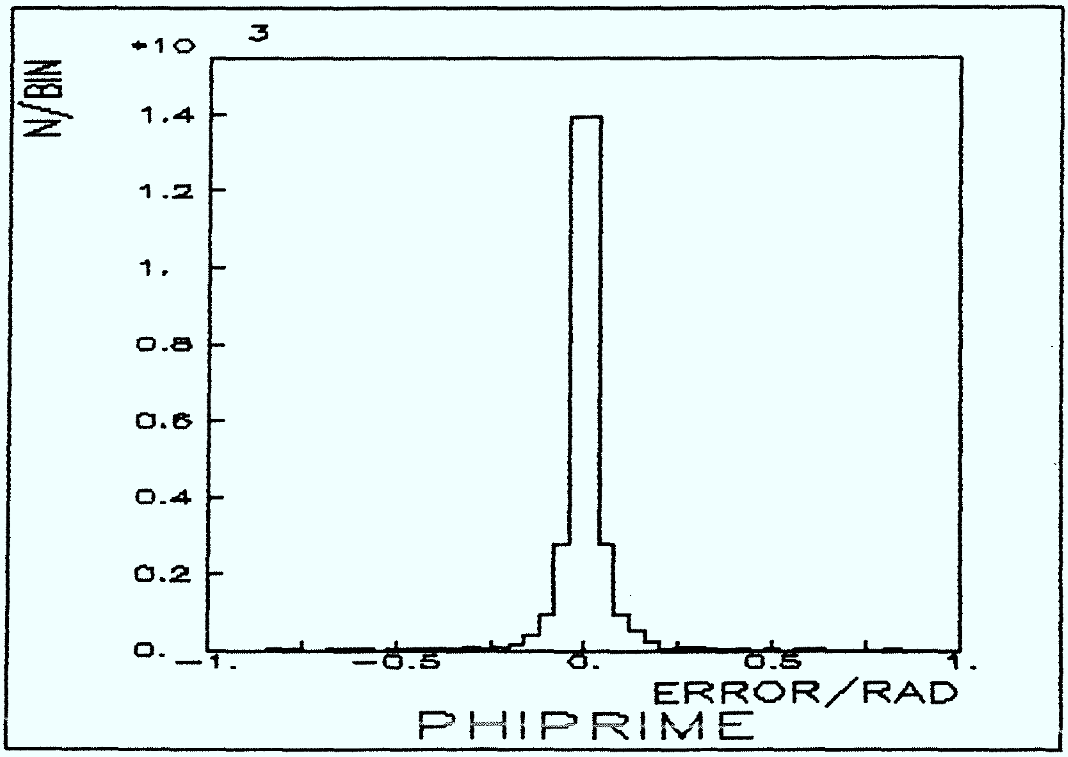

Fig. 4.6: Distribution of the error in the reconstruction of φ'. (from Monte Carlo simulations)

A problem arose when the two solutions of the quadratic equation for the momenta became identical. This happened in the case of a symmetric decay of the ψ, i.e. $\cos(\theta') = 0$. Due to the fact that the reconstruction of the electron direction is inaccurate, the discriminant in the solution could sometimes become negative. This was seen both in the data and in the Monte Carlo simulations. Whenever this happened, the discriminant was simply put to zero. This is equivalent to putting $\cos(\theta') = 0$. The effect of doing this has been studied by Monte Carlo simulations, and although the errors increased somewhat, they remained much smaller than the bin size introduced in the binned analysis of the data. Events with a reconstruction leading to a complex solution for the momenta always had $|\cos(\theta')| < 0.2$. 11 out of the 84 events had this problem. This is in agreement with the Monte Carlo studies, showing that 7% of the χ_1 and 12% of the χ_2 had a reconstruction yielding a negative discriminant[67].

4.4 Acceptance Calculations.

The geometrical acceptance was studied by Monte Carlo simulations, separately for the χ_1 and the χ_2. The MWPCs defined the geometrical acceptance. In addition, uneven detection efficiencies had to be accounted for. While the efficiencies of the trigger hodoscopes were at nearly 100% throughout the detector acceptance, the Cerenkov efficiencies turned out to be fairly uneven. The trigger efficiencies of these counters were substantially lower close to the edge of the acceptance than in the middle. This has been studied, and the efficiencies could be approximated by the formula [68]:

$$\varepsilon = (1 - 5.0\times10^{-4}(42.5-\theta_1)^2)\times(1 - 4.5\times10^{-4}\varphi_1^2)$$

where θ_1 and φ_1 are measured in degrees (in the laboratory system). The efficiencies were assumed to be identical for both counters.

The full $\cos(\theta)\times\cos(\theta')\times\varphi'$ space was divided into 15x15x15 =3375 bins, and the acceptance was calculated separately in each bin, assuming an isotropic distribution of events. Due to the large number of bins, these calculations required rather large amounts of computer resources. Two Monte Carlo simulations were carried out for each of the two χ_J states; one where the Cerenkov efficiencies were accounted for, and one where these were ignored. This was necessary in order to study the effects of the Cerenkov efficiencies on the fitted parameters. It was found that the two assumptions of the Cerenkov efficiencies yielded compatible values of the fitted parameters. The uncertainty introduced due to inaccurate knowledge of the Cerenkov efficiency is small when compared to the statistical errors.

State:	χ_1	χ_2
Geometric acceptance:	11.2%	10.9%
Including Cerenkovs:	8.0%	7.7%

Acceptance curves were also produced in the three projections $\cos(\theta)$, $\cos(\theta')$ and φ' (fig. 4.7). The shape of these curves are only of an indicative character, since the probability of detecting an event with a particular value of one of the three angles actually depend on the shape of the full angular distribution. However, with the fine binning used in determining the acceptance, this probability could be calculated under any specific assumption of the full angular distribution by integrating numerically over the two other angles.

a)

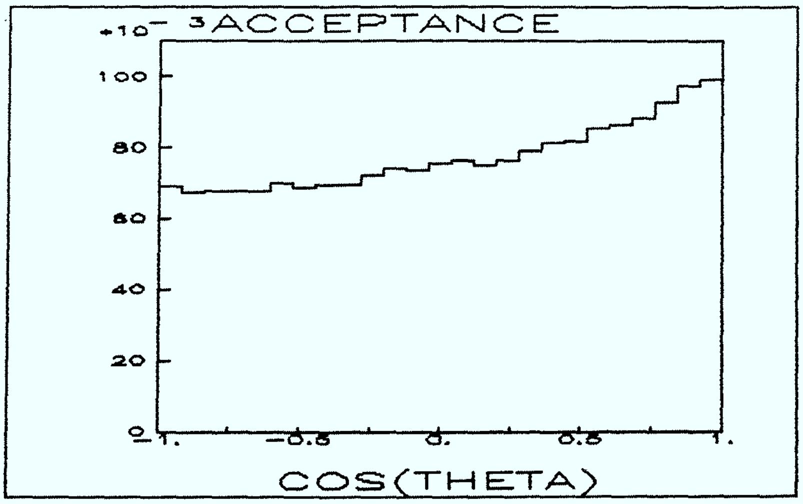

b)

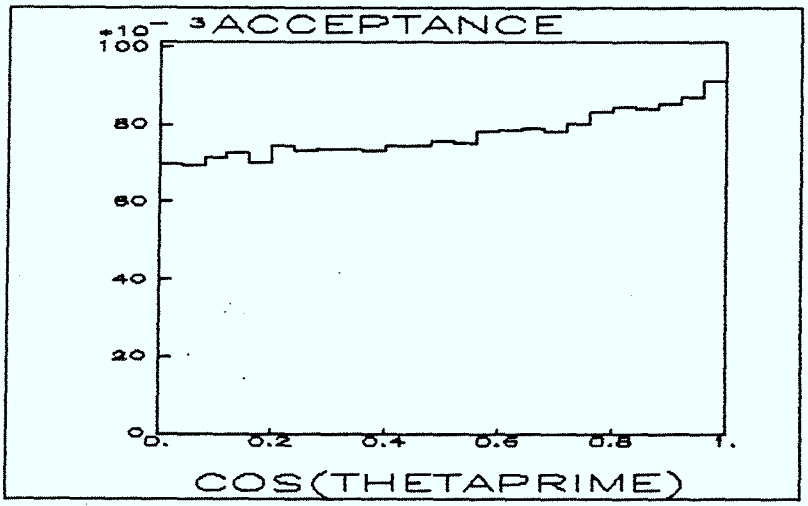

c)

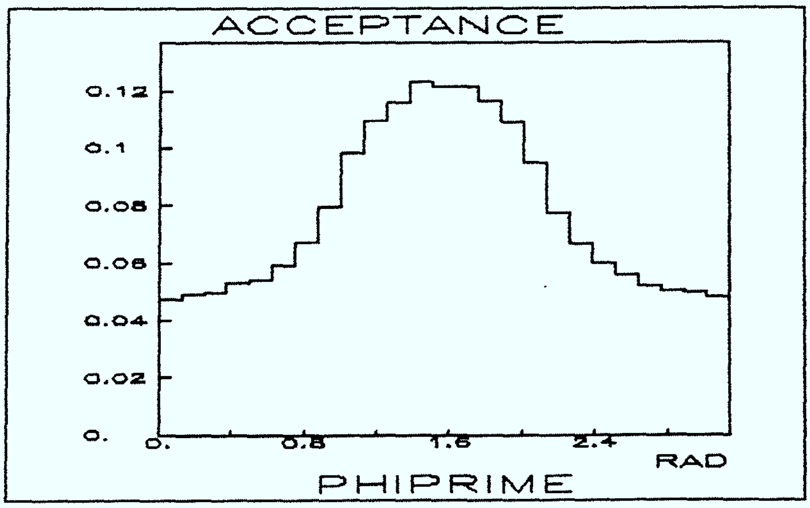

Fig. 4.7: Geometrical acceptances in the three projections. a) cos(θ), b) cos(θ'), c) φ'.

4.5 Features Apparent in the Raw Distributions.

Before turning to a full likelihood analysis of the distributions, it is informative to study the shape of the raw distributions in light of the shapes expected for several values of the parameters and the indicative efficiency curves. In figs.4.8-4.9 we show the raw distributions in cos(θ), cos(θ') and φ' for the two event samples. The cos(θ) distribution of the χ_2 events seems to peak at |cos(θ)| = 1. In cos(θ'), no strong angular dependence are seen in any of the two distributions. The shape of the φ' raw distributions are due to the shape of the acceptance.

In fig. 4.10-4.11 we show the theoretical distributions in cos(θ) and cos(θ') for several values of the parameters. For the χ_1 case, we note that the distribution in cos(θ') depends heavily on a_2, and that a nearly isotropic distribution both in cos(θ) and cos(θ') implies that the a_2 component should be small. For the χ_2 case, note that for a distribution which peaks at |cos(θ)|=1, one should expect a positive value of a_2, regardless of the value of the other free parameter, B_0. Given a value of a_2, the shape of the cos(θ) distribution seem to vary very slowly with B_0. Unfortunately, the distribution in cos(θ') seems to be compatible with any value of a_2.

a)

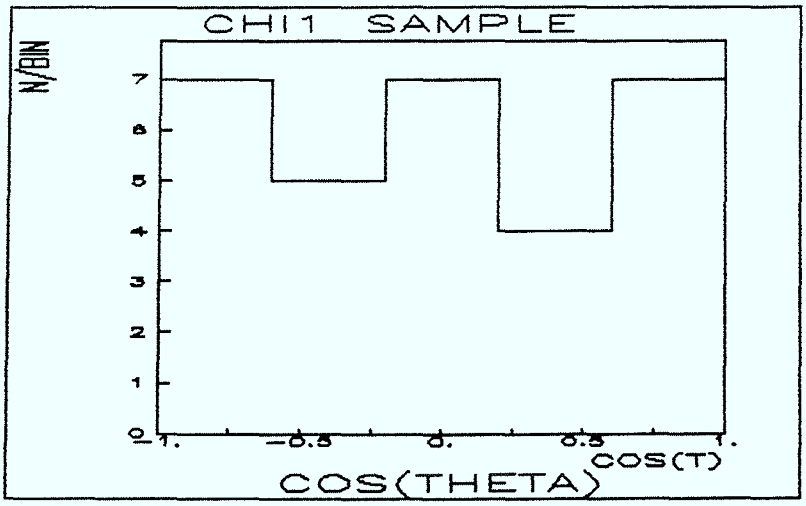

b)

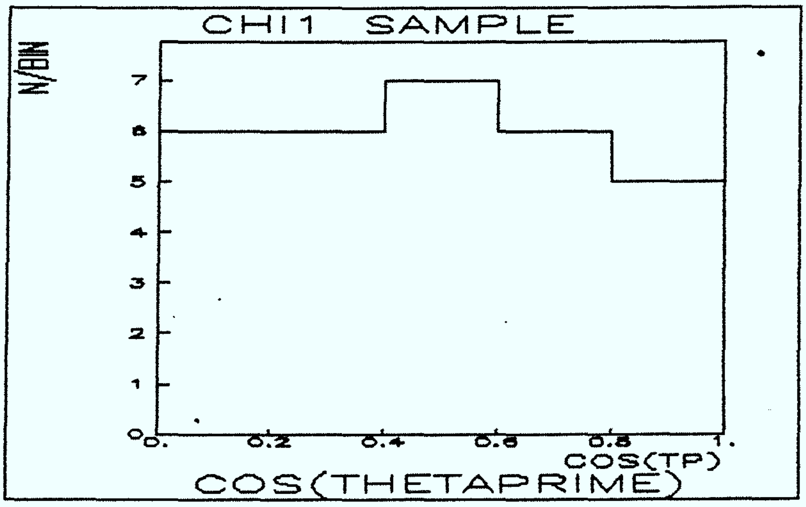

c)

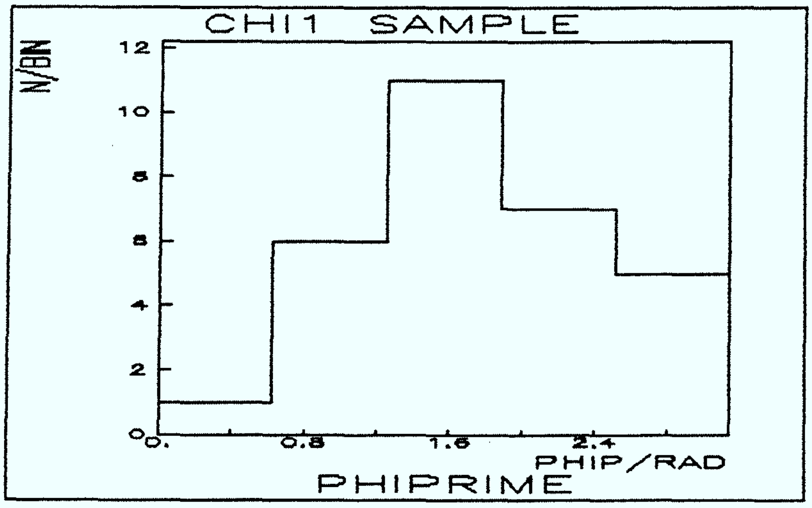

Fig. 4.8: Raw distributions in the three projections for the χ_1 sample. a) $\cos(\theta)$, b) $\cos(\theta')$, c) φ'.

a)

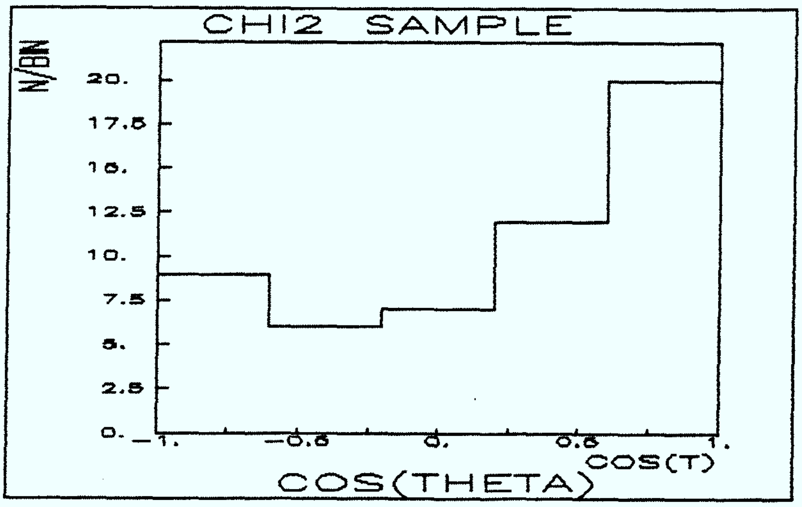

b)

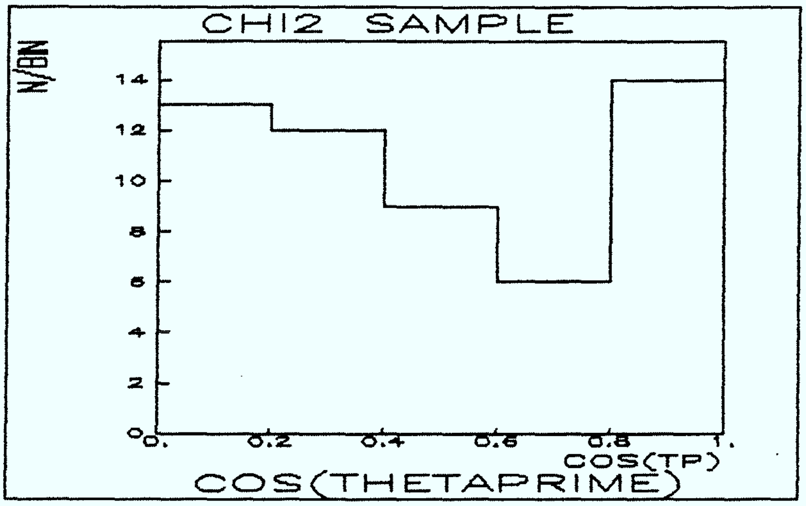

c)

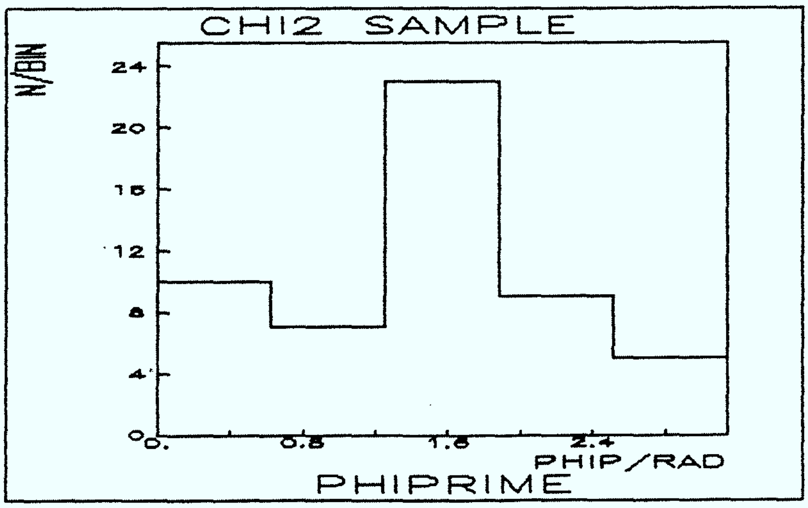

Fig. 4.9: Raw distributions in the three projections for the χ_2 sample. a) $\cos(\theta)$, b) $\cos(\theta')$, c) φ'.

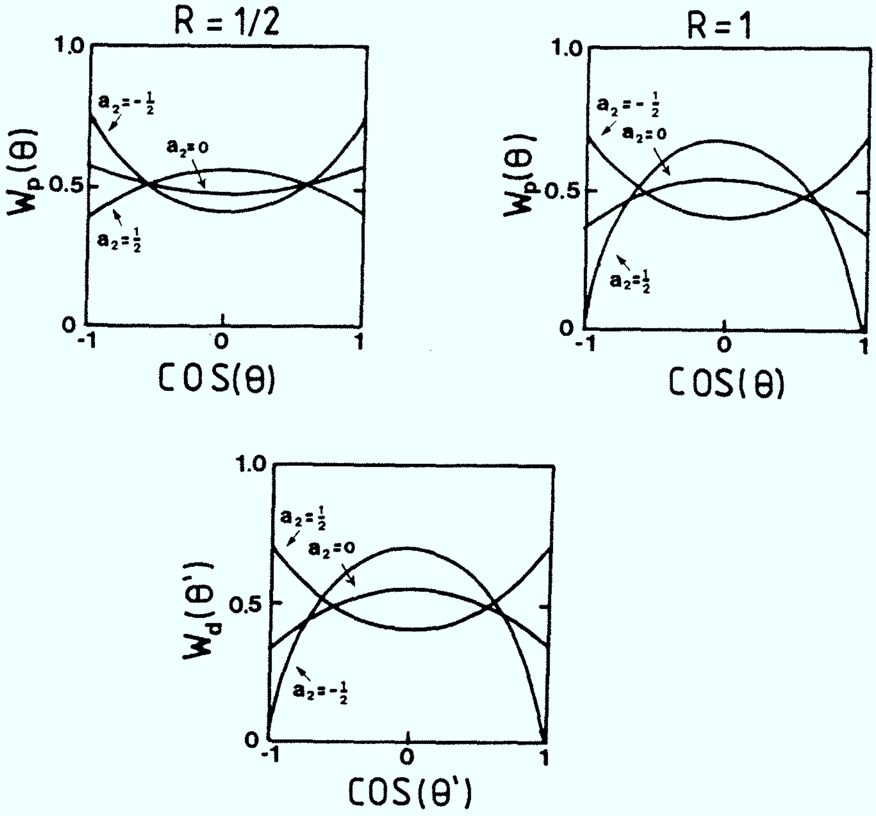

Fig.4.10: Theoretical distributions for a spin 1 hypothesis for various assumptions on the parameters. R = $2B_1^2/(B_0^2+2B_1^2)$

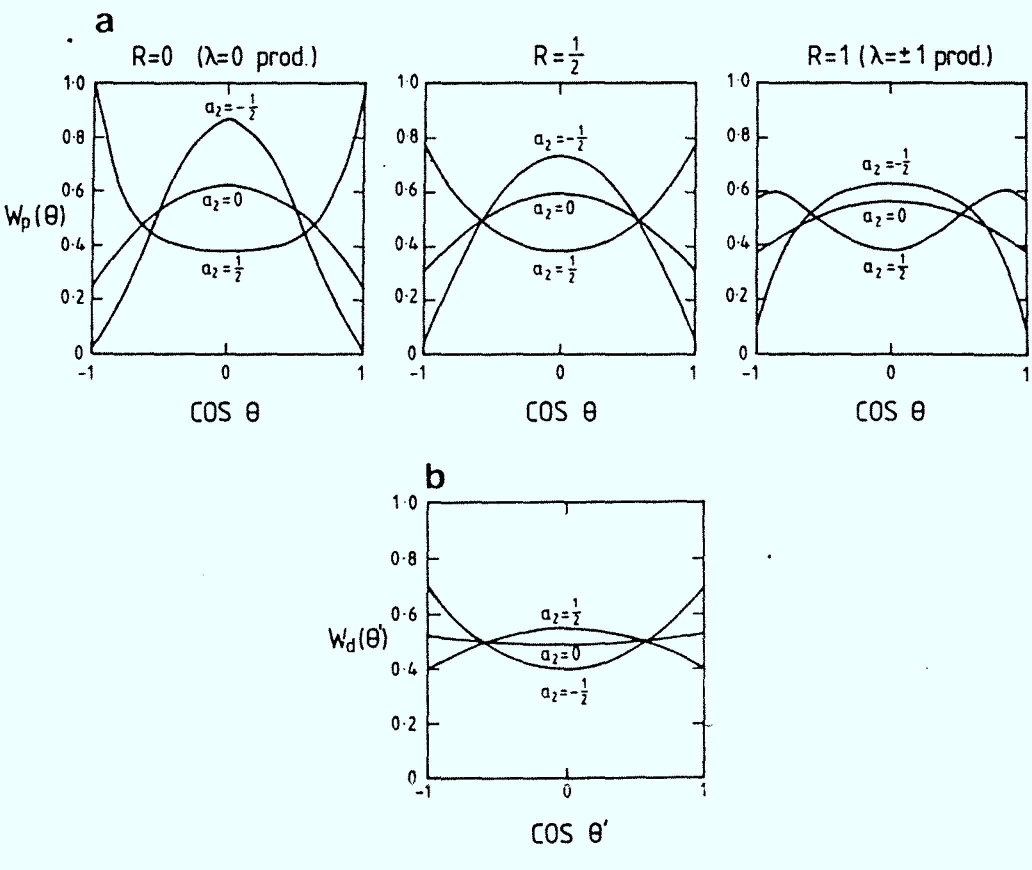

Fig.4.11: Same as fig. 4.10 for the spin 2 hypothesis. From [65].

4.6 Analysis of the Angular Distribution.

4.6.1 Choice of Method.

It is well known that binning the data introduces losses of information on the parameters to be determined. However, using an unbinned maximum likelihood function requires that the detector resolution is known at every point of the detector. In addition, no bias should be present in the data.

We have seen that the information on $\cos(\theta')$ for 11 of the 84 events is rather poor, $|\cos(\theta')| < 0.2$. Putting $\cos(\theta')=0$ for all these events, would certainly introduce a bias to the analysis. Moreover, the error on the two remaining angles are also larger for these events than for the rest of the sample.

This is the reason why we have chosen to perform a binned analysis, where the bin size is larger than 0.2 in $|\cos(\theta')|$. It was also felt that the bin widths should be comparable in the three variables $\cos(\theta)$, $\cos(\theta')$ and φ'. By classifying the data in bins which were much larger than the detector resolution, biases due to the detector resolution were also avoided. A preliminary investigation showed that the uncertainty in the determination of the parameters in any case was dominated by the limited number of events. A few comments on statistics are given in appendix 4.

4.6.2 Parity Transformations.

The three sub-processes $\bar{p}p \rightarrow \chi_J$, $\chi_J \rightarrow \gamma\psi$ and $\psi \rightarrow e^+e^-$ are separately invariant under parity transformations. This property was exploited in order to reduce the range of some angles. The effect of a parity transformation of the sub-processes are the following:

$$\bar{p}p \rightarrow \chi_J: \qquad \cos(\theta) \rightarrow -\cos(\theta)\ ;$$
$$\varphi' \rightarrow \varphi' + \pi \qquad \text{(modulo } 2\pi)$$

$$\chi_J \rightarrow \gamma\psi: \qquad \cos(\theta) \rightarrow -\cos(\theta)\ ;$$
$$\cos(\theta') \rightarrow -\cos(\theta')$$

$$\psi \rightarrow e^+e^-: \qquad \cos(\theta') \rightarrow -\cos(\theta');$$
$$\varphi' \rightarrow \varphi' + \pi \qquad \text{(modulo } 2\pi)$$

By inspecting the explicit expansions of the angular distributions, it was verified that these transformations actually leaved the distribution functions unchanged. Parity transformations were applied to the data on an event to event basis in order to restrict the range of $\cos(\theta)$ and $\cos(\theta')$ to only positive values, thus enhancing the statistics of the remaining volume of angles by a factor of 4. Since each of the parity transformations involved a transformation of two of the three angles, one of the angles had to run over its full range.

4.6.3 Constructing the Likelihood Function.

The data were divided into a total of 45 bins, three $\cos(\theta)$ and $\cos(\theta')$ bins ranging from zero to one, and five bins in φ, ranging from 0 to 2π. The events were assumed to be distributed among the bins according to a multinomial distribution law:

$$L(N,\vec{n},\vec{p}) = N! \prod_{i=1}^{45} \frac{p_i^{n_i}}{n_i!} \qquad \sum_{i=1}^{45} p_i \equiv 1$$

where N is the total number of events, n_i is the number of events in bin i and p_i is the probability that an event will fall into bin i. This probability is given by:

$$p_i = \frac{\int_{\Delta\Omega} W(\theta,\theta',\varphi',B_0,a_2 \ldots)\varepsilon(\theta,\theta',\varphi')\, d\Omega}{\int_{\text{full space}} W(\theta,\theta',\varphi',B_0,a_2 \ldots)\varepsilon(\theta,\theta',\varphi')\, d\Omega}$$

where $W(\theta,\theta',\varphi',B_0,a_2 \ldots)$ is the theoretical distribution, a function of the angles and the unknown parameters, and $\varepsilon(\theta,\theta',\varphi')$ is the overall detection efficiency at the specified angles. As mentioned in section 4.4, an estimate of the detection efficiency was made separately in 3375 cells of the three-dimensional space of angles. This information was now used to approximate the expression above by:

$$p_i \approx \frac{\sum_{j=1}^{75} W_{ij}\, \varepsilon_{ij}\, \Delta\Omega_{ij}}{\sum_{j=1}^{3375} W_j \varepsilon_j \Delta\Omega_j}$$

where W_j and ε_j are averages of the theoretical distributions and detection efficiencies over the range of cell j. The 75 numbers ij, j=1,2,....,75 are the appropriate cells within a bin of the likelihood function.

The most probable values of the parameters B_0, a_2 .. are those which maximise the likelihood function. In order to find the parameters, the negative logarithm of the likelihood function was minimised using the Minuit [69] program package.

In order to check the method above, events were generated according to angular distributions brought about for several different values of the parameters to be determined. Appendix 3 gives some details on Monte Carlo generation according to a distribution. Subsequently, events were selected by imposing acceptance and efficiency criteria. Finally the Monte Carlo events were subjected to the maximum likelihood analysis. This procedure proved very useful when debugging the program performing the likelihood analysis. The input parameters were reproduced to within the errors given by the analysis. Using a large number of evets as input, the parameters were reproduced with great accuracy.

4.7 Results.

The results are grouped into three sections. In the first section, we test the Single Quark Radiation hypothesis, i. e. we look for a non-zero electric octupole component in the χ_2 distribution. In the second section, we present our determination of the parameters under the assumption that the SQR rule is valid. In the first two sections, we make the conventional assumptions of the spins of the χ_1 and the χ_2. Finally, we attempt to verify the spins of the χ_1 and the χ_2. All errors quoted correspond to a rise of the negative log of the likelihood function of 0.5.

4.7.1 Testing the SQR hypothestis.

For the χ_2 events, the unprejudiced angular distribution depend on three parameters, B_0, a_2 and a_3. Hence, a full analysis of the angular distribution should determine all three variables, although the assumption that one of the quarks radiate a photon during the process $\chi_2 \rightarrow \psi\,\gamma$ would prohibit an a_3 component. In table 4.1 we present the results of the three parameter likelihood fit to the data. Furthermore this fit is compared to the fit obtained by leaving just two parameters free (putting $a_3 = 0$).

Hypothesis:	Parameter:	Value:
a_3 present	B_0	<.8
	a_2	$.47 \pm .26$
	a_3	$.09 \pm .2$
no a_3	B_0	<.7
	a_2	$.46^{+.19}_{-.18}$

Table 4.1: Likelihood fits to the χ_2 sample under two different assumptions.

We see that a_3 is compatible with zero. Furthemore, putting a_3 to zero does not significantly alter the values obtained for B_0 and a_2 when performing a new likelihood fit. Hence, our data are consistent with the SQR hypothesis.

4.7.2 Determining the parameters.

In this section, we assume that $a_3 \equiv 0$ for the χ_2 distribution. Although B_0 is expected to be equal to zero for the χ_1 data, we perform two fits with the χ_1 data, one where B_0 is left free, and one where this parameter is fixed to zero. The results are the following:

Sample:	Assumptions:	Parameter:	Value:
χ_1	none	B_0	$< .83$
		a_2	$-.10^{+.34}_{-.26}$
	$B_0=0$ *	a_2	$-.13^{+.19}_{-.18}$
χ_2	$a_3=0$	B_0	$< .70$
		a_2	$.46 \pm .19$

Table 4.2: Helicity zero components and magnetic quadrupole components determined from the maximum likelihood fits of the χ_1 and χ_2 samples.

Contours of the likelihood functions are shown in fig. 4.12. In fig. 4.13 we show the raw distributions in $\cos(\theta)$ compared to the theoretical distributions for the fitted parameters, and the acceptance corrected theoretical distributions.

a)

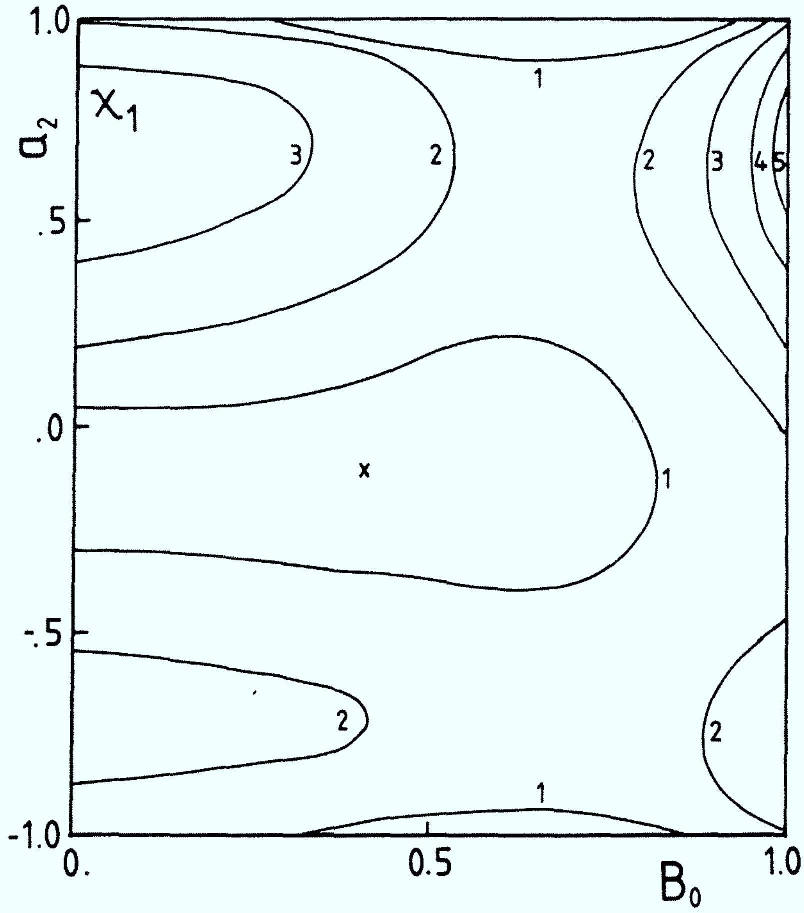

b)

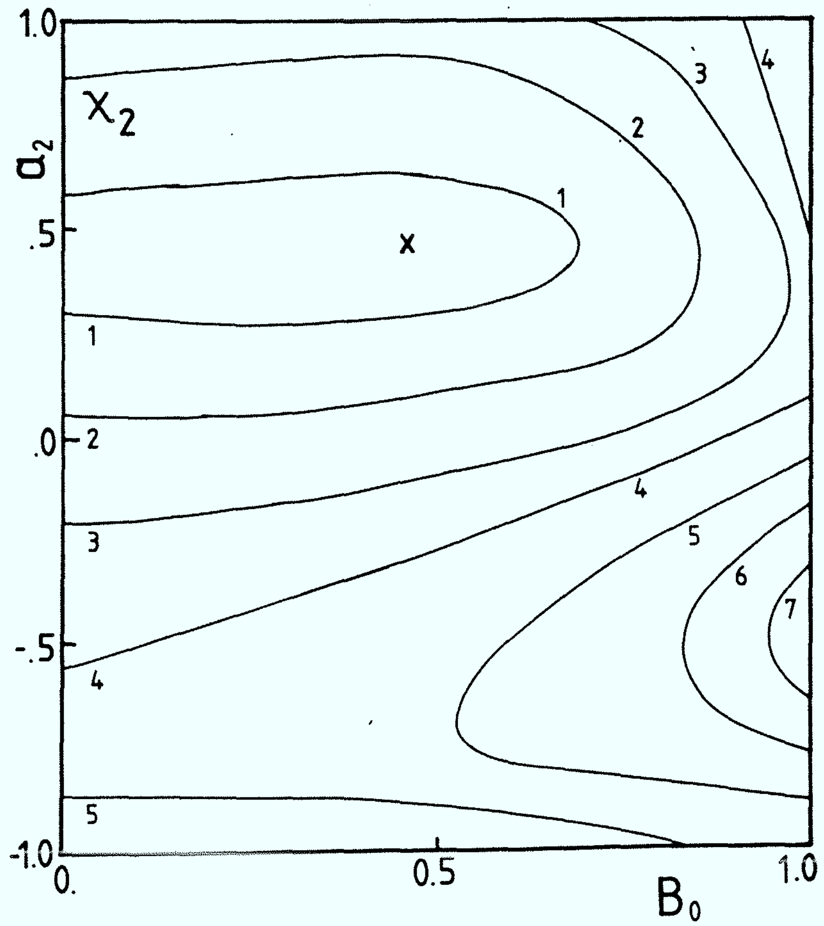

Fig.4.12: Likilihood contours in the B_0 - a_2 plane for the χ_1 (a) and χ_2 (b) events. Contour number n corresponds to a decrease of the likelihood function by a factor $\exp(-0.5n^2)$ with respect to its maximal value. The maximum of the likelihood function is indicated by a cross.

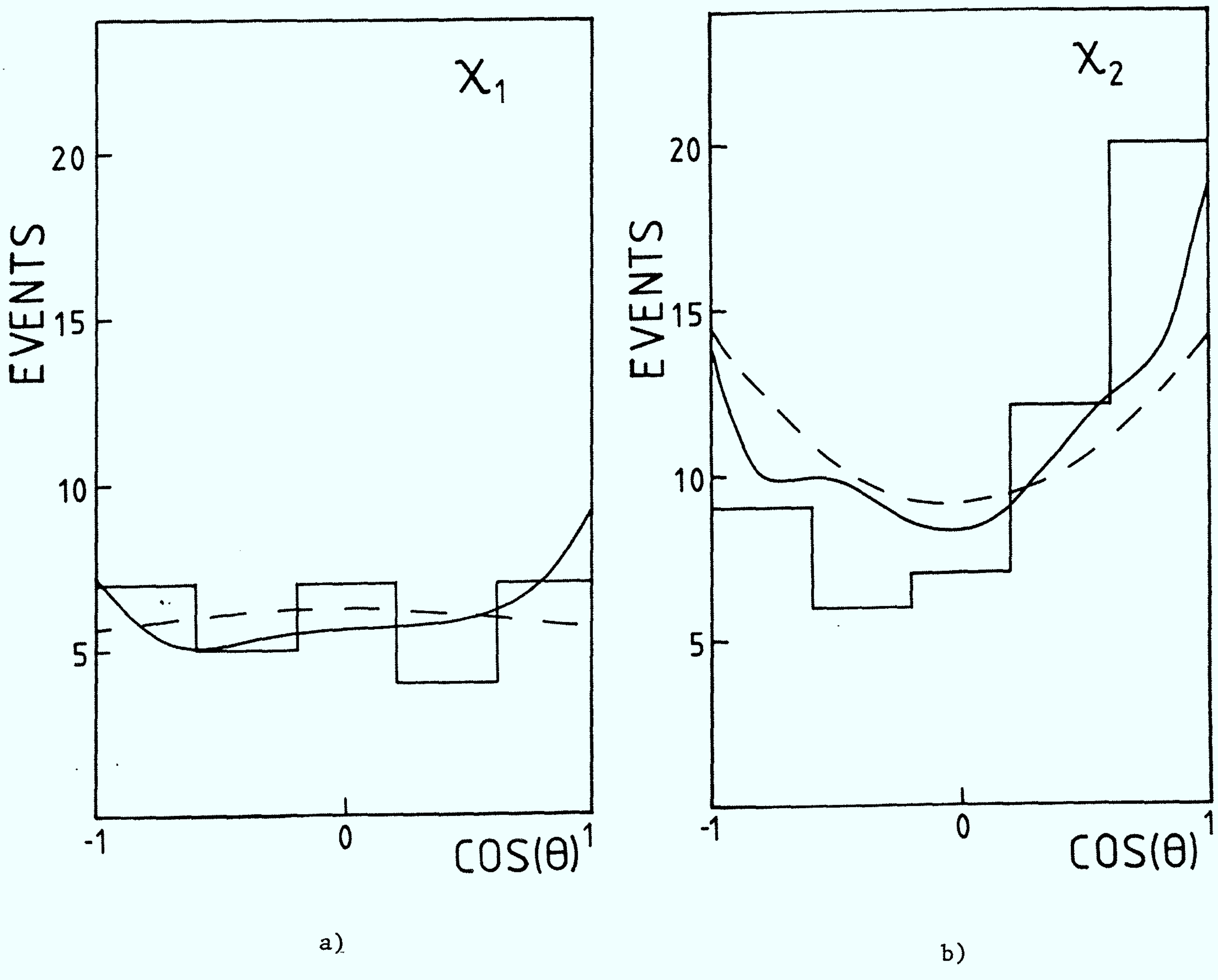

Fig.4.13: Distribution of the angle of the photon with respect to the antiproton-proton axis, θ, for the χ_1 (a) and χ_2 (b) events. Dashed line indicates the theoretical distribution for the preferred value of the parameters. The solid line indicates the distribution expected for these values of the parameters when the detector acceptance is taken into account.

4.7.3 Spin Tests.

Although the spins of the χ_1 and χ_2 states are well established, [70,8], it is of interest to attempt to perform an independent verification. The verification of the spins will also serve as a check of the consistency of the results above.

In order to increase the power of our tests, we make several assumptions on the parameters. Both theoretical considerations [62,63] and experimental data support that the a_2 component of the χ_1 transitions should be small. All existing data for the χ_1 (under a spin 1 assumption) yield results where a_2 is compatible with zero [70,71]. This experiment also agrees with this. Hence, we assume that the spin 1 transition to the ψ is pure dipole. Furthermore, we assume that $B_0 = 0$ for the spin 1 case. However, we do not feel that we are in the position to make any assumptions on a_2 and B_0 for the spin 2 case. In fact a non-zero value of a_2 is reported both in ref. [70] and in this experiment. Due to the limited statistics, we refrain from testing the spin 2 hypothesis with two free parameters for the χ_1 data. The aim of this analysis is thus to attempt to reject spin 0 for the χ_1 data, and to reject spin 0 and spin 1 for the spin 2 data.

The spin analysis is based on the binned likelihood function which is defined in sect. 4.6.3. The value of the likelihood function depends on the underlying spin and multipole hypotheses and on the data (number of events and distributions). Specifically, we define:

L_0 = Likelihood for a spin 0 hypothesis.
L_1 = Likelihood for a spin 1 hypothesis.
L_2 = Likelihood for a spin 2 hypothesis, with a_2 and B_0 as found from the χ_2 data.

Furthermore, we define the following ratios:

$$R_{01} = -\ln(L_0/L_1) \;;\quad R_{02} = -\ln(L_0/L_2) \text{ and } R_{12} = -\ln(L_1/L_2).$$

These ratios are random variables whose distributions depend on the input data (i.e. on the number of events and their distribution among the bins). For the experimental data we calculated the following quantities:

R_{01}^{exp} ; calculated using the 30 χ_1 events,

and:

R_{02}^{exp} and R_{12}^{exp} ; calculated using the χ_2 events.

Furthemore, we define the confidence levels:

$$C.L. = \int_{R_{ij}^{exp}}^{\infty} P_k(R_{ij})dR_{ij}$$

where $P_k(R_{ij})$ is the expected distribution of R_{ij} for a specific spin hypothesis and a specific number of events. Clearly, a low value of the confidence level indicates that the tested hypothesis is false. Due to the limited statistics, asymptotic theorems for binned data may not be applied. Instead, the confidence levels are computed by comparing R_{ij}^{exp} with distributions of these quantities which are found by performing Monte Carlo simulations of the experiment, when events are generated according to specific assumptions of the spins. Acceptance criteria were also imposed during the simulations of the experiments. A large number of experiments were simulated, and it was found that the distributions, $P_k(R_{ij})$, could be well approximated by gaussians. Assuming gaussian distributions, the confidence levels

a)

b)

c)

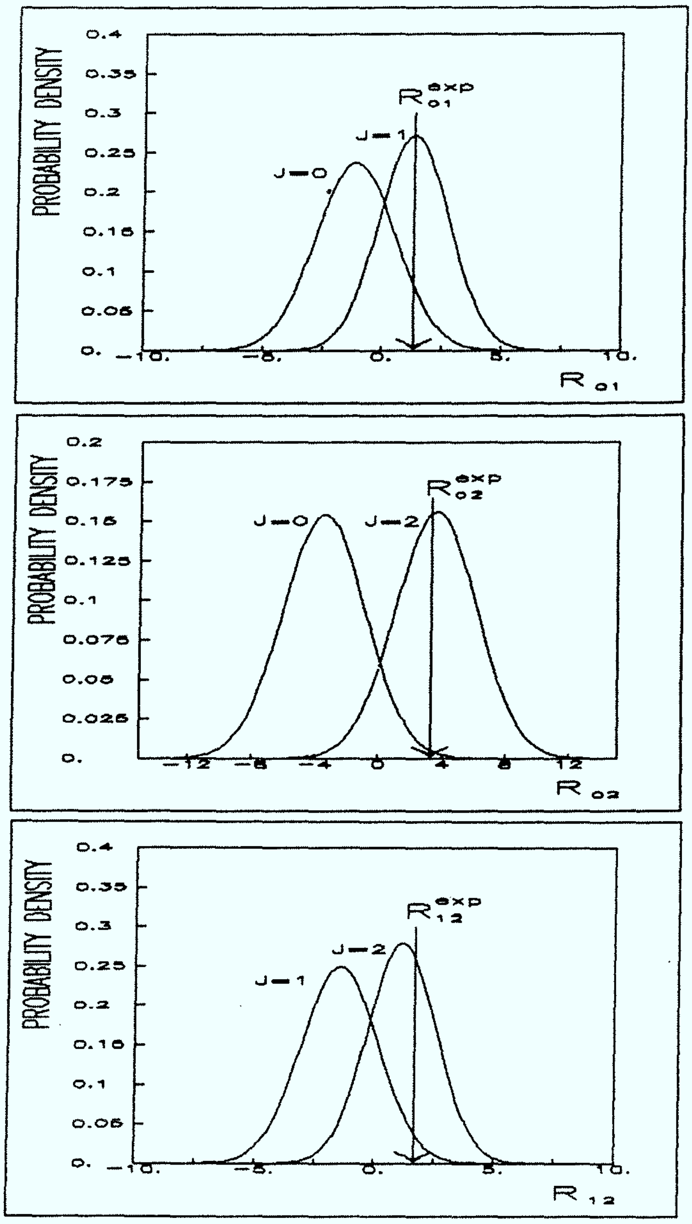

<u>Fig.4.14:</u> a) Spin 0 test for the χ_1 data. The quantity $R_{01} = -\ln(L_0/L_1)$ from the experimental data is compared to the distribution of this quantity expected for spin 0 events and that expected for spin 1 events. L_0 is the likelihood for spin 0, and L_1 is the likelihood for spin 1. The distributions were found by Monte Carlo simulation, and it was found that they could be very well approximated by gaussians.

b) Same as a) for the χ_2 data. $R_{02} = -\ln(L_0/L_2)$ where L_0 is the likelihood for spin 0, and L_2 is the likelihood for spin 2 with the experimentally found values of the parameters from the χ_2 sample.

c) Same as b), but here the χ_2 data are tested against a spin 1 hypothesis.

found in table 4.3 were deduced:

Sample	Test function	C.L. for J=0	C.L. for J=1	C.L. for J=2
χ_1	R_{01}	7.5%	50.4%	-----
χ_2	R_{02}	0.3%	-----	36.0%
χ_2	R_{12}	----	4.5%	55.2%

Table 4.3: Confidence levels of spin tests.

These results are illustrated in fig.4.14. The results show that the conventional spin assignments are favoured. However, using a 1% criterion for rejecting an hypothesis, only the spin 0 hypothesis for the χ_2 state is ruled out by this test.

4.8 Multipole Transitions and the Quark Magnetic Moment.

The nature of the radiative transitions depend naturally on the properties of the charmed quarks. Specifically, the angular distributions are sensitive to the quark magnetic moment. In [62], contributions to the dipole and quadrupole amplitudes are calculated, and the following relations between the multipole coefficients are deduced:

$$\frac{a_2}{a_1} = \frac{-\varepsilon(1+\kappa)}{1+\varepsilon\kappa} \times \begin{cases} 1 & \text{for the } {}^3P_1 \text{ state} \\ \sqrt{(9/5)} & \text{for the } {}^3P_2 \text{ state} \end{cases}$$

where $\varepsilon = p_\gamma/4m_c$.

Taking $m_c = 1.6\ \text{GeV}/c^2$, we obtain, from the χ_1 result on a_2:

$$\kappa = 1.2 \begin{matrix} +5.0 \\ -2.5 \end{matrix}$$

and, from the χ_2 result:

$$\kappa = -4.2 \pm 1.1$$

Unfortunately, this does not represent a very good measurement of the quark anomalous magnetic moment. We have not been able to explain the inconsistency. More data are needed in order to decide whether the unexpected trend of the χ_2 distribution is a physical effect or a stastistical fluctuation. A third possibility is of course that some detector inefficiency is not accounted for (e.g. in the veto counters). This should however not alter the distribution in $\cos(\theta)$ too dramatically since the analysis chain is in fact aiming at finding all inclusive ψs, regardless of the presence of a γ. Only at the very last stage, we require response of the vetos and the remaining part of the detector to be consistent with the expected kinematics. Very few events are rejected due to this requirement. Furthermore, the background is expected to be low. A worst case estimate of the background may be made by considering the whole scan for the ${}^1P_1$ as off resonance data for the χs. Two events in 1019 nb^{-1} of integrated luminosity were found to be compatible with a $\psi\gamma$ final state. These events are part of the ${}^1P_1$ sample described in chapter 3. When interpreted as background events, this should lead to an estimate of 2.6 ± 1.6 background events in the χ_1 and χ_2 samples where 1369 nb^{-1} were collected.

The rates of the transitions $\chi_J \rightarrow \gamma\psi$ are also affected by an anomalous magnetic moment. To order ε, the rates are given by[62]:

$$\Gamma_J(\varepsilon) = \Gamma_J(0)(1+2\varepsilon\kappa\langle\vec{L}.\vec{S}\rangle)$$

where $\Gamma(0)$ is the zero order dipole approximation of the width, given by:

$$\Gamma_J(0) = \frac{p_\gamma^3}{(2J+1)} \frac{4\alpha q^2}{27} \quad |\langle 1p|r|1s\rangle|^2$$

where q is the charge of the c quark. The model-dependent matrix element cancels in the ratio:

$$\frac{\Gamma_1(\varepsilon)}{\Gamma_2(\varepsilon)} = \frac{5\ p_{\gamma 1}^3 (1-2\varepsilon\kappa)}{3\ p_{\gamma 2}^3 (1+2\varepsilon\kappa)}$$

Using the R704 measurements of the widths:

$$\Gamma_1 < 1.3 \text{ MeV} \ ; \quad \Gamma_2 = (2.6\ {}^{+\,1.4}_{-\,1.0}) \text{ MeV},$$

and the measured branching ratios [8]:

$$BR(\chi_1 \rightarrow \gamma\psi) = (25.8 \pm 2.5)\ \%,$$
$$BR(\chi_2 \rightarrow \gamma\psi) = (14.8 \pm 1.7)\ \%,$$

we arrive at $\kappa > -2.2$ (84% c.l) by the formula above. This result favours the result on κ obtained from the χ_1 angular distribution.

4.9 Conclusions

The angular distributions of the processes $\bar{p}p \rightarrow \chi_{1,2} \rightarrow \gamma\psi \rightarrow \gamma e^+ e^-$ are consistent with the conventional spin assignments of the χ states. When allowing for an electric octupole component in the χ_2 radiative transition to the ψ, we find that the distribution is also consistent with the assumption that a single quark radiates the photon. This assumption prohibits an electric octupole component. While the fitted magnetic quadrupole amplitude of the χ_1 distribution is consistent with zero, we find a positive value of this amplitude for the χ_2 case.

This is in contradiction with a previously reported result [70]. From the χ_2 distribution, we may also study the $\bar{p}p \rightarrow \chi_2$ formation mechanism, since the χ_2 may be formed both with net helcity zero and net helcity one. The motivation for this is that massless QCD prohibits a net helcity zero component. However, thė statistics is too feeble to give a definite value for B_0, the net helicity zero component.

5. ELASTIC SCATTERING AT 90^0 CM

5.1 Introduction.

Throughout the data taking periods, several test runs were done with an open trigger requiring one charged particle in each detector arm. The purpose of this was twofold; to check the apparatus and to study the process:

$$p\,\bar{p} \rightarrow p\,\bar{p} \quad .$$

Since the charge of these particles remained unmeasured, we were restricted to measure cross-sections at 90^0 in the CM (Centre of Mass) system. As the detector provided no indepenent momentum measurement of the particles, nor any particle identification (except for photons and electrons); we were left with the two-body kinematics and the requirement of one particle per detector arm as the only means of identification of the process.

Even though the beam momentum range of 3 GeV/c to 6 GeV/c has been available for antiproton proton collisions for two decades, data on large angle elastic scattering are relatively scarce due to low cross sections and comparatively low antiproton beam luminosity in previous experiments. It is therefore worthwhile to perform an analysis to find the cross sections at 90^0 CM.

5.2 Trigger and Data Aquisition.

The trigger was designed to accept events with a single minimum ionizing particle in each arm. The matrix setting of the hodoscope was such that no specific kinematical correlation was required. However, in order to lower the trigger rate, events with particles at small angles in both detector arms were vetoed. A typical matrix setting for the hodoscopes is shown in fig. 5.1.

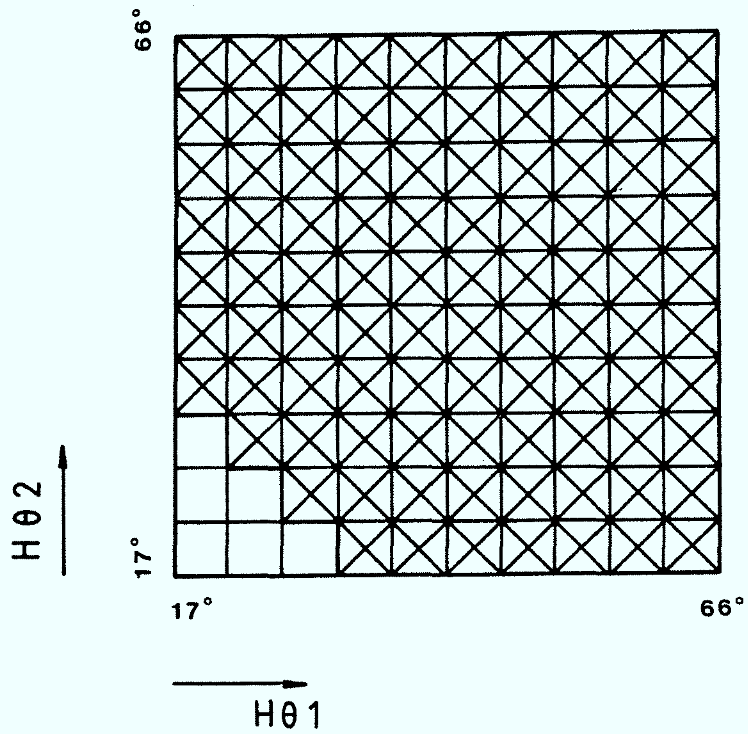

Fig. 5.1: Example of the matrix setting when triggering on minimum ionizing particles.

In order to quench the trigger rate further, only events with one hit in each scintillator plane were accepted. Since the shower hodoscopes were situated behind the precalorimeters, a rather large fraction of the events were lost because hadronic showers were initiated in the precalorimeter. However a few runs were done without multiplicity requirements, allowing a direct estimate of a correction factor (details in sect. 5.3.3). Finally, we mention that any signal in the veto counters would cause rejection of the event at the trigger level. A typical example of the trigger used for these runs is the following:

$$T2 = S_1 * S_2 * MH\theta * MH\varphi * MSH * \overline{VC} * \overline{VN}$$

Data were collected in four regions of lab. momenta, at (on the average) 3.65 GeV/c, 3.83 GeV/c, 4.07 GeV/c and 5.6-5.7 GeV/c; corresponding to centre of mass energies of the η_c, "off" η_c, the ψ, and the χ_1-${}^1P_1$-χ_2 region respectively.

This analysis is based on data collected at regular intervals throughout the whole lifetime of the R704 experiment. The experiment had three periods of running, two test periods in May and July 1983 and a long period (11 weeks) of running during the spring of 1984. In the table below, we give statistics on the number of hadronic triggers and the integrated luminosity collected during the different periods.

Momentum	3.65		3.83		4.07		5.6-5.7	
Period	Triggers	L/nb^{-1}	Triggers	L/nb^{-1}	Triggers	L/nb^{-1}	Triggers	L/nb^{-1}
May83	-------		-------		73665	4.39	-------	
July83	140427	7.39	-------		37665	1.75	64088	4.58
1984	92760	4.65	46288	2.16	59322	4.18	81661	16.48
Total	233187	12.04	46288	2.16	170528	10.32	145749	21.06

Table 5.1 Number of triggers and integrated luminosity collected for testing purposes, and for studying two-body processes at large angles.

5.3 Offline Analysis

The offline analysis is based on selecting events using the MWPCs for track reconstruction, and selecting events with the correct kinematics.

5.3.1 Production

The first stage of the production was a quick filter based on the hit pattern in the MWPCs.Events with a cluster configuration which rarely was found in good events, were rejected. If two or more clusters were found in at least two of the three planes of at least one of the two small MWPC chambers, the event was rejected. Basically, this filter rejected events with more than one charged particle in one of the detector arms. This filter speeded up the analysis considerably, especially at the highest energy, where multiplicities were high.

The second stage considered the event kinematics and the quality of the event reconstruction. After line reconstruction, performed independently in each arm, every combination of two lines was tried against the three cut parameters described below.

1. The events were required to be coplanar i.e. the incoming antiproton (assumed to be parallel to the nominal beam) and the two tracks in the detectors were required to lie in the same plane. The coplanarity was defined as:

$$C = (\vec{u}_1 \times \vec{u}_2).\vec{u}_3 / \|\vec{u}_1 \times \vec{u}_2\| = \cos \xi$$

where $\vec{u}_1$, and $\vec{u}_2$ are unit vectors along the direction of the two tracks; and $\vec{u}_3$ is a unit vector along the beam direction. ξ is the angle between the incoming beam and a vector normal to the plane of the two outcoming particles. Events with $|C| > .10$ were rejected. Fig. 5.2 shows the coplanarity distribution of events from one of the runs.

2. All events passing the coplanarity cut were required to have the opening angle expected for elastic events. For each reconstructed direction in arm 1, the polar angle expected in arm 2 was calculated, and compared to the polar angle(s) of the reconstructed line(s) in arm 2. The difference, $\Delta\theta$, between the expected and the reconstructed direction was calculated, and events with $|\Delta\theta| > 15$ mrad were rejected. Fig 5.3 shows the $\Delta\theta$ distribution for events passing the coplanarity cut and expected to obey elastic kinematics. The peak due to elastic events is very clear allowing for a justified value of the cut parameter $\Delta\theta$.

3. Finally, the vertex parameter, v, defined to be the shortest distance between the two lines, was calculated. Specifically, this (signed) distance may be written:

$$v = (\vec{P}_2 - \vec{P}_1).(\vec{u}_1 x \vec{u}_2)/\|\vec{u}_1 x \vec{u}_2\|$$

where $\vec{P}_1$ and $\vec{P}_2$ are points on the line in arm 1 and arm 2 respectively, and $\vec{u}_1$ and $\vec{u}_2$ are the two reconstructed directions. Fig. 5.4 shows the distribution of the vertex parameter for a sample of events. All events with $|v| > 4$ cm were rejected.

Finally, the events were subjected to a kinematical fitting procedure. The fitting was performed by a least squared method, and the constraints of energy and momentum conservation were introduced through Lagrangian multipliers. Events with a χ^2 per degree of freedom of the fit which was smaller than 10 were concidered as elastic event candidates . On basis of the χ^2 distributions, background substraction was performed. This is described in section 5.3.2.

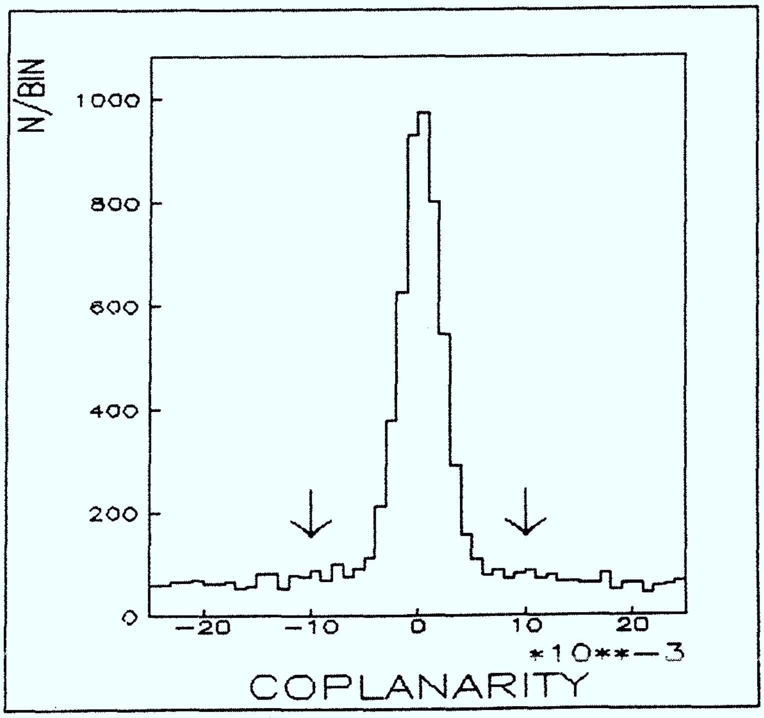

Fig. 5.2: Coplanarity distribution of a sample of events. The arrows indicate the cut values.

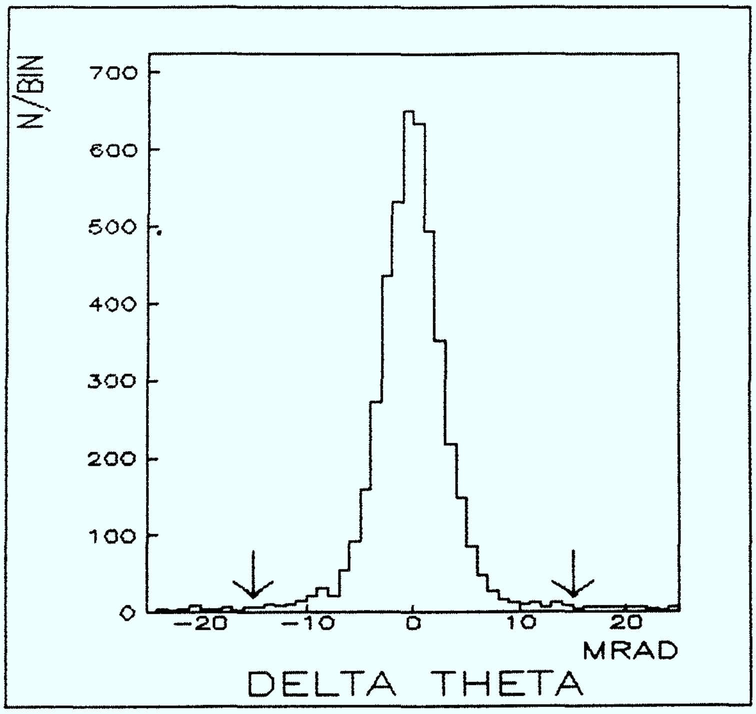

Fig. 5.3: Distribution of exepected minus recostruced polar angle in arm 1 for a sample of events which were subject for the elastic analysis.

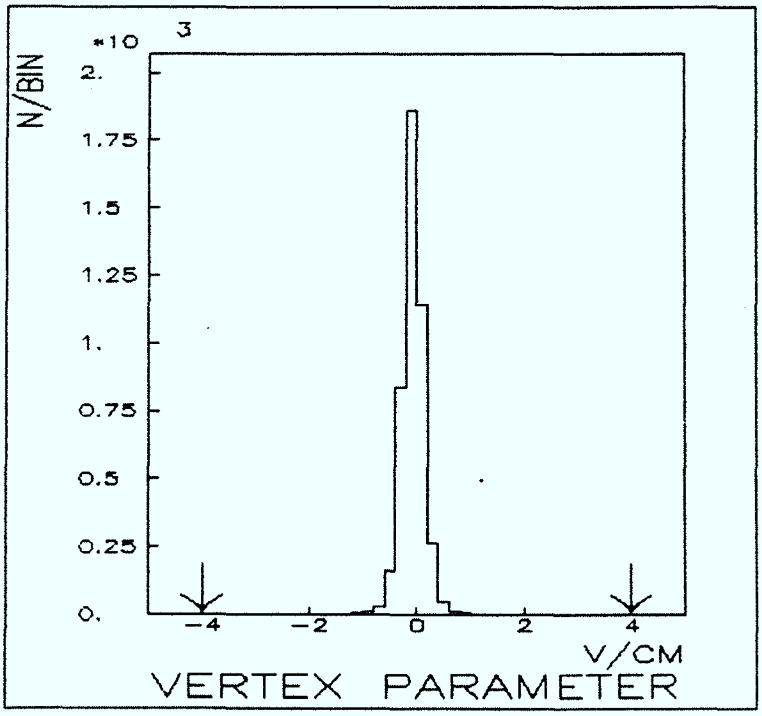

Fig. 5.4: Vertex parameter distribution for events passing the kinematical cuts.

5.3.2 Background Substraction

Although the presence of elastic events is evident from figs 5.1 and 5.2, it is clear that some background is present in the final event sample. This background may have several origins.The most important background source is probably that a few events may actually be multiparticle final states, with one or several particles escaping detection.

The background contamination of the event sample passing the kinematical fitting procedure may be estimated by studying the χ^2 distribution obtained. The χ^2 distribution for good events should have a mean value which is equal to the number of degrees of freedom of the fit, ND. Since, in our case, ND may vary between 5 and 7 depending on the number of efficient MWPC planes (required to be more than 5 in each arm), it is more convenient to study the quantity χ^2/ND, which should be distributed with a mean value of 1. In fig. 5.5 the distribution of χ^2/ND is shown for a sample of events passing the analysis.

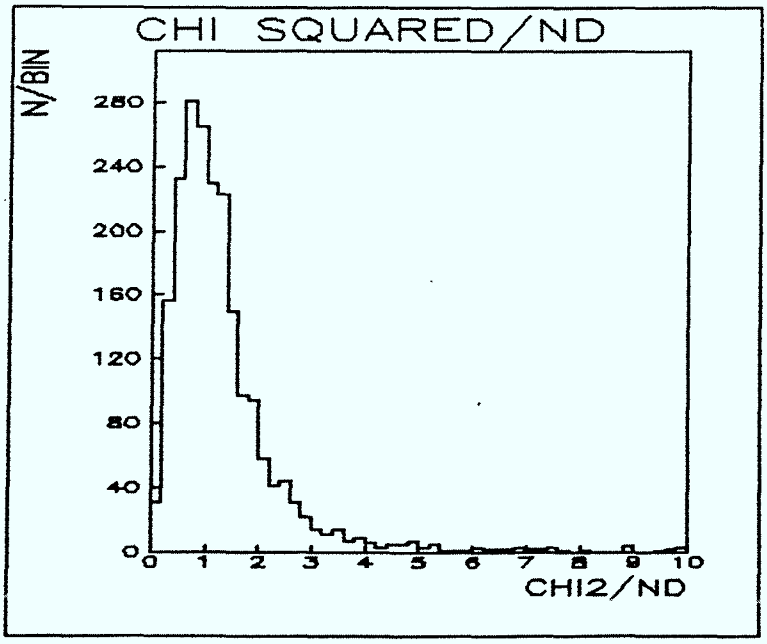

Fig. 5.5: Distribution of χ^2 per degree of freedom for events passing the cuts of the analysis.

The extent to which the χ^2 distribution agrees with the theoretical one, $F(ND,\chi^2)$, depends on the correctness of the estimates of the errors of the measurements. However, it seems reasonable to assume that the distribution becomes shifted in a systematic manner. Specifically, the confidence level, defined by:

$$C.L. = \int_{\chi^2}^{\infty} F(ND,x)\, dx$$

whose distribution should be constant on the interval between 0 and 1, could be assumed to be distributed according to a smooth function for an event sample consisting of only good events. In the following, we will assume that the distribution of C.L. for good events may be described by a linear function. The presence of a background in our sample should cause a build-up of events with low confidence level.

The background in the samples of elastic candidates is estimated by fitting the distribution of events with C.L. > 0.2 to a straight line and extrapolating this line to C.L. = 0. The number of events exceeding the number expected from this extrapolation, are then assumed to be equal to the number of background events. Fig. 5.6 shows an example of the method on a sample of elastic candidates.

Another method of background estimation is to study a scatterplot of coplanarity versus $\Delta\theta$. The number of background events is estimated by assuming that the background events are evenly distributed in this plot, in a region close to the region of elastic events, and counting the number of events present just outside the cuts imposed during the analysis.Fig. 5.7 illustrates the method.

The two estimates of the background produced results which were compatible. The first method was adopted for estimating the background.

in our data sample. The amount of background ranged from 10 % to 30 % depending on the incident momentum, and the trigger (multiplicity requirements).

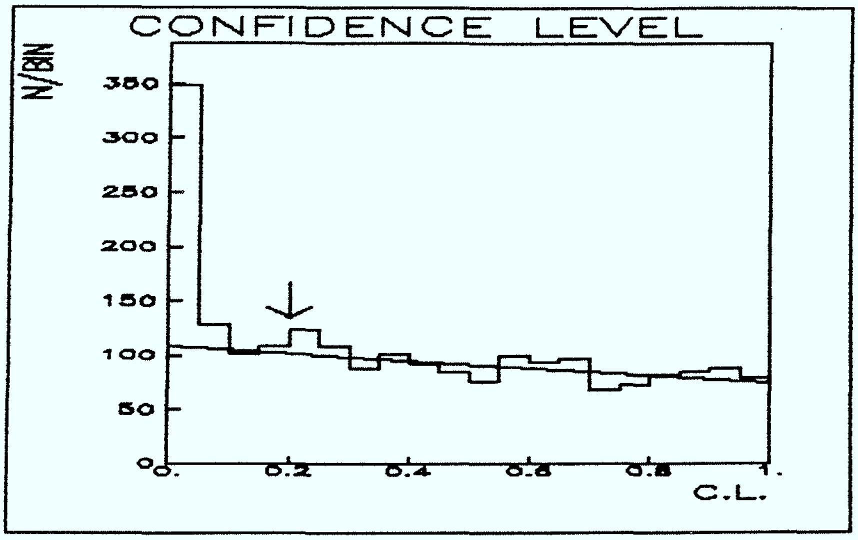

Fig. 5.6: Distribution of the confidence level for a sample of elastic candidates. The accumulation of events towards low confidence level is assumed to be due to the presence of background. The straight line is a fit to the distribution of events above c.l.=0.2.

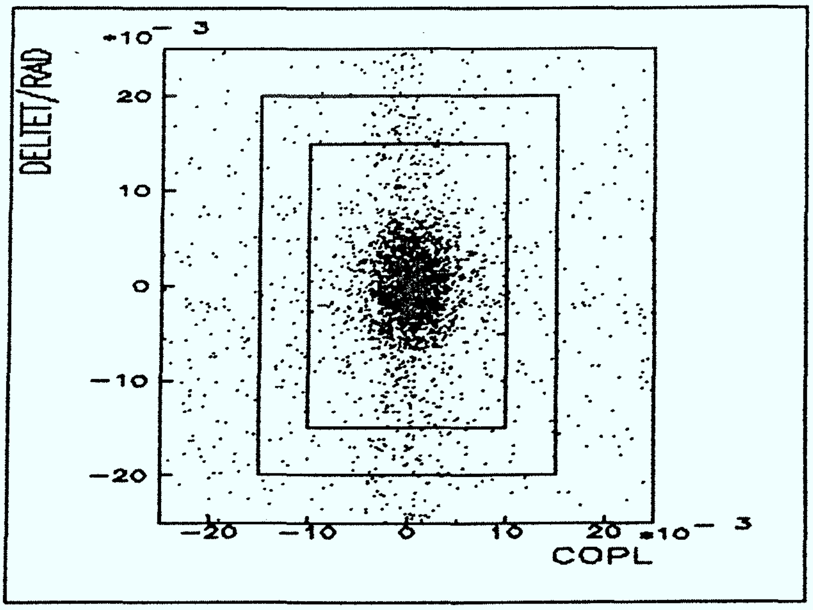

Fig. 5.7: Δθ vs. coplanarity for a sample of events. The events inside the small rectangle are accepted for further analysis. The background contamination was studied by counting events in the region between the small and the big rectangle.

5.3.3 Correction Factors.

In order to determine the cross sections, a number of corrections had to be applied to the data. The corrections described below are all calculated by averaging over the range of $-.04 < \cos\theta^* < .04$, corresponding to $87.7^0 < \theta^* < 92.3^0$. ($\theta^*$ is the scattering angle in the centre of mass system). Three main corrections were applied to the data, due to:

1. Trigger inefficiencies
2. Reconstruction inefficiencies
3. Geometric acceptance

The trigger inefficiencies are mainly due to the tight multiplicity requirements. Most runs were performed with a trigger requiring just one hit in each scintillator plane. As the shower hodoscopes were situated behind the precalorimeters, events which initiated a hadronic shower in one of the precalorimeters could be lost. The probability for such a shower to be initiated in one of the precalorimeters is about 60 %, since each precalorimeter consists of roughly 0.3 nuclear interaction lengths of matter. In addition, the hodoscope elements will, as seen from the interaction region, overlap slightly, meaning that there is a finite probability that one particle will cause a signal in two adjacent counters.

A few runs were performed without requirements on the multiplicities. Events from these runs, fitting the elastic hypothesis with a χ^2/ND <2, were studied in order to estimate the trigger efficiencies. A trigger efficiency of (41.3 $\pm$ 0.5)% was found for runs with the tightest requirements on the trigger multiplicities. Runs at several momenta were studied, but no dependence of the incident momentum was found in this correction. Appropriate correction factors were estimated in the same manner for a few runs with multiplicity requirements which were different from the one mentioned above. (several runs had no requirements on the multiplicities of the shower hodoscopes).

Two factors determine the offline reconstruction efficiency. Firstly, a fast filter on the MWPC cluster pattern (described in the beginning of sect. 5.3.1) was introduced in order to speed up the analysis. It was found that $(93.2\pm2)\%$ of the elastics survived this filter.

Secondly, the MWPC wires were not 100 % efficient. In the reconstruction, at least 5 out of 6 wire planes in each arm were required to be efficient. For each run, the reconstruction efficiency was calculated. A weighted mean of this efficiency was calculated for each energy. The reconstruction efficiency varied between 85% and 95%.

The geometrical acceptance was calculated by Monte Carlo simulations for each trigger and each energy in the angular range of $|\cos(\theta^*)| < 0.04$. The acceptance was found to vary between 23.6% and 25.7%, dependign on the trigger and the incident momentum.

It is concieveable that good events are lost due to too strict cuts. This was investigated by studying the coplanarity distribution of events not passing the $\Delta\theta$ cut, and $\Delta\theta$ the distribution of events not passing the coplanarity cut. No peaks in the $\Delta\theta$ distribution was found. A broad peak in the coplanarity distribution was noted. However, the number of events in this peak did not seem to increase when decreasing $|\Delta\theta|$ towards the cut value of 15 mrad. Thus, we cannot conclude that this peak stems from the tail of the $\Delta\theta$ distribution for elastic events. We conclude that the coplanarity and $\Delta\theta$ cuts reject a neglible amount of good events.

5.4 The Elastic Cross-sections.

For the final cross-section calculation, events with $|\cos(\theta^*)|<0.04$ were considered. The background was substracted individually at each energy and for each of the three periods of running. Whenever the correction factors (such as recostruction efficiencies) were expected to remain stable, weighted averages of these factors were calculated for the appropriate run sequences.

The cross-section is given by:

$$\frac{d\sigma}{d\Omega} = \frac{N - N_B}{2\pi \ \Delta\cos(\theta^*) \ L \ K}$$

where:

N is the number of events,

N_B is the estimated number of background events,

$\Delta\cos(\theta^*)$ is the range of the CM scattering angle

L is the integrated luminosity, and

K is a correction factor equal to the product of the efficiencies at each stage of the analysis.

The luminosity measurements are obtained by measuring the rate of small angle elastically scattered events, as explained in sect. 2.4.3. The luminosity measurements are accurate to within 5% [72]. For the first test runs, this luminosity measuring system was not available. Instead, the rate of coincidences of signals in the two small scintillators were used as a measure of the luminosity. The count rates were compared to the proper luminosity measurements whenever possible; and the integrated luminosities of the first test runs were deduced from this information. The errors in these measurements are assumed to be 8 %.

In the table below we summarise the results.

p GeV/c	N	L nb^{-1}	$d\sigma/d\Omega$ $\mu b/ster$	$-t$ $(GeV/c)^2$	$d\sigma/dt$ $\mu b/(GeV/c)^2$	Relative error(%)	
						stat	syst
3.65	3151	12.04	4.52	2.65	10.7	1.8	9.1
3.83	684	2.16	3.92	2.78	8.85	3.8	9.1
4.07	1577	10.32	2.12	3.03	4.39	2.6	9.1
5.6-5.7	107	21.06	0.041	4.50	0.057	19.0	11.8

Table 5.2: Differential cross-sections for antiproton-proton elastic scattering at 90^0 CM.

5.5 Discussion.

In Fig. 5.8 we show a log-log plot of $d\sigma/dt$ at 90^0 CM versus s, the square of the centre of mass energy. The increase of precision of our data points with respect to previous measurements is clearly visible.

A fit of the form s^{-n} has been performed using our four data points. Since the systematic errors mainly stem from the uncertainty in the luminosity measurements, we assume that these errors have shifted all four data points in the same direction. Hence, the systematic errors were ignored when performing the fit.

The results of the fit is:

$$n = 12.3 \pm 0.2$$

The quality of the fit is poor, as shown in fig. 5.9, where our results are compared to proton-proton elastic scattering data. The data point at 5.6 GeV/c is well below the fitted line. The cross section at 90^0 seems to be falling off faster in this region than in the region around 4 GeV/c. The proton-proton data, however, follow a power law beaviour, and a a good fit of the form s^{-n} is performed, yielding $n=9.0\pm0.3$

Several models for large angle scattering predict an s^{-n} dependence of $d\sigma/dt$ at fixed angle. However, the specific value of n is model dependent. The dimensional counting rule [73] predicts n=10. The constituent interchange model (C.I.M.), however, predicts n=12 [74]. Both models have the same prediction of n for antiproton-proton and proton-proton elastic scattering. This is clearly not the case in our energy region.

The reaction $\bar{p}p \to \bar{p}p$ is related to the reaction $pp \to pp$ by crossing. In fig. 5.10, the ratio of the two cross-sections at 90^0 are plotted as a function of s. For our data points, this ratio was computed by estimating the $pp \to pp$ cross-sction at the proper s using the result of the fit to the pp data presented in fig. 5.9. A marked change in this ratio is observed over our energy range. This confirms previously noted trends, as seen in the figure. The mechanisms of elastic scattering seem to change dramatically from incident momenta of 3.5 GeV/c to 5.5 GeV/c.

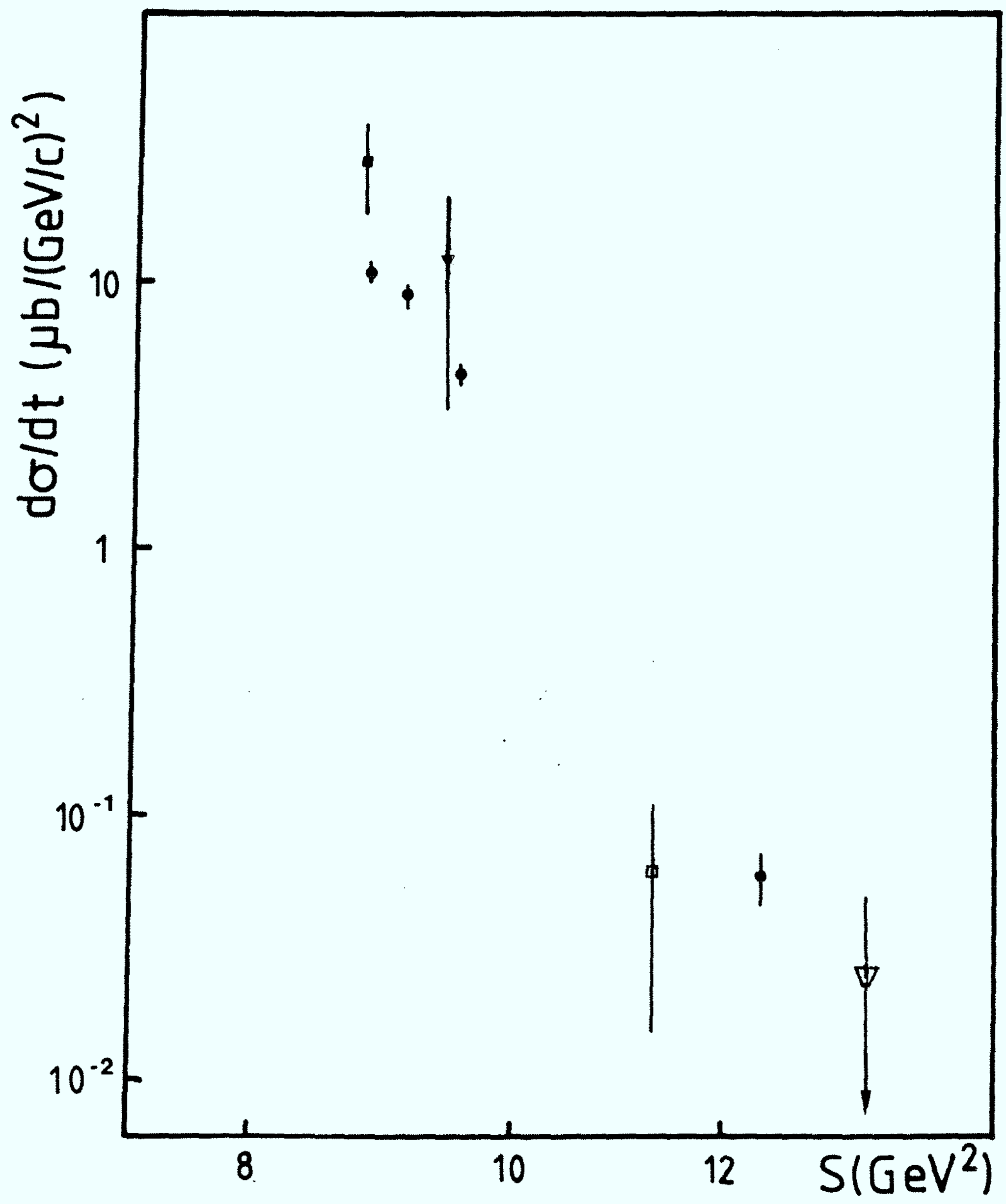

Fig. 5.8: The $p\bar{p} \rightarrow p\bar{p}$ differential cross section at 90^0 CM as function of the square of the CM energy (s). Solid cirles are from this experiment. Otherwise from [81] (solid square), [82] (solid triangle), [83] (open square) and [84] (open triangle).

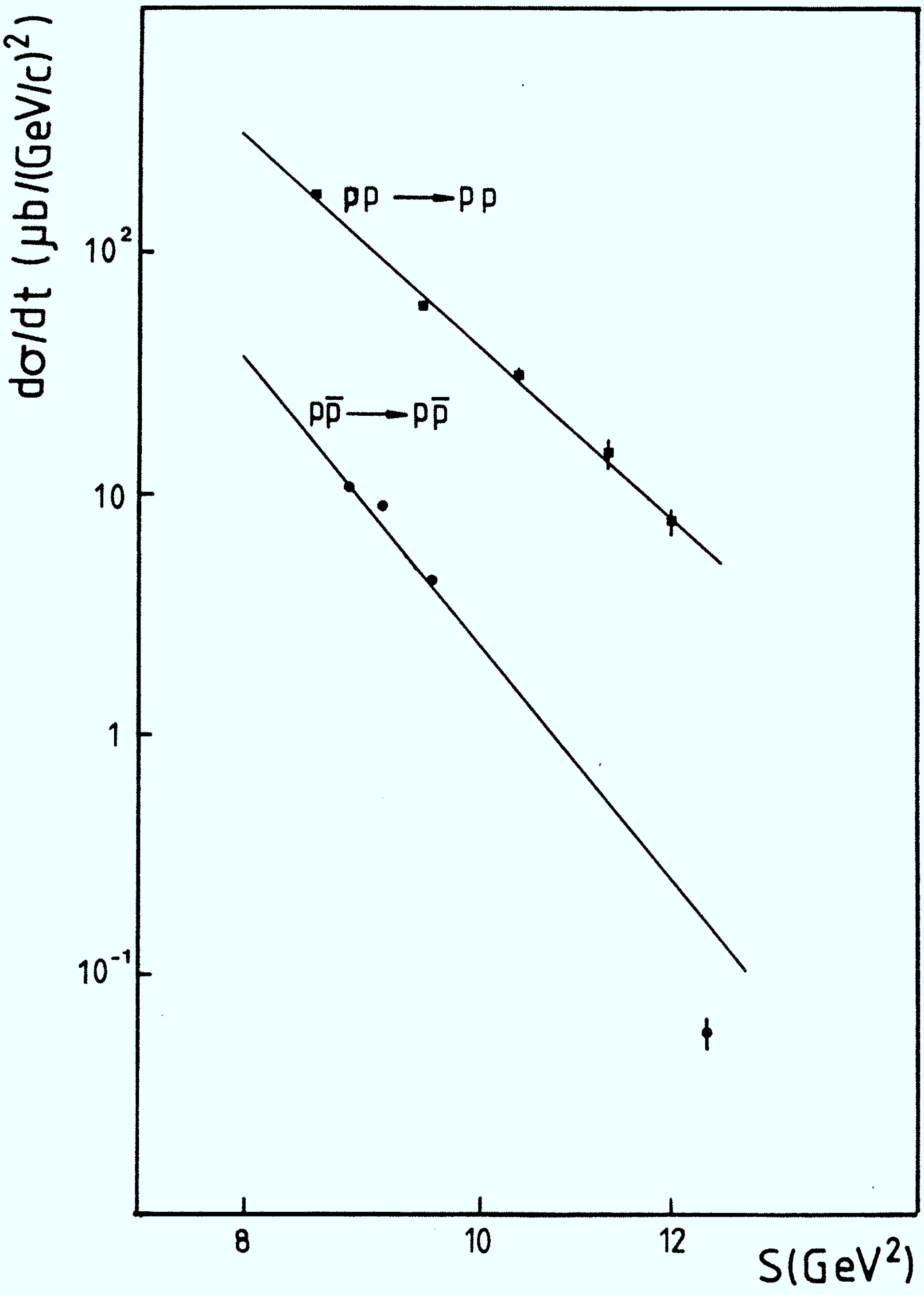

Fig. 5.9: $p\bar{p}$ elastic cross section at 90^0 CM compared to the pp elastic cross section at 90^0 CM. Solid circles denote the $p\bar{p}$ points from this experiment. Systematic errors are not included in the figure. The pp data (squares) are from ref. [75]. The lines indicates the results of fits of the form s^{-n} to the two data sets. Systematic errors were ignored in these fits.

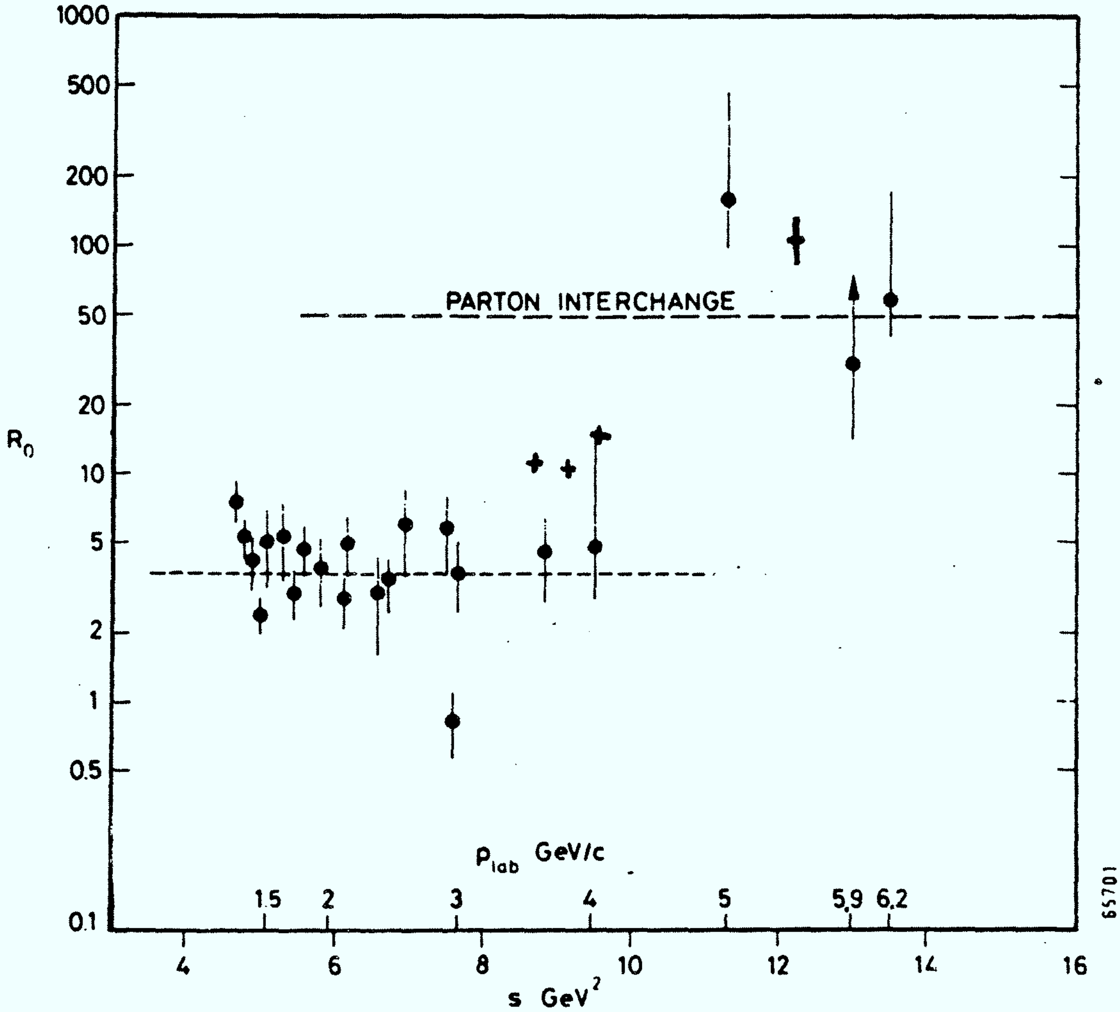

Fig.5.10: The ratio between the pp and the p$\bar{p}$ elastic cross sections at 90^0 as function of energy. From [76]. The results of this experiment are added (crosses). The upper dashed line is the c.i.m. prediction

5.6 Conclusions.

We have measured the antiproton-proton elastic cross-section at 90^0 CM for several incident momenta in the range 3.6-5.7 Gev/c. The precision of these measurements is superior to previously reported measurements. The cross-section in this region seems to fall off faster than s^{-12}. This is much faster than the falloff of the proton-proton elastic cross section, previously measured (e.g. ref. [75]). The results also confirm the previously noted [76] change in the ratio of the pp to the $p\bar{p}$ elastic cross section over the incident momentum range of 3.5-5 GeV/c.

6. CONCLUSIONS.

The new technique employed in the experiment R704, to use an internal gas-jet target in a storage ring, has proved very successful for high precision studies of low cross-section reactions in antiproton proton collisions. The gas-jet target worked very nicely throughout the lifetime of R704, and the relatively poor statistics accumulated is entirely due to the short supply of antiprotons, and the limited running time allocated to this experiment. Nevertheless, a number of significant measurements have been performed; some of which are discussed in this dissertation.

We have described an analysis chain leading to the discovery of five events which are consistent with the resonant formation of the $^1P_1$ charmonium state, subsequently decaying into a state containing a ψ which in turn decays into an electron positron pair. The mass of the $^1P_1$ deduced from these events are compatible with the mass of the spin weighted centre of gravity of the ^3P states. This is consistent with the hypothesis that the confining forces in the charmunium system are of a scalar nature. The cross section for the formation of these events is also very reasonable within the charmonium model. However, the statistical significance of this signal is rather poor, as the hypothesis that these events are due to non-resonant inclusive ψ production cannot be ruled out.

Furthermore, we have studied the angular distributions in the processes $p\bar{p}\to\chi_J\to\psi\to\gamma e^+e^-$, J=1,2. We have shown that the data are consistent with the conventional spin assumptions of these states, although alternative spin hypotheses may not be ruled out from this study alone. Only spin 0 for the χ_2 is ruled out with a confidence level which is smaller than 1%. Assuming the conventional spins for these states, it is found that the χ_1 radiative transition to the ψ is consistent with a pure dipole transition. However, the study of the χ_2 angular distribution leads us to the conclusion that the χ_2 radiative transition to the ψ seems to contain a positive quadrupole component. Moreover, it is found that the χ_2 data are consistent with the hypothesis that a single quark radiates the photon in the transition to the ψ. We have also attempted to measure the net helicity 0 component in the $p\bar{p}\to\chi_2$ formation process. No firm conclusion can be drawn from this study.

Finally, we have measured the $p\bar{p}$ elastic cross-section at 90^0 CM for four lab. momenta between 3.6 and 5.7 GeV/c. The precision of these measurements greatly exceeds the precision of previously available data at these momenta. It is found that the elastic cross-section at 90^0 CM decreases faster than s^{-12} over our energy range. When compared to the pp cross section, the tendency that the ratio between the two cross-sections changes dramatically over the momentum range of 3.5 to 6 GeV/c is confirmed by our measurements.

APPENDIX 1 R704 COORDINATE SYSTEMS

Occasionally, throughout the thesis it is referred to coordinates of impact points, track parameters etc. Here we describe the conventions used.

The laboratory system is defined to have its z axis pointing along the horizontal antiproton beam, with origin in the middle of the interaction region, i.e. in the middle of the interscept between the beam and the gas-jet. The y axis is vertical, pointing upwards, and the x axis is horizontal in a right handed system.

For each arm, a local system was defined, with z' and z'' axes pointing into the middle of arm 1 and arm 2 respectively. The z' and z'' axes are both at an angle of 41.5^0 with respect to the z axis of the lab. system. All three z axes are horizontal, and the z' and the z'' axes are at an angle of $2\times41.5^0 = 83^0$ with respect to eachother. The x' and x'' axes are horizontal and point away from the antiproton beam, and the y' and y'' are vertical in right handed systems.

All three systems were intended to have a common origin in the middle of the interaction region. However, offline studies showed that the two detector arms were mounted along axes which crossed 0.4 cm upstream of the middle of the interaction region, i.e. at $z= -0.4$ cm [77]. The origins of the two arm systems are hence common, and at $x=0$ cm, $y=0$ cm, and $z= -0.4$ cm. Fig. A1.1 shows how the different coordinate systems are arranged.

Whenever polar coordinates are used, θ denotes the polar angle and φ the azimuthal angle.

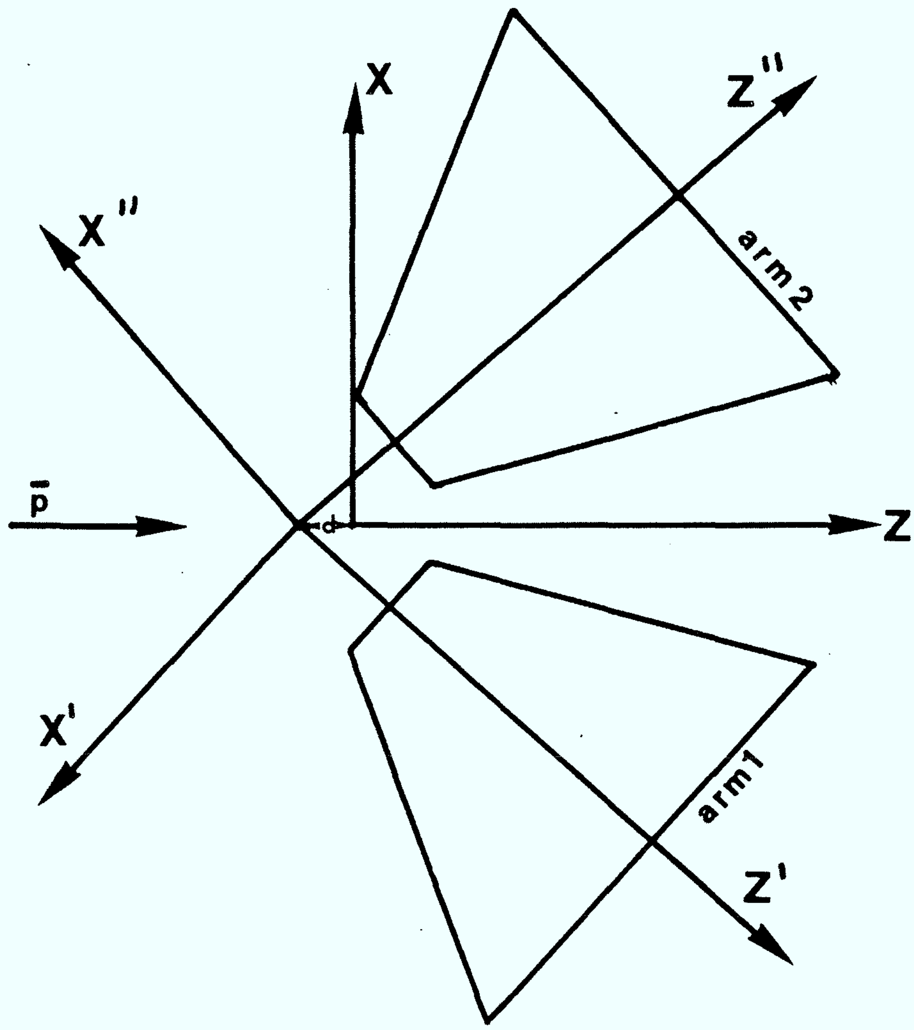

Fig. A1.1 Definition of the R704 coordinate systems.

APPENDIX 2: ANGULAR DISTRIBUTIONS IN THE HELICITY FORMALISM.

The helicity of a particle is defined as $\lambda=\vec{s}.\vec{p}/\|\vec{p}\|$, where $\vec{s}$ is the spin of the particle and $\vec{p}$ its momentum. The helicity is invariant under boosts and rotations, so the helicity formalism is well suited for applications to relativistic systems.

Consider a decay process $\alpha \rightarrow 1+2$, where α has spin J with projection M along some axis, z, in a coordinate system where α is at rest. We wish to find the probability amplitude of the particles to emerge with helicities λ_1 and λ_2 and with polar and azimuthal angles θ and φ (of particle 1 for definiteness). This amplitude may be written:

$$A = \langle\theta,\varphi,\lambda_1,\lambda_2|\ U\ |J,M\rangle$$

where U is some operator which propagates the transition from the initial to the final state. We may now specify the final state by its total angular momentum, j, and angular momentum projection (onto z), m, instead of using the angles. Inserting a complete set of these angular momentum states, we obtain:

$$A = \sum_{j,m} \langle\theta,\varphi,\lambda_1,\lambda_2|j,m,\lambda_1,\lambda_2\rangle\langle j,m,\lambda_1,\lambda_2|\ U\ |J,M\rangle$$

Angular momentum conservation requires that j=J and m=M, so:

$$A = \langle\theta,\varphi,\lambda_1,\lambda_2|J,M,\lambda_1,\lambda_2\rangle\langle J,M,\lambda_1,\lambda_2|\ U\ |J,M\rangle$$

It may be shown that the coefficient is given by [78]:

$$\langle\theta,\varphi,\lambda_1,\lambda_2|J,M,\lambda_1,\lambda_2\rangle = \text{const} \times D^{J*}_{M,\lambda}(\varphi,\theta,-\varphi) \quad ,$$

where $\lambda=\lambda_1-\lambda_2$. $D^{J*}_{M,\lambda}(\varphi,\theta,\chi)$ is the complex conjugate of:

$$D^{J}_{M,\lambda}(\varphi,\theta,\chi) = e^{-iM\varphi} \; d^{J}_{M,\lambda}(\theta) \; e^{i\lambda\chi}$$

The $d^{J}_{M,\lambda}(\theta)$ functions are explicitly given in e.g. ref.[8].

The term $\langle J,M,\lambda_1,\lambda_2| \; U \; |J,M\rangle$ depend on the helicities and the dynamics of the transition, and may be denoted by A_{λ_1,λ_2}.

In order to write down the angular distribution of the process

$$\bar{p}p \rightarrow \chi_J \rightarrow \gamma+\psi$$
$$\qquad\qquad\qquad\qquad \hookrightarrow e^+e^-$$

or

$$1+2 \rightarrow \chi_J \rightarrow 3+4 \qquad\qquad ;$$
$$\qquad\qquad\qquad\qquad \hookrightarrow 5+6$$

we note that the probability amplitude for the transition of the χ_J to the final state is the product of the probability amplitudes of two decay processes. Furthermore, we must sum over the unmeasured intermediate states, so choosing a frame with z axis along the direction of particle 1 in the C.M. system, and an x axis such that $\varphi=0$, we obtain:

$$A(\chi\rightarrow\text{final}) \; \alpha \; \sum_{\lambda_4} d^{J}_{M,\lambda_4-\lambda_3}(\theta) \; A_{\lambda_3,\lambda_4} \; D^{J'*}_{\lambda_4,\lambda_5-\lambda_6}(\varphi',\theta',-\varphi') \; C_{\lambda_5,\lambda_6} \quad ,$$

for an initial state specified by J and M, and a final state specified by λ_3, λ_5 and λ_6. J' is the spin of particle 4 (the ψ). The primed angles are in a frame where particle 4 is at rest. Here,the z' axis is chosen to lie along the direction of flight of particle 4 and with x' axis lying in the plane formed by the z' axis and the direction of flight of particle 1. It is also assumed that particle 4 is at rest in the unprimed system.

At this stage, we may relate some of the coefficients $A_{\lambda,\lambda'}$ and $C_{\lambda,\lambda}$ to eachother by exploiting parity conservation; and the helcity conserving properties of QED. The masslessness of the photon prohibits $\lambda_3=0$. Furthermore $|\lambda_5-\lambda_6| = 0$ is prohibited. Hence:

$$C_{\lambda,-\lambda} = 0 \qquad \text{and} \qquad A_{0,\lambda} = 0 \qquad (\text{for all } \lambda)$$

Parity conservation in electromagnetic interactions permits us to write [78]:

$$C_{-1/2,-1/2} = P^{\psi}(-1)^{J'} C_{1/2,1/2} \equiv C$$

and

$$A_{1,\lambda_4} = P^{\chi}(-1)^{J} A_{-1,-\lambda_4} \equiv A_{|\lambda_4-\lambda_3|}$$

where P^{ψ} and P^{χ} are the parities of the ψ and the χ. In addition, conservation of angular momentum requires $|\lambda_4-\lambda_3| \leq J$. Since the coefficient, C, multiplies every term in the expansion, it does not affect the angular distribution, and may be put equal to 1. Taking into account the dynamics of the formation process through the coefficients B, we obtain finally for the full angular distribution:

$$W(\theta,\theta',\varphi') = \sum_M B_M^2 \left(\sum_f \left| \sum_{\lambda_4} d^J_{M,\lambda_4-\lambda_3}(\theta)\, D^{1*}_{\lambda_4,\lambda_5-\lambda_6}(\varphi',\theta',-\varphi')\, A_{|\lambda_4-\lambda_3|} \right|^2 \right)$$

where f denotes a final state helicity configuration, i.e. the sum is over λ_3, λ_5 and λ_6. M is the component of the angular momentum of particle 3 onto the beam axis. We note that the orbital angular momentum between the two initial state particles may not have a component along this axis. Hence $M = \lambda_1 - \lambda_2$, the difference between the helicities of the two initial state particles. Again, we can exploit parity conservation to write:

$$B^2_M = B^2_{-M} .$$

APPENDIX 3: MONTE CARLO SIMULATION OF A DISTRIBUTION.

One is often faced with the problem of simulating an experiment where the distribution of events is not isotropic in space. Starting from a uniform random number generator, one has to extract the sought distribution. There exists an analytical procedure which can be employed in order to obtain this distribution, $P(x)$. If we assume that the distribution is properly normalized, i.e.

$$\int_{-\infty}^{\infty} P(x)dx = 1$$

we may generate the quantity

$$F(y) = \int_{-\infty}^{y} P(x)dx$$

uniformly on the interval $0<F(y)<1$. Then $y=F^{-1}(y)$ will be distributed according to the function $P(x)$.

The inversion of $F(y)$ is often a very difficult task. Hence, in most cases a different procedure is employed. The following algorithm will generate a number which is distributed as $P(x)$, if the range of x is restricted to some interval.

1. Generate a random number, y, on the interval $[0,\max(P(x)]$. ($\max(P(x)$ is the global maximum of the function $P(x)$)

2. Generate the function argument, x, randomly on its range, and calculate $P(x)$.

3. If $P(x)>y$, accept x as an event; reject x otherwise.

The set of accepted x will now be distributed according to $P(x)$.

This procedure is easily generalized to the multidimentional case, and this was the procedure employed when generating events according to the angular distribution $W(\theta,\theta',\varphi')$.

APPENDIX 4: STATISTICAL METHODS.

The most general method of parameter estimation is the maximum likelihood procedure. If the data are binned, the likelihood function depends on how the events are distributed among the bins in the observation space. Whenever the total number of events is fixed, a multinomial distribution law is obeyed. In this case, the likelihood function reads:

$$L_1 = N! \prod_{i=1}^{NB} \frac{p_i^{n_i}}{n_i!} \qquad ; \qquad \sum_{i=1}^{NB} p_i = 1 \; .$$

where p_i is the probability to observe an event in bin i, and n_i is the number of events in bin i. N is the total number of events, and NB is the number of bins. The probabilities, p_i, are functions of the parameters to be determined, and the best estimate of the parameters is the one which maximizes the likelihood function. Usually, maximizing the likelihood function is performed by minimizing its negative logarithm, i.e. seeking the global minimum of:

$$-\ln(L_1) = -\ln(N!) - \left(\sum_{i=1}^{NB} n \ln(p_i) - \sum_{i=1}^{NB} \ln(n_i!) \right)$$

The normalisation condition should of course still be obeyed.

If the total number of events is allowed to fluctuate according to a Poissonian distribution, the likelihood function becomes:

$$L_2 = \prod_{i=1}^{NB} \frac{m_i^{n_i} \exp(-m_i)}{n_i!}$$

where m_i is the expected number of events in bin i; i.e.

$$m_i = N \frac{p_i}{NB}$$

The negative logarithm of this is:

$$-\ln(L_2) = \sum_{i=1}^{NB} p_i - \left(\sum_{i=1}^{NB} n_i \ln(p_i) - \ln(n_i!) \right)$$

Note that whenever Σp_i is kept constant, the logarithms of the two functions are identical, except for a constant term.

If the bin size is infinitely small, just one event will fall into each bin, and the negative logarithm of L_1 becomes:

$$-\ln(L_1) = -\sum_{i=1}^{N} \ln(p_i) \qquad ; \quad \int p d\Omega = 1.$$

where the integral is over the observation space. Thus, in this case the method becomes identical to the one used for unclassified data, where the likelihood function is given by:

$$L_3 = \prod_{i=1}^{N} p_i$$

Whenever binomial statistics is assumed, the normalization condition should of course still be obeyed. This method should in principle give the most accurate determination of the unknown parameters since no averaging over bins is performed. However, another problem appears when using this method. The detector resolution should be known at all points where events are found, and properly accounted for by a resolution function. This problem may of course be eliminated in the binned case, if the bin size is much larger than the resolution. For proper normalization the detector acceptance should also be known at all points in detector.

The likelihood function for unclassified data may be a product of gaussians, i.e.

$$L_3 = \prod_{i=1}^{N} \exp(-(\bar{x}_i - x_i)^2 / 2\sigma_i^2) \quad .$$

where $x_i = x_i(\vec{\theta})$ is a function of the K parameters to be determined, θ_j, $j=1,2..,K$. In this case, minimizing the negative log of L_3 is equivalent to the least squares procedure of parameter estimation.

The conventional least squares method consists of minimizing the sum:

$$\chi^2 = \sum_{i=1}^{N} (\bar{x}_i - x_i)^2 / \sigma_i^2$$

Note the factor of 1/2 which is missing when comparing this expression to the negative log of L_3 above. Since this quadratic function is non-negative and have no upper bound, the best estimate of the parameters is uniquely determined by solving the K equations:

$$\frac{\partial L}{\partial \theta_j} = 2\sum_{i=1}^{N}((\bar{x}_i - x_i)/\sigma_i)\frac{\partial x_i}{\partial \theta_j} = 0 \quad .$$

The goodness of the fit may be tested by computing χ^2 for the estimated values of the parameters. Apart from depending on the parameters, χ^2 also depends on the number of degrees of freedom, ND; defined as the number of measurements, N minus the number of parameters to be estimated. Theoretically, the distribution of the χ^2 variable, $P_{ND}(\chi^2)$, has a mean value equal to ND, and a variance of 2ND. Small values of χ^2 indicates that the fit is succesful. More quantitatively, we may compute the confidence level, defined as:

$$C.L. = \int_{\chi^2}^{\infty} P_{ND}(x)dx \qquad (0 \leqslant C.L. \leqslant 1)$$

in order to give a quantitive statement on the goodness of the fit. Conversely, the C.L. of alternative hypotheses may be computed, and a low confidence level may indicate that this alternative hypothesis may be rejected. In order to reject a hypothesis, C.L. < .05 is frequently required. It should be stressed that a good fit to some model does not necessarily imply that the model is correct, since alternative models may also describe the data well.

The confidence level may be computed for other test statistics as well. In chapter 3, this is done for the Kolmogorov-Smirnov test statistic for a sample size of 5 events. In ref. [55], this quantity is called "the significance level". The explicit formula for computing the significance level for the Kolmogorov-Smirnov test is found in ref. [80].

The term "confidence level" is also used when quoting errors of estimated parameters. In the one parameter case, the confidence level associated with the estimate of a parameter, $\theta = \theta \pm \text{err}$, is

$$C.L. = \int_{\theta-err}^{\theta+err} L(\theta)d\theta$$

whenever $L(\theta)$ is properly normalized.

If $L(\theta)$ is a gaussian, the 1 σ error corresponds to a confidence level of 68%. In this case, the negative log of L will rize by 1/2 whenever the function argument is $\theta+\sigma$ or $\theta-\sigma$. In this context it is appropriate to note that whenever a parameter is estimated by the least squares method, the 68% C.L. error estimate is found by finding the L.S. function argument which gives a rise of the L.S. function of 1 unit with respect to its minimum [79].

LIST OF REFERENCES.

[1] : J.J. Aubert et al.: Phys. Rev Lett. 33 (1974) 1404.

[2] : J.E. Augustin et al.: Phys. Rev. Lett. 33 (1974) 1406.

[3] : J.E. Augustin et al.: Phys. Rev. Lett. 34 (1975) 764.

[4] : B.J. Bjorken and S.L. Glashow: Phys. Lett. 11 (1964) 255.

[5] : S.L. Glashow, J. Iliopoulos and L. Maiani: Phys. Rev. D2 (1970) 1285.

[6] : K. Berkelman et al.: Phys. Lett. 57B (1975) 407.

[7] : R.M. Baltrusaitis et al.: Phys. Rev. Lett. 52 (1984) 2126.

[8] : Particle Data Group: Rev. Mod Phys 56 (1984), Phys. Lett. 170B (1986).

[9] : E. Eichten et al.: Phys. Rev. D21 (1980) 203.

[10] : D.S. Kulshreshta: Phys. Rev. D26 (1982) 2331.

[11] : C. Quigg and J.L. Rosner: Phys. Rep. 56 (1979) 167.

[12] : A. Martin: Phys. Lett. 100B (1981) 511.

[13] : J.L. Richardson: Phys. Lett. 82B (1979) 272.

[14] : T. Appelquist, R.M. Barnett and K. Lane: Ann. Rev. Nucl. Part. Sci. 28 (1978) 387.

[15] : For a review, see L.J. Reinders, H. Rubinstein and S. Yasaki: Phys. Rep. 127 (1985) 1.

[16] : M.A. Shifman et al.: Phys. Lett. 77B (1978) 80.

[17] : R. Partridge et al.: Phys Rev. Lett. 45 (1980) 1150.

[18] : For a review, see A. Hasenfratz and P. Hasenfratz: Ann. Rev. Nucl. Part. Sci. 35 (1985) 559.

[19] : See e.g. J.J. Sakurai: "Advanced Quantum Mechanics." Addison-Wesley 1967.

[20] : E. Eichten and F. Feinberg: Phys. Rev. D23 (1981) 2724.

[21] : D. Gromes: Z. Phys. C22 (1984) 265.

[22] : D. Gromes: Z. Phys. C26 (1984) 401.

[23] : C. Michael: Phys. Rev. Lett. 56 (1986) 1219. A. Huntley and C. Michael: CERN-TH 4544/86.

[24] : P. de Forcrand and J. D. Stack: Phys. Rev. Lett. 55 (1985) 1254

[25] : H. Schnitzer: Phys. Lett. 65B (1976) 239.

[26] : A. De Rujula, H. Georgi and S.L. Glashow:
Phys. Rev. D12 (1975) 147.

[27] : H. Schnitzer: Phys. Rev. D13 (1975) 74.

[28] : L-H. Chan: Phys. Lett. 71B (1977) 422.

[29] : R. Van Royen and V.F. Weisskopf: Nouv. Cim. A50 (1967) 617.

[30] : A. Ore and J.L. Powell: Phys. Rev. 75 (1949) 1696.

[31] : V.A. Novikov et al.: Phys. Rep. 41C (1978) 1.

[32] : S. Cooper in Proc. of the Int. EPS Conf. on High Energy Physics, Bari, Italy 18-24 July 1985, p 945.

[33] : C.N. Yang: Phys. Rev. 77 (1950) 242.

[34] : R.W. Eaton et al.: Phys. Rev. D29 (1984) 804.

[35] : J.E. Augustin et al.: LAL/85-27 (1985).

[36] : C. Baglin et al.: Proposal to ISRC, CERN/ISRC/80-14.

[37] : For a review of Crystal Ball results:
E.D. Bloom and C.W. Peck: Ann. Rev. Nucl. Part. Sci. 33 (1983) 143.

[38] : A. Martin: Phys. Lett. 93B (1980) 338.

[39] : W. Buchmuller, G. Grunberg and S.-H.H. Tye:
Phys. Rev. Lett 45 103 (1980).

[40] : G. Bahnot and S. Rudaz: Phys. Lett. 78B (1978) 119.

[41] : E. Eichten et. al.: Phys. Rev. D17 (1978) 3090.

[42] : G. Carron et al.: Phys. Rev. D29 (1984) 804.

[43] : IEEE Transaction on Nucl. Sci. 28 (1981) 353.

[44] : C. Baglin et al.: "Charmonium Spectroscopy at the ISR Using an Antiproton Beam and a Hydrogen Gas "jet" Target",
CERN EP 85-01 (1985).

[45] : J.M. Brom: Thesis for the degree "docteur es .."
University of Strasbourg, CRN/HE85-04 (1985).

[46] : B. Stugu: Thesis for the degree Cand. Scient.,
University of Oslo (1983).

[47] : Jenaer Glaswerk, Schott & Gen., Mainz, FRG.

[48] : S. Stapnes: Thesis for the degree Cand. Scient.,
University of Oslo (1985).

[49] : A. Kylling: Thesis for the degree Cand. Scient., University of Oslo (1985).

[50] : D. Olsen: Thesis for the degree Cand. Scient., University of Oslo (1986).

[51] : C. Baglin et al.: Phys. Lett. 172B (1986) 455.

[52] : G. Rinaudo: R704 Internal Note no. 110.

[53] : C. Baglin et al. Phys. Lett. 171B (1986) 135.

[54] : M.K. Gaillard, L. Maiani and R. Petronzio: Phys. Lett. B110 (1982) 489.

[55] : A. G. Frodesen, O. Skjeggestad, H. Tøfte: "Probability and Statistics in Particle physics", Universitetsforlaget, Oslo 1979.

[56] : G. Borreani et al.: R704 Internal Note, 6.11.85.

[57] : W.Buchmuller: Phys. Lett. 112B (1982) 479.

[58] : A. Andrikopoulou: Z. Phys. C22 (1984) 63.

[59] : R. M. Baltrusaitis et al. Phys. Rev. D33 (1986) 629.

[60] : R. McLary, N. Byers: Phys. Rev. D28 (1983) 1692.

[61] : G. Segre, J. Weyers: Phys. Lett. 62B (1976) 91.

[62] : G. Karl, S. Meshkov, J. L. Rosner: Phys. Rev. Lett. 45 (1980) 215.

[63] : L. S. Brown, R. N. Cahn: Phys. Rev. D13 (1976) 1195.

[64] : M. G. Olsson et al.: Phys. Rev. Lett. 31D (1985) 203.

[65] : A. D. Martin, M. G. Olsson, W. J. Stirling: Phys. Lett. 147B (1984) 203.

[66] : G. Karl, S. Meshkov, J. L. Rosner: Phys. Rev. D13 (1976) 1203 and Ref. [65].

[67] : D. Olsen: R704 Internal Note no. 118.

[68] : Refs. [45] and [52].

[69] : F. James and M. Roos: Writeup D506, CERN Computer Centre Program Library.

[70] : M. Oreglia et al.:Phys. Rev. 25D (1982) 2259.

[71] : W. Tanenbaum et. al. Phys. Rev. 17D (1978) 1731.

[72] : A. Bussière, M. Chevallier and J. Fay: R704 internal note 112, and ref. [44].

[73] : S.J. Brodsky and G. Farrar: Phys. Rev. D11 (1975) 1309.

[74] : J. F. Gunion, S. Brodsky, R. Blankenbecler:
Phys. Rev. D8 (1973) 287.

[75] : R. Kammerud et al.: Phys. Rev. D4 (1971) 1309.

[76] : P. J. Carlson, K. E. Johansson:
Lett. Nuov. Cim. Ser. 2 17 (1976) 379.

[77] : B. Stugu: R704 Internal Notes no. 101 and 117.

[78] : J. D. Richman: "An Experimenters Guide to the Helicity
Formalism" CALT-68-1148 (1984).

[79] : F. James: "Interpretation of the Errors on Parameters as given
by Minuit"; Supplement to ref. [69].

[80] : D. B. Owen: "Handbook of Statistical Tables",
Addison-Wesley 1962.

[81] : W. M. Katz et al.: Phys. Rev. Lett. 19 (1967) 265.

[82] : O. Czyzewski et al.: Phys. Lett. 15 (1965) 188.

[83] : A. Eide et al.: Nucl. Phys. B60 (1973) 173.

[84] : T. Buran et al.: Nucl. Phys. B97 (1975) 11.